DISSERTATION

Titel der Dissertation

Deformation Induced Phase Transformation in Zr_3Al
Studied by Transmission Electron Microsopy

angestrebter akademischer Grad

Doktor der Naturwissenschaften (Dr. rer.nat.)

Verfasser:	Mag. David Geist
Matrikel-Nummer:	A 0104813
Dissertationsgebiet (lt. Studienblatt):	A 791 411
Betreuer:	Ao. Univ.-Prof. Mag. Dr. Christian Rentenberger

Wien, am 17. Februar 2011

Abstract

The production of nanocrystalline materials by severe plastic deformation of coarse grained structures has been attracting a lot of research interest for the last two decades. Despite the potential to change and tailor material properties by nanostructuring, there are rather limited data available for nanocrystalline intermetallic alloys. In this work, severe plastic deformation of the ordered $L1_2$ structured intermetallic compound Zr_3Al and the study of deformation induced structural changes are conducted for the first time. Zr_3Al is heavily deformed by the methods of high pressure torsion and repeated cold rolling with intermediate foldings. The deformation by high pressure torsion at room temperature leads to nanocrystalline samples and allows a systematic comparison to other $L1_2$ compounds subjected to high pressure torsion. This comparison facilitates the understanding of the influence of different dislocation dissociation mechanisms on the grain refinement characteristics and on the deformation induced phase transitions of these materials. A multi-scale analysis of the deformed Zr_3Al samples by transmission and scanning electron microscopy using both plan view and cross section samples allows to assess inhomogeneities from the atomic scale to the scale of the sample, revealing important deviations from the ideal torsion experiment and the change of deformation mechanisms with decreasing grain size. The deformation by repeated cold rolling with intermediate foldings leads to amorphous samples, thus unambiguously showing the different effects of the deformation methods on the saturation structure. In addition, calorimetric measurements yield information about the thermal stability and the crystallization behaviour of the material amorphized by rolling. It is shown that imperfect amorphization involving residual nanocrystallites facilitates the crystallization of a fine nanocrystalline structure. Hardness measurements by microindentation and X-ray diffractometry supplement these studies by yielding information on the mechanical properties and integral structural properties of deformed samples, respectively. By studying different deformation methods and the inhomogeneity of the deformation by high pressure torsion, this work is an important contribution to the physical understanding of structural changes of intermetallic compounds by severe plastic deformation.

iv

Zusammenfassung

Die Herstellung nanokristalliner Materialien durch extreme plastische Verformung grobkristalliner Strukturen wird seit rund zwei Jahrzehnten intensiv erforscht. Trotz des Potentials, Materialeigenschaften durch Nanostrukturierung zu verändern, wurden nanokristalline intermetallische Legierungen noch nicht umfassend untersucht. In dieser Arbeit wird die intermetallische Verbindung Zr_3Al, die die geordnete $L1_2$ Struktur aufweist, zum ersten Mal extrem plastisch verformt und die dabei auftretenden Strukturänderungen untersucht. Die dabei zum Einsatz kommenden Verformungsmethoden sind Hochdrucktorsion sowie wiederholtes Kaltwalzen und Falten. Hochdrucktorsion bei Raumtemperatur führt zu nanokristallinen Proben und ermöglicht einen systematischen Vergleich zwischen Zr_3Al und anderen hochverformten Verbindungen, die ursprünglich die $L1_2$ Struktur aufweisen. Dieser Vergleich liefert ein tieferes Verständnis des Einflusses der verschiedenen Versetzungsaufspaltungsmechanismen auf die Kornverfeinerung und die verformungsinduzierten Phasenumwandlungen. Eine raster- und durchstrahlungselektronenmikroskopische Betrachtung der verformten Proben ermöglicht die Untersuchung von strukturellen Inhomogenitäten ab der atomaren Skala bis hin zu einer Längenskala, die der Probengröße entspricht. Dabei werden Abweichungen von einem idealen Torsionsexperiment sowie der Wechsel der Verformungsmechanismen mit zunehmender Kornverfeinerung erklärt. Die Verformung von Zr_3Al durch wiederholtes Kaltwalzen und Falten führt zu amorphen Proben. Damit wird der Einfluss der verschiedenen Verformungsmethoden auf die Sättigungsstruktur gezeigt. Weiters werden kalorimetrische Messungen angewandt, um Auskunft über die thermische Stabilität und das Kristallisationsverhalten des durch Walzen amorphisierten Materials zu erhalten. Die unvollständige Amorphisierung, die Restnanokristallite im Material verursacht, begünstigt während des Aufheizens der Probe die Bildung einer nanokristallinen Phase. Härtemessungen und Röntgendiffraktometrie ergänzen all diese Studien durch Informationen über die mechanischen und integralen strukturellen Eigenschaften. Durch die Untersuchung verschiedener Verformungsmethoden sowie der Inhomogenitäten der Verformung durch Hochdrucktorsion kann diese Arbeit einen wesentlichen Beitrag zum physikalischen Verständnis der Strukturänderungen von intermetallischen Verbindungen durch extreme plastische Verformung liefern.

Contents

List of Figures

List of Tables

Chapter 1

Introduction

1.1 Outline of this thesis

In the introduction of this thesis, the effect of nanostructuring on the properties of a material will be described by two examples. Firstly, the change of hardness and related mechanical properties due to nanostructuring will be described, since hardness measurements were also done in the course of this thesis. Secondly, changes in the irradiation resistance will be described, since irradiation resistance played an important role in earlier investigations of Zr_3Al. In the third section of the introduction, the three probably most important methods of severe plastic deformation will be introduced, two of which were used in this work (high pressure torsion, repeated cold rolling with intermediate folding). The last section of the introduction deals with the properties and earlier studies of Zr_3Al and, to put the material into a larger context, the Zr-Al binary system as a whole.

In the second chapter, the experimental methods used in this work will be briefly introduced (i.e. X-ray diffraction, transmission and scanning electron microscopy, hardness testing and differential scanning calorimetry).

Chapters 3 through 6 cover the work that was published (in the case of chapter 6 the work was submitted and is not published yet) in ISI-listed journals in the course of this thesis. Chapter 3 was published in the journal Materials Science Forum and deals with a plan-view transmission electron microscopy (TEM) investigation of Zr_3Al deformed by high pressure torsion [S1]. A publication in Philosophical Magazine [S2] is the basis for chapter 4 that deals with the comparison of the deformation of three different $L1_2$

structured intermetallic compounds. In this context it must be mentioned that the experimental contribution of the author of this thesis was limited to Zr_3Al, whereas the Ni_3Al and Cu_3Au experiments were done by co-authors of the paper. Chapter 5 reports the effect of repeated cold rolling with intermediate folding and subsequent heat treatments on Zr_3Al. The content of this chapter has been published in Journal of Alloys and Compounds [S3]. Chapter 6 extends the study of Zr_3Al subjected to high pressure torsion by using experimental methods complementary to transmission electron microscopy and by extending the study from a plan-view study as in chapter 3 to a 3D study. By using both, plan-view and cross section samples, important results concerning the homogeneity of the HPT process could be obtained. The content of this chapter has been submitted to Acta Materialia [S4].

The last chapter will summarize the findings of this thesis and conclusions will be drawn.

1.2   Properties of nanocrystalline materials

Nanocrystalline (NC) materials are materials with a sufficient number of atoms located in the grain boundaries to significantly change the properties of the material compared to its coarse-grained counterparts (i.e. materials with grain sizes at least in the range of microns). This rather general definition leads to a wide spread of possibilities of maximum grain sizes for NC materials in review articles about the topic. Gleiter suggested in an early work that it is the idea of NC materials that 50% or more of the atoms are situated in the core of the defects [1]. Assuming that grain boundaries are the only relevant defects present in a material with very small grain size and further assuming a grain boundary thickness of 1 nm leads to the necessity of grains smaller than 5 nm to get a NC material [2]. In a later review [3] he defined the characteristic length scale as a few (typically 1 - 10) nm. Meyers defined NC materials as polycrystals with grain sizes between 1 nm and 250 nm [4]. Another definition that will be stuck to in this work is the one used in many cases (e.g. [5, 6, 7]), where the upper grain size limit of NC materials is set to about 100 nm. Materials with a grain size up to 1 μm will be referred to as ultra-fine grained (UFG) materials, thus incorporating NC and submicron materials (100 nm - 1 μm) as proposed in [6].
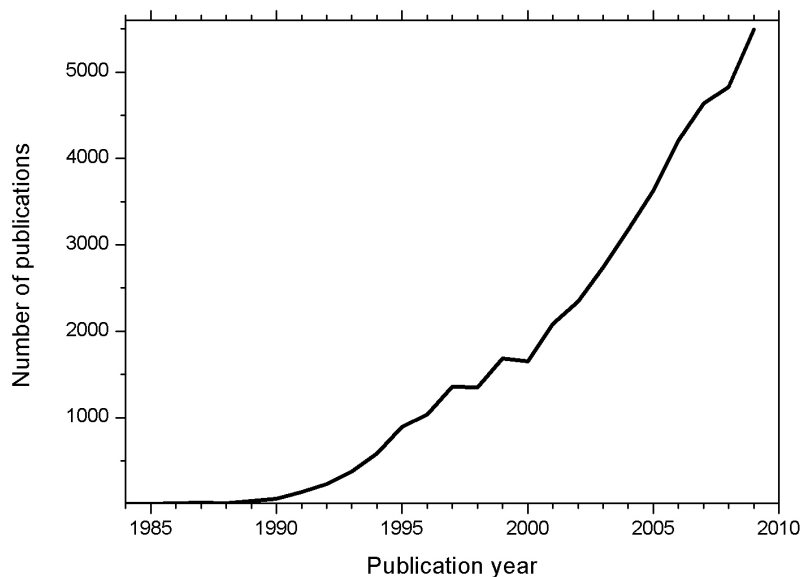
Figure 1.1: Number of published papers on the topic "nanocrystalline" from 1984 (2 publications) to 2009 (5433 publications) according to Thomson Reuters ISI Web of Knowledge [8]. [Certain data included herein are derived from the Web of Science ®prepared by THOMSON REUTERS ®, Inc. (Thomson®), Philadelphia, Pennsylvania, USA: ©Copyright THOMSON REUTERS ®2010. All rights reserved.]

NC materials have been a fast emerging topic for many years now. Starting in the mid 80's with only several publications per year, several thousands of papers are published each year nowadays, as is shown in Fig. 1.1. Due to the vast amount of publications concerning NC materials, a wide variety of property changes due to nanosize effects were studied and discussed in the last decades. The following two sections will show the possibilities to change material properties by changing the grain size to the nano- or the submicron scale by briefly reviewing the effects on the mechanical properties strength/hardness and on the irradiation resistance.

1.2.1 Mechanical properties

It is well established that the yield strength σ_y of coarse-grained material ($>$ 1 μm) as a function of grain size can be approximated using the Hall-Petch

relation:

$$\sigma_y = \sigma_0 + k\frac{1}{\sqrt{d}} \tag{1.1}$$

with σ_0 and k being material constants [9, 10]. Due to this relationship, nanostructuring of materials can significantly increase their hardness. In the case of Cu, the validity of the Hall-Petch relationship was shown down to a grain size of 10 nm. At this grain size, which was achieved by magnetron sputtering, hardness measurements yielded a value of 3.02 GPa, which is extraordinarily high for Cu [11]. NC Cu and Pd produced by inert gas condensation showed an increase in hardness by a factor of 2-5 [12] compared to the coarse-grained material. The problem of low ductility, that often accompanies nanostructuring of materials, can be bypassed for some materials by introducing a bimodal grain size distribution. For Cu, this lead to a material with a high tensile strength (6 times the value of coarse-grained Cu) and good ductility (65% elongation to failure) [13]. The hardening by grain size reduction, however, is known not to be valid down to "zero" grain size (i.e. amorphous materials):

Early reports of an inverse Hall-Petch relation causing softening in small NC samples may often have been related to imperfections in NC materials. Due to the application of bottom-up methods (mentioned in the introduction of section 1.3) and the necessity to solidify the material before testing, porosity and contamination can be regarded as the cause for early observations of softening at small grain size [14]. It was shown that a decline of Young's modulus was connected with an increase in porosity and that processing flaws, which were detected by small-angle neutron scattering, may significantly affect the tensile strength [15]. Nevertheless, it is widely believed that at a certain grain size, dislocation-mediated processes diminish and alternative processes become more important. Among the candidates in the still ongoing debate about the explanation of deformation of NC materials are: grain-boundary sliding, grain-boundary diffusional creep, rotational deformation, emission of (partial) dislocations from grain boundaries and deformation twinning [16, 17]. Examples of models and experimental data will be presented to give an insight into the hardness and yield strength evolution of small NC materials.

An early model [18] with very limited reliable experimental data available (due to the lack of high-quality NC samples) suggested conventional

Hall-Petch behaviour for large grains and Coble creep becoming more important with decreasing grain size, leading to a softening of the materials at grain sizes of approximately 5-25 nm. Assuming a log-normal distribution of grain sizes, experimental data was fit for Cu and NiP. However, as already mentioned, the experimental data available at that time was quite spread making it hard to assess the quality of the model.

Using molecular dynamics methods, Schiøtz and Jacobsen simulated the deformation of NC Cu with grain sizes between 5 and 50 nm at a strain rate of $5 \cdot 10^8$ s^{-1} (due to computational limitations, deformation behaviour at high strain rates is accessible more easily) [19]. They found that at small grain sizes, strain is localized in the grain boundaries indicating that the main deformation mechanism is grain boundary sliding, which was already described by earlier molecular dynamics simulations [20]. For larger grains, they saw indications for the majority of the deformation being accomplished by dislocation activity. In their simulation, the flow stress increased with decreasing grain diameter until a size of 15 nm. For grains 10 nm and less in diameter, they got a steep decrease in flow stress, thus supporting the idea of an inverse Hall-Petch relation at grain sizes < 10 nm. Similar results were obtained by conducting molecular dynamics simulations of NC Al. A transition from grain-size hardening to grain-size softening is observed at $\sim$ 30 nm, because at this grain size, the deformation mechanism changes from intragranular (dominant at grain sizes > 30 nm) dislocation-based deformation to intergranular grain boundary sliding mechanisms. This results in a maximum strength for Al at a grain size of $\sim$ 30 nm [21].

A model proposed by Kim and Estrin for Cu [22] assumes a mixture of grain interior and grain boundary phases. While, in this model, the plastic flow of the grain boundary phase was assumed to be diffusion controlled, the plastic flow of the grain interior is carried by both, dislocation mechanisms and diffusion controlled mechanisms. Simulating deformation experiments for the grain interior at grain sizes from 5 to 1000 nm, they found that with decreasing grain size and with decreasing strain rate, the contribution of diffusion increases: At $\dot{\epsilon} = 10^{-5}$ s^{-1}, there is no contribution of dislocation mechanisms to the deformation up to a grain size of 40 nm, whereas at the higher strain rate $\dot{\epsilon} = 10^{-1}$ s^{-1}, even at a grain size of 10 nm, $\sim$ 90% of the deformation is caused by grain boundary contributions. Together with the deformation behaviour of the grain boundary phase, this leads to

an inverse Hall-Petch relationship for small grain sizes at low strain rates. Comparing normalized stress[1]-strain curves to experimental data of Ni, they get good agreement for the ascending part of the curve. Since the model was developed for Cu and is compared to only one set of experimental Ni data, the reliability of this model seems somehow limited.

In a study conducted by Schuh et al. [23] the hardness of NC NiW is investigated for grain sizes < 16 nm. They compare their own electro-deposited Ni-(11-14)W (grain sizes 6 - 10 nm) with electro-deposited Ni-(18-23)W reported in [24]. In both individual sets of hardness measurements, a trend towards inverse Hall-Petch behaviour can be seen with a maximum hardness at ∼ 7-8 nm. In [23], it is mentioned that care should be taken since, although expected to be negligible, solid solution strengthening was not taken into account. In addition, they emphasize that the hardness data obtained may not only depend on the grain size, but also on other factors (e.g. grain morphology, texture, porosity or defects).

The above-mentioned examples show that there is still some ambiguity in the experimental studies concerning an inverse Hall-Petch relationship. They mostly do show a clear deviation from classical Hall-Petch behaviour for small grain sizes (reduced hardening with decreasing grain size), but the significance for the proof of a real inverse Hall-Petch behaviour can sometimes be doubted, due to either imperfect samples (as mentioned in [14]) or to significant uncertainties in the evaluation of hardness or tensile strength (e.g. tensile strength in [25]). Despite the necessity for further experimental investigation to further increase the understanding of deformation mechanisms at the lower end of the NC length scale, a trend towards the inverse Hall-Petch relationship is visible and also strongly supported by simulations.

For a list of reviews including some of the above-mentioned literature, see table 1 in [4].

1.2.2   Irradiation

Several studies were conducted comparing the response of NC and coarse-crystalline materials (metals, intermetallics, oxides) on irradiation yielding ambivalent results. A comparison of the defect accumulation upon ^{12}C irradiation between NC (23 nm) and coarse crystalline Au showed an increased

---

[1]Normalized stress here denotes stress divided by shear modulus

and a decreased defect recovery capability in the NC material for 300 K and 15 K, respectively [26]. NiTi with a grain size of 23-31 nm irradiated with Ar ions showed an amorphization at much higher doses than coarse-crystalline NiTi [27]. A similar result was obtained for the complex oxide $Gd_2(Ti_{0.65}Zr_{0.35})_2O_7$: The NC (18±7 nm) oxide retained its crystalline structure even after a dose that was approximately three times higher than the dose required for amorphization of the coarse crystalline oxide. Apart from the grain size, the chemical order was also proposed to have an influence on the irradiation behaviour in this case [28]. On the contrary, it was shown that NC (1.5 nm) ZrO_2 amorphizes relatively easily, even upon irradiation with ions as light as Ne, whereas coarse ZrO_2 has never been reported to get amorphous upon ion irradiation [29]. Wurster and Pippan point out that defect annihilation in NC materials is strongly related to grain boundary sinks, making higher grain boundary volumes (smaller grains) beneficial for irradiation resistance. Very small grains, however, will facilitate amorphization due to the high excess free energy of the grain boundary volume. For an optimum irradiation resistance, both these factors have to be taken into account [30].

Recently, multiscale simulations of radiation-induced defects near grain boundaries in Cu revealed interesting mechanisms explaining the radiation resistance of NC materials [31]. Consistently with results of previous studies of Ni and Fe [32], a grain boundary close (up to a few nm) to the primary knock-on atom gets loaded with interstitial atoms that were displaced due to the collission cascade. In [31] it was found that the vacancies created by the cascade can be annihilated relatively easily by emitting the interstitials from the loaded grain boundary. This process has a lower activation energy than bulk vacancy migration and therefore has more potential to facilitate irradiation resistance by defect annihilation than regular vacancy migration has. Together with other effects (e.g. reduction of the vacancy migration barrier by the loaded grain boundaries), the simulation greatly improves the understanding of the influence of grain size on the irradiation resistance in NC materials.

1.3   Severe Plastic deformation

Nanomaterials can be made by arrangement of atoms from a non-crystalline atomic setup in a gaseous (e.g. various deposition methods [33], inert gas condensation [34]), liquid (rapid cooling, electrodeposition [35, 36]) or solid phase (crystallization of amorphous materials [37]). These methods are called bottom-up methods (in a broad sense of the term). The other approach for the production of nanostructured materials is the top-down method. Here, a large number of lattice defects is introduced in initially coarse-crystalline materials leading to an accumulation of defects and a large number of grain-boundaries until the grain-size gets decreased to the nanoscale [4].

To get a bulk non-porous nanostructure, a consolidation or compactification step is needed for methods that produce nanopowders or porous materials. This can be the case for both bottom-up (deposition and condensation processes) and top-down approaches (e.g. ball-milling). A prominent family of techniques that produce bulk nanostructured materials without the need for further consolidation or compactification is severe plastic deformation [5]. Some SPD techniques will be introduced in this section.

1.3.1   Equal channel angular pressing (ECAP)

ECAP (also denoted by ECAE - Equal channel angular extrusion), an SPD technique where a billet is deformed by "pressing it through intersecting channels of equal cross-section", was first proposed by Segal et al. [38]. Later work of Valiev et al. [39] made the method popular and it has been applied on a wide variety of materials since then (for a review, see [40]). In Fig. 1.2, a sketch of an ECAP device is shown. A plunger (darker blue) presses the sample (red) through the die (grey), that consists of two channels with an equal cross section inclined by an angle ϕ, which is usually chosen close to $90°$. The arc curvature angle Ψ of the round shape at the outermost sample path can be chosen between $\Psi = 0°$ (i.e. a sharp corner) and $\Psi = 180° - \phi$ (as depicted in fig. 1.2). Often, $20°$ is chosen as the arc curvature angle [41]. Back-pressure can be applied optionally (light blue plunger) and it was shown that this can have some beneficial effects (e.g. suppression of cracking, decrease in final grain size, more uniformity in the deformation
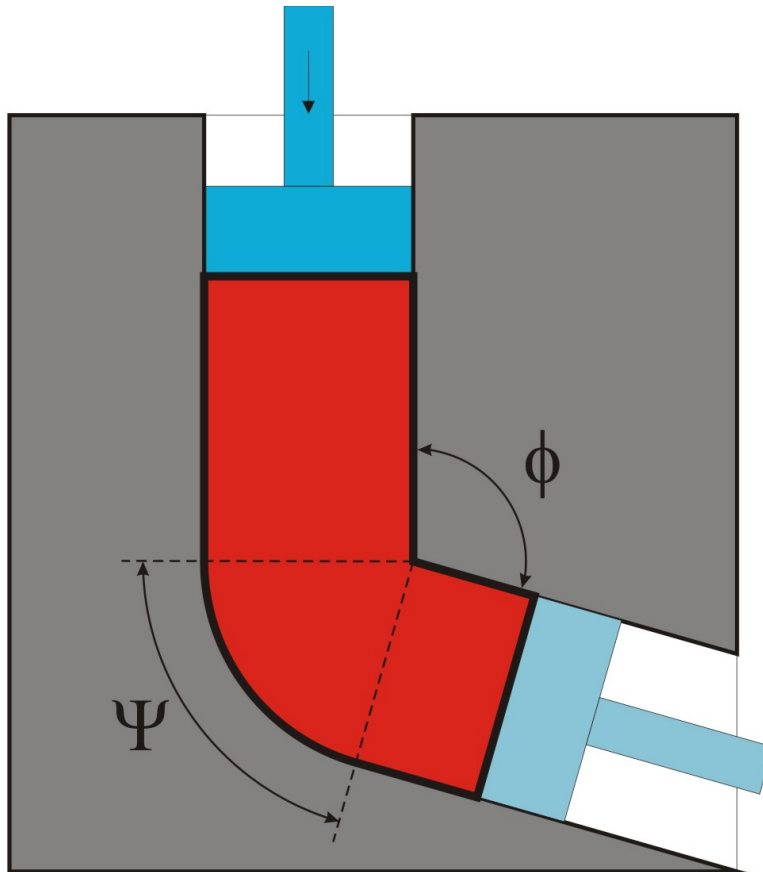
Figure 1.2: Sketch of the ECAP technique. A plunger (blue, at the top of the image) pushes the sample (red) through a die (grey). Optionally, back pressure can be applied by a second plunger (lighter blue, bottom right). The inclination angle ϕ and the arc curvature angle Ψ have an influence on the strain imposed per pass.

process) [42]. Since the shear strain imposed follows the equation

$$\epsilon = \frac{N}{\sqrt{3}}[2cot(\frac{\phi}{2} + \frac{\Psi}{2}) + \Psi cosec(\frac{\phi}{2} + \frac{\Psi}{2})] \ [43] \qquad (1.2)$$

with N being the number of ECAP passes, the shear strain imposed per cycle is close to 1 for the above-mentioned typical choices for Ψ and ϕ. To get strains much higher than 1, obviously consecutive ECAP passes have to be done. There are four basic routes with different rotation schemes for the reinsertion of the ECAP sample after an ECAP pass (A, B_A, B_C and C). The choice of the deformation route controls the amount of redundant strain (i.e. slip of one pass is cancelled by slip of one of the consecutive passes) and the slip systems activated. For a detailed description of the deformation routes and their effect see [40].

Comparing ECAP to other popular SPD methods, it is apparent that the possible bulk sample size in ECAP processing is larger than in other SPD techniques. Srinivasan et al. showed that ECAP processing of Al alloy samples having a square cross section with 100 mm side length is possible [44]. This possibility for upscaling is important particularly for industrial application of SPD materials. A downside of ECAP for some applications is the larger minimum grain size that can be achieved, as compared to, for example, HPT [41], often leading to submicron rather than truly NC samples.

1.3.2   High pressure torsion (HPT)

In HPT, a sample is placed between two plungers. The plungers exert high pressure (several GPa) on the sample and are rotated against each other, leading to torsional deformation of the sample, provided that the friction between plungers and sample is sufficient. The first concept of an apparatus similar to modern HPT devices was proposed in 1935 by the later Nobel laureate P.W. Bridgman [45]. In the 1980s, the HPT method was applied to several metals and alloys and at the end of the decade, a publication about low-temperature superplasticity achieved by HPT-processing [46] and subsequent systematic development of HPT as a processing technique to change materials properties by the same research group generated a world-wide interest in HPT [7]. Several different HPT geometries were developed in the meantime. The one used in this work (quasi-confined geometry) is
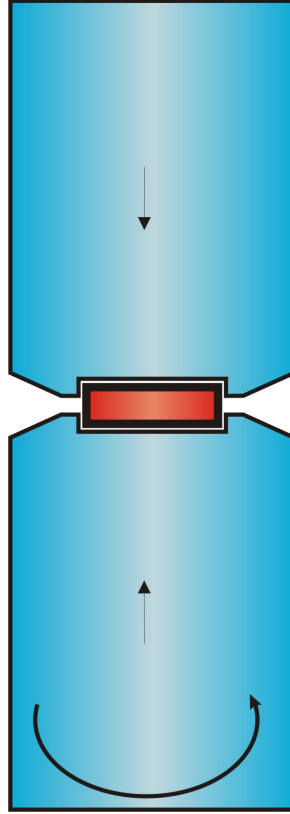
Figure 1.3: Sketch of the HPT technique. The upper and the lower plunger (blue, cylindrically symmetric) are pressed against the cylindric sample (red). The lower anvil is rotated against the upper one, inducing a shear deformation in the sample.

sketched in Fig. 1.3. In the case of quasi-confined geometry HPT, there is some material flow out of the cavity in the initial stages of deformation (compression and early rotation stage). The friction of the material in the gap between the plungers then limits and eventually stops further flow of material and causes a quasi-hydrostatic pressure within the cavities [47]. To calculate the shear strain imposed by an HPT deformation, the following method is usually used (cf. Fig. 1.4): For infinitesimal rotations the shear strain γ (displacement divided by height) is $\mathrm{d}\gamma = \frac{R\mathrm{d}\theta}{h}$ and therefore [7]

$$\gamma = \frac{R\theta}{h} = \frac{2\pi N \cdot R}{h} \qquad (1.3)$$
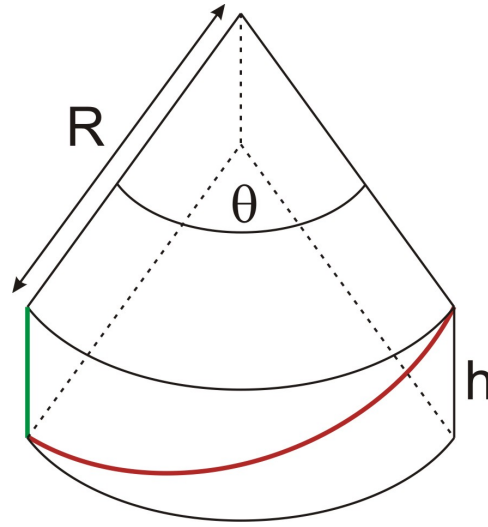
Figure 1.4: Visualization for the determination of the shear induced by HPT. The green vertical line is sheared into the red line by rotating the upper plunger by the angle θ. From geometrical considerations for infinitesimal rotation angles, equation 1.3 can be deduced

with R being the radius from the center of the HPT disk, θ the torsion angle, h the sample height and N the number of rotations.

Comparing HPT to other SPD methods, some advantages of HPT are apparent [48]:

- The ability to continuously impose shear strain to samples up to values that cannot be routinely achieved by other SPD methods ($> 100000\%$ nominal shear strain can be easily achieved, as shown in the course of this work).

- The possibility to deform brittle or high strength materials

- Relatively easy adjustment of the deformation temperature for devices capable of low/high temperature deformation (from liquid nitrogen temperature to several hundreds of degrees Celsius).

In addition, in the direct comparison to ECAP, grain sizes of deformed materials are usually smaller after HPT processing [49].

However, there are also some drawbacks of the HPT technique. One major challenge is the upscaling of HPT samples. Usually, HPT disks are

$\sim$ 10 mm in diameter and less than 1 mm in height. Recent attempts to increase the sample height lead to the appearance of major inhomogeneities not only in the lateral (that is reasonable from eq. 1.3), but also in the axial sample dimension [49, 50]. By choosing appropriate deformation parameters (e.g. elevated deformation temperature [50]) and most notably by upscaling the whole HPT device to get low height to diameter ratios and by choosing a special sample geometry, these challenges could be mastered for single phase iron as was shown by Hohenwarter et al. [51]. However, as mentioned in [51], especially for large samples, and as shown in the course of this work for standard size samples, the issue of homogeneity in HPT samples is an up-to-date topic that is not resolved yet and especially for alloys and compounds needs further investigation.

1.3.3   Repeated Cold Rolling (RCR)

Repeated rolling and folding was already used in the 1980s as an alternative process to rapid quenching and mechanical alloying to obtain amorphous metallic alloys [52]. Different elemental foils were stacked and by repeated rolling and folding, the elements were mixed and the material was finally amorphized. Explicitly as an SPD process, repeated rolling and folding (cf. Fig. 1.5) was first proposed and applied to Al by Saito et al. in the late 1990s [53, 54]. The deformation was conducted at elevated temperature to achieve better bonding. In between the folding steps, which are preceded with cutting the sheets, the surfaces were degreased and wire brushed. The term that was used for this SPD method was accumulative roll bonding (ARB) and resulted in a submicron grain size ($<$ 500 nm) for several materials (Al, Al-Mg alloy, steel). The term ARB got widely accepted for repeated rolling with intermediate foldings when degreasing and wire brushing are conducted in between the folding steps.

A few years later it was shown that repeated cold rolling (i.e. at room temperature) with intermediate foldings (denoted Folding and Rolling - F&R) can be used to achieve truly NC metallic samples [55]. For Ni, it was shown that after 80 passes of rolling and folding and a short subsequent annealing treatment for the relaxation of the microstructure, a grain size of less than 10 nm could be achieved. For Ti and Zr, the grain size achieved after 80 passes was $\sim$ 80 nm. These grain sizes are extremely small for SPD-processed pure metals and especially the grain structure of Ni (6-7 nm
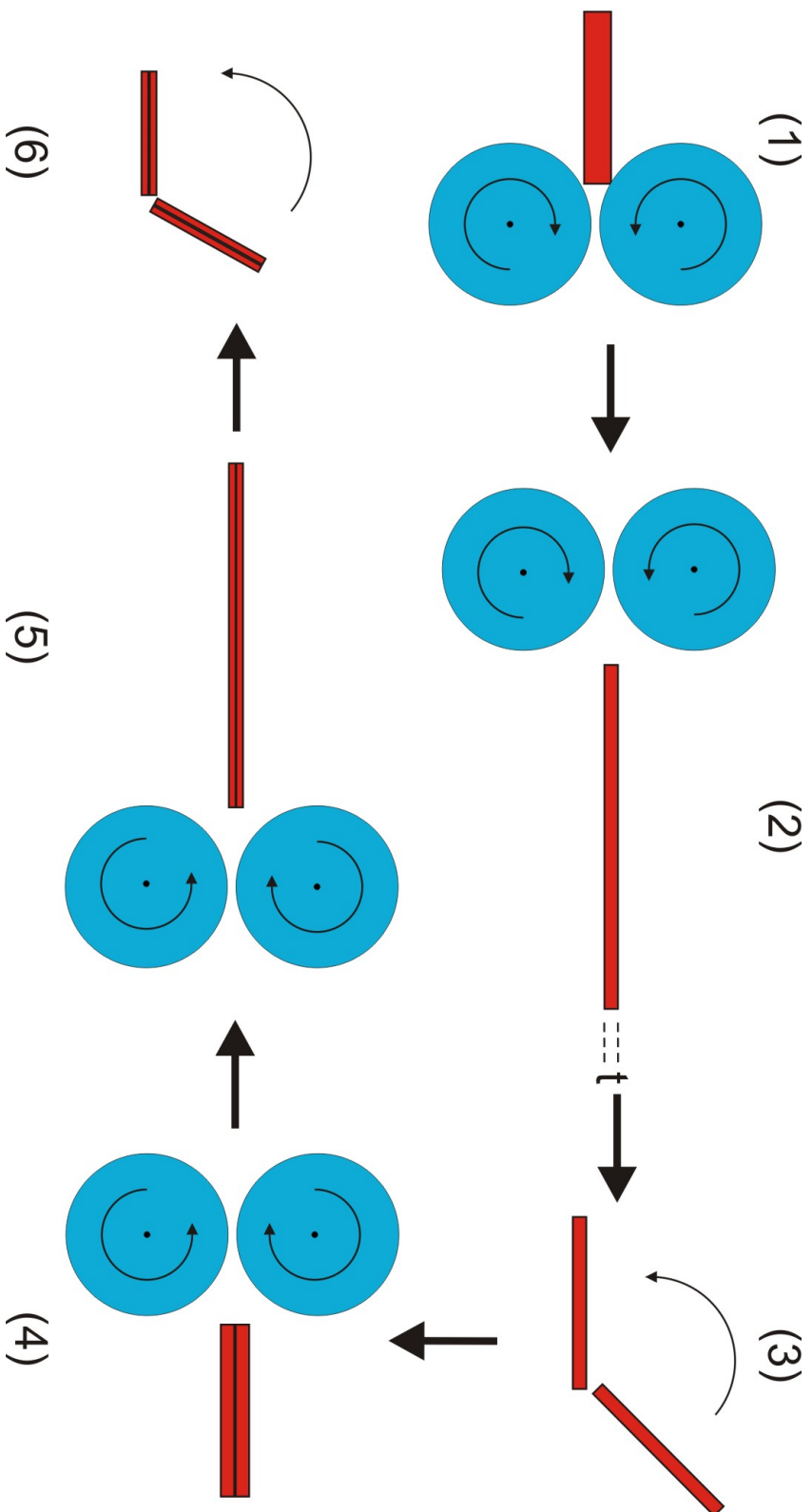
Figure 1.5: Sketch of the RCR process. By cold rolling (1-2), the thickness of a sheet (red) is reduced to thickness t (2). The sheet is folded and stacked (3). The stack is now rolled from thickness $2t$ down to thickness t in a single or in multiple rolling passes causing bonding of the sheets (4-5). Folding and stacking the sheet again (6) allows to repeat steps 4 to 6 to reach - in principle - an infinite number of foldings.

after 80 rolling and folding passes [56] can be most likely refined stronger than in any other SPD process.

To be able to compare the strains imposed by different SPD techniques to the one imposed by RCR, the strain ϵ imposed by one RCR pass (consisting of one folding and a subsequent thickness reduction of 50% to achieve the same thickness as before the folding step) was calculated. Under the assumption of the von Mises yield criterion for the plane strain condition, the equivalent strain can be expressed as [54]:

$$\epsilon = (\frac{2}{\sqrt{3}} ln(\frac{1}{2})) \cdot n \approx -0.8n \qquad (1.4)$$

with n being the number of rolling and folding passes.

Apart from the potential to achieve extremely small grain sizes for pure metals and sometimes amorphization for alloys and compounds (e.g. $Cu_{60}Zr_{40}$ [57]), processes involving rolling and folding of samples also attract interest because rolling is a process already widely used in industry and thus, the equipment needed is not very special [58] (in contrast to HPT and ECAP devices) and upscaling might be more feasible for RCR than for other SPD processes.

1.4 The Intermetallic Compound Zr₃Al and the Zr-Al system

1.4.1 The Zr-Al system

The phase diagram of the Zr-Al system (cf. Fig. 1.6, for quantitative equilibrium data, see [59]) exhibits eight stable low-temperature and two stable high-temperature intermetallic compounds all of which were repeatedly confirmed experimentally (for references, see [60]). In addition, several metastable intermetallic compounds were found [61]. Some of the metastable phases were reported to be stabilized by impurities (e.g. Oxygen impurities stabilize the Mn_5Si_3-structured polymorph of Zr_5Al_3 [62]). Using ab-initio methods, Ghosh and Asta [60] calculated the formation enthalpies of the stable low-temperature phases and found that the ground-state convex hull is defined by only five phases at 0 K (i.e. only these five phases should be stable at low temperatures). More recent ab-initio calculations yielded
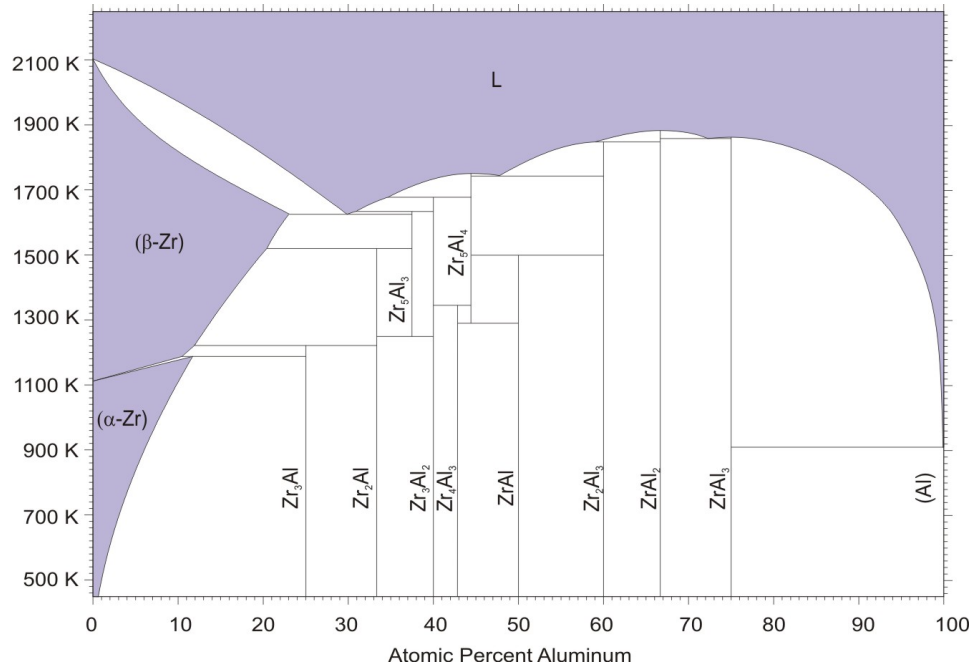
Figure 1.6: Phase diagram of the Zirconium Aluminum System [61]

formation enthalpies that are in better agreement to the experiments [63]. Only ZrAl has a formation enthalpy that lies significantly above the convex hull at 0 K, the other seven phases are predicted to be stable.

The narrow composition range of the intermetallic compounds in the Zr-Al system and thus very prominent two-phase regions in the phase diagram are explained by Alatalo et al who studied the Zr-Al system using all-electron full potential linearized augmented Slater-type orbital calculations [64]. They found that the heats of formation per atom of all the low-temperature phases (except $ZrAl_3$) lie almost on a straight line when plotted against the chemical composition. This means that small deviations from stoichiometry raise the enthalpy of a single phase above the common tangent line between two phases, thus making a phase mixture energetically favourable (cf. case (a) in Fig. 1.7).

On the Zr-rich end of the Zr-Al phase diagram, two different Zr solid solutions and the compound Zr_2Al can be found apart from Zr_3Al, which will be introduced in section 1.4.2. It was reported several times that Zr_3Al cannot be produced as a single-phase material, but that there is always some residual Zr solid solution or Zr_2Al or both in the samples [65, 66, 67].
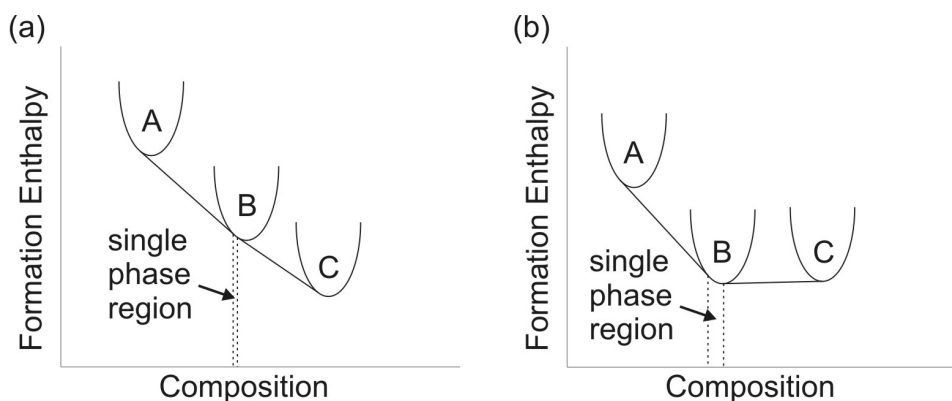
Figure 1.7: Schematic of the formation enthalpies of two different binary systems. In (a) the minima of the formation enthalpy curves lie almost on a straight line. The composition range in which the single B phase has a lower enthalpy than phase mixtures (i.e. between the intersections of the B free energy curve with the tangents) is rather small. In (b), the single B phase is energetically favourable to phase mixtures in a larger composition range.

The Zr(Al) solid solution exists in a body-centered cubic high-temperature β-phase and in a hexagonal close-packed low-temperature α-phase. The transition between those phases occurs at 1139 K for pure Zr. For the highest possible Al concentration (8.3 at%) the α-phase is stable up to to 1183 K [68]. The intermetallic compound Zr_2Al is $B8_2$-structured (prototype Ni_2In, space group $P6_3/mmc$) and stable up to 1488 K [69].

1.4.2 The Intermetallic Compound Zr_3Al

The intermetallic compound Zr_3Al is of the $L1_2$ structure (prototype Cu_3Au, space group $Pm\bar{3}m$), i.e. face-centered cubic with the Zr atoms sitting at the face-centered sites and Al sitting at the corners of the cube (cf. Fig. 1.4.2). The lattice parameter is 0.438 nm [69]. It is a line compound stable up to 1292 K. At this temperature, it dissolves into bcc β-Zr and Zr_2Al [68].

The compound was subject of intense investigations in the 1970's due to several properties that made it interesting for the potential replacement of the Zircaloy Zr alloys as a cladding material for nuclear reactors [70]: Zr has a very low thermal-neutron capture cross section [71]. The problem of low strength and also low corrosion resistance of α-Zr can be overcome by addition of 20at% or more Al, which results in the transformation from
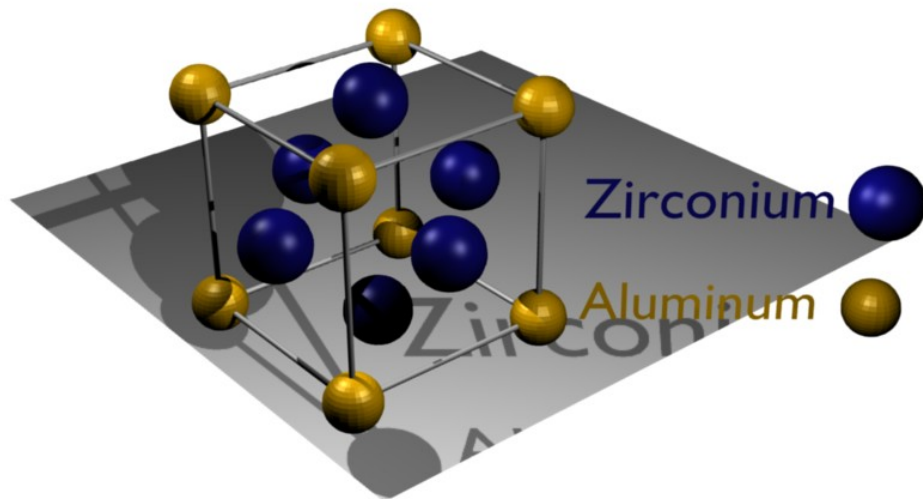
Figure 1.8: Schematic of the L1$_2$ structure.

α-Zr to Zr_3Al in a major fraction of the sample volume. On the other hand, addition of more than 25at% Al leads to the formation of Zr_2Al resulting in a loss of room-temperature ductility [72]. Thus, the compound Zr_3Al seemed to be a good candidate for nuclear applications and the formation mechanism of the intermetallic phase Zr_3Al [73] and several of its macroscopic properties (e.g. work-hardening [74], yield strength [75], oxidation behaviour [76]) were studied. Unfortunately, investigations of Zr_3Al irradiated with fast neutrons [77, 78] revealed a complete loss of ductility. Since the material did not preserve its good ductility, which was found in the unirradiated state [79] after irradiation, it was not possible to use it as a reactor material.

Another, more recent, field of research was the amorphization behaviour of Zr_3Al after different treatments. Mori et al [80] investigated the behaviour of several intermetallics upon electron irradiation and found that Zr_3Al stays crystalline. Hydrogen-bearing Zr_3Al, in contrast, was rendered completely amorphous by electron irradiation [65]. Hydrogenation alone was also shown to render Zr_3Al amorphous at sufficiently large ratios $\frac{H}{Zr_3Al}$ [67]. Ion irradiation also lead to complete amorphization of Zr_3Al [81, 82]. Benameur and Yavari showed that upon mechanical attrition, Zr_3Al becomes amorphous relatively fast compared to other $L1_2$ compounds (Ni_3Ge, Ni_3Al) [83]. In general, it was found that Zr_3Al has a more pronounced tendency for amorphization than Ni_3Al for a number of various treatments [84].

Another fact that makes Zr_3Al an interesting $L1_2$ compound is its dislocation dissociation structure. In $L1_2$ compounds, superlattice dislocations with the Burgers vector $\vec{b} = a\langle 110 \rangle$ can dissociate according to two schemes in the octahedral slip mode (i.e. slip occurs on $\{111\}$ planes), comprising either antiphase boundaries (APB) or superlattice intrinsic stacking faults (SISF) (Further dissociation of the $\frac{1}{2}a\langle 110 \rangle$ superpartial dislocations and the $\frac{1}{3}a\langle 211 \rangle$ super Shockley dislocations as well as cubic slip, that occurs at high temperatures, is discussed in detail in [85].):

$$a\,[110] \rightarrow \frac{1}{2}a\,[110] + APB + \frac{1}{2}a\,[110]\;\;(Scheme\;1) \qquad (1.5)$$

$$a\,[110] \rightarrow \frac{1}{3}a\,[21\bar{1}] + SISF + \frac{1}{3}a\,[121]\;\;(Scheme\;2) \qquad (1.6)$$

Contrary to most $L1_2$ alloys, in which dislocation dissociation occurs predominatly according to Eq. 1.5 at room temperature [85], superlattice dislocations in Zr_3Al dissociate according to eq. 1.6 generating SISF at room

type	plane	energy $[\frac{mJ}{m^2}]$	T [K]	source
SISF	111	70-90	293	Howe [71]
SISF	111	2	673	Holdway [86]
SISF	111	15±10	293	Douin [87]
SISF	111	9±4	77-293	Shang [88]
SISF	111	20±4	823	Shang [88]
APB	100	30-45	873-1073	Holdway [86]
APB	100	220±30	293	Douin [87]
APB	100	85±10	77-823	Shang [88]

Table 1.1: Fault energies of L1$_2$ structured Zr$_3$Al

temperature, as was shown in [71]. Studies at temperatures from 293 K to 1073 K showed that up to 673 K, octahedral slip with dislocations dissociating according to eq. 1.6 is dominant. At temperatures higher than 873 K, cubic slip becomes more and more important at the expense of SISF-dissociated octahedral slip [86]. RT studies of Douin [87] indicate that the dissociation scheme is not a function of temperature, but on the character of the dislocation. There, it is shown that parent dislocations with a character smaller than 40° dissociate according to eq. 1.5 and the rest according to eq. 1.6. This result is not in accordance with the results obtained by Holdway and Staton-Bevan [86]. A more recent study of the dislocation structures in Zr$_3$Al performed at temperatures from 77 K to 823 K arrives at the conclusion that dislocations comprising APB begin to slip at {111} planes. Screw dislocations cross-slip to a {100} plane while other parts of dislocations transfer to SISF-dissociation on {111} due to the lower energy of SISF as compared to APB on {111}. With increasing temperature, dislocations cross-slip faster to {100} and thus, less SISF are created. APB on {111} planes were not encountered in this study [88]. Similar to the findings of the above-mentioned investigations, the estimations of the energy of the planar faults in Zr$_3$Al do not present a homogeneous picture either, as shown in table 1.1.

Concerning SPD of Zr$_3$Al, to the best of the author's knowledge, no studies were done so far apart from the work conducted in the course of this thesis.

1.5 Aim of this work

The aim of this work is to study the effects of SPD on the structural evolution of the intermetallic compound Zr_3Al using mainly electron microscopy methods. The correlation of dislocation dissociation behaviour of different $L1_2$ structured materials to the corresponding grain refinements in HPT and the deformation driven phase transformations are elucidated by a comparison of HPT-deformed Zr_3Al and HPT-deformed Cu_3Au and Ni_3Al, which are of the same crystal structure as Zr_3Al but show a different dislocation dissociation behaviour.

The structural evolution and the saturation structure of Zr_3Al after deformation by the use of two different SPD methods (i.e. HPT and RCR) is compared and principal differences in the deformation processes are analyzed. The thermal stability of metastable Zr_3Al produced by SPD and the products of annealing are studied.

Finally, the homogeneity of the HPT process is checked in three dimensions by an electron microscopy analysis of differently oriented samples prepared from HPT disks, since a few recent papers raised doubt about the homogeneity of structural refinement in the HPT deformation. This is done from the nanometer to the millimeter scale to get a profound knowledge of the effect of HPT on Zr_3Al.

Chapter 2

Experimental Procedures

In this chapter, basic concepts of the experimental methods used will be briefly explained. In addition, the experimental procedures used in the work presented in chapters 3 through 6 will be presented in more detail than in the individual sections of the corresponding chapters.

2.1 X-Ray Diffraction

X-rays can be used (and have been used for the last approximately 100 years) for the characterization of materials. According to the Bragg equation (cf. Fig. 2.1)

$$2dsin\theta = n\lambda \tag{2.1}$$

d lattice plane distance

θ diffraction angle

n integer number

λ wavelength

the result of a diffraction experiment can be used to determine the parameters of periodic lattices, e.g. atomic lattices in crystalline materials. Moreover, the peak shape of Bragg reflections can be analyzed and information about internal strains and crystalline defects can be obtained [89]. The Scherrer formula

$$B = \frac{K\lambda}{\beta cos\theta} \tag{2.2}$$
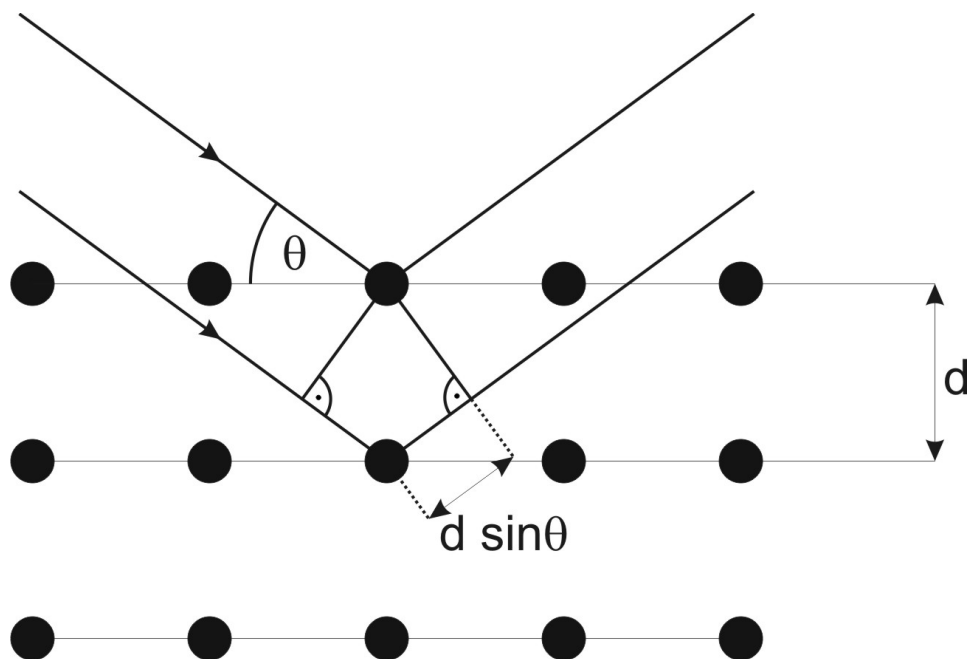
Figure 2.1: Schematic drawing of Bragg reflection for a crystalline material.

K shape factor

B CSD size

λ wavelength

β Full Width at Half Maximum (FWHM) of the Bragg peak

correlates the peak broadening to the coherently scattering domain (CSD) size. To minimize systematic errors caused by instrumental peak broadening, β is corrected in the following way (for Gaussian broadening): $\beta^2 = \beta_{measured}^2 - \beta_{standard}^2$ with $\beta_{standard}$ being the peak broadening measured for a coarse-grained sample (where peak broadening is affected by instrumental peak broadening only [90]). This works to a CSD size of up to several hundred nanometers (this number is strongly dependent on the instrument used) because for larger crystals and the accompanying decrease of size broadening, the instrumental broadening becomes too dominant and therefore causes large uncertainties. Since the strain also influences peak broadening, it is often helpful to seperate size broadening and strain broadening. This can be done for example by using the Williamson-Hall plot: ($\beta cos\ \theta$) is plotted

against ($4 \sin \theta$) for several Bragg peaks. The slope gives the strain ϵ and the intercept with the y-axis gives $\frac{\lambda}{B}$ [91]. This way, the grain size or the CSD size (sometimes, the grain size or CSD size is multiplied with a correction factor of 0.8 - 1.0) can be determined without any contributions of strain broadening. It should be mentioned that, apart from the Williamson Hall plot, there are several other methods to evaluate grain sizes and strains from X-ray diffractograms (e.g. Warren-Averbach and modified Williamson-Hall) [92].

2.2 Transmission Electron Microscopy

TEM is a very powerful and versatile tool for the characterization of materials from the atomic scale to a scale of several tens of microns. TEM techniques have been intensely discussed in several textbooks (e.g. [93, 94, 95]). Out of the vast amount of different TEM methods that can be used for materials characterization (e.g. electron energy loss spectroscopy, electron holography, magnetic domain-sensitive microscopy (Lorentz-microscopy), electron tomography), the TEM methods used in this work will be very briefly sketched (i.e. bright-field imaging (BF), dark-field imaging (DF), high-resolution TEM (HRTEM) and energy-dispersive X-ray spectroscopy (EDX), cf. Fig. 2.2) and peculiarities of investigations of nanocrystalline materials will be mentioned.

2.2.1 Bright-field imaging

In BF imaging, in the back focal plane, where the DP is formed, all the electrons that are diffracted more than a certain angle away from the central beam impact on the objective aperture. Therefore, these electrons cannot interfere with other electrons anymore and are thus not involved in the image formation process. Via the intermediate lens and the projection lens system, the magnified image of the sample is projected on a screen. The requirement for a BF image is that no diffracted beam passes through the objective aperture. BF images are primarily sensitive to the orientation of the sample since regions in or close to Bragg orientation will cause stronger diffraction and will therefore lead to dark areas in the image, as shown in Fig. 2.3a. In addition, thick sample regions, high atomic numbers and many atoms in the ray path cause darker areas in the image [94, 96]. For

Energy-dispersive
X-ray specctroscopy

incident beam

sample

Objective lens

Diffraction pattern

Back focal plane

BF, DF, HRTEM
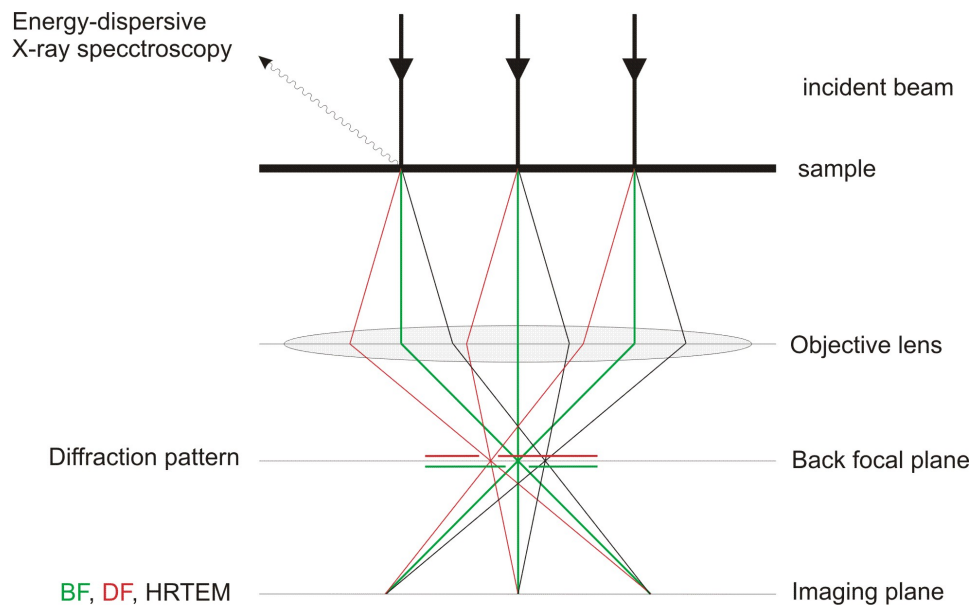
Imaging plane

Figure 2.2: Sketch of different TEM modes. EDX measures the energy of
the X-rays emitted by the sample. DP are formed in the back focal plane
of the objective lens. Images are formed in the imaging plane. Depending
on which rays are selected in the back focal plane, different imaging modes
are realized. Selecting the central (green) beam using the green aperture
(drawn slightly below the back focal plane for clarity) gives a BF image and
selecting a diffracted (red) beam gives a DF image. Without any apertures,
all the diffracted beams can interfere giving a phase contrast image (i.e.
HRTEM at sufficiently high resolution.)
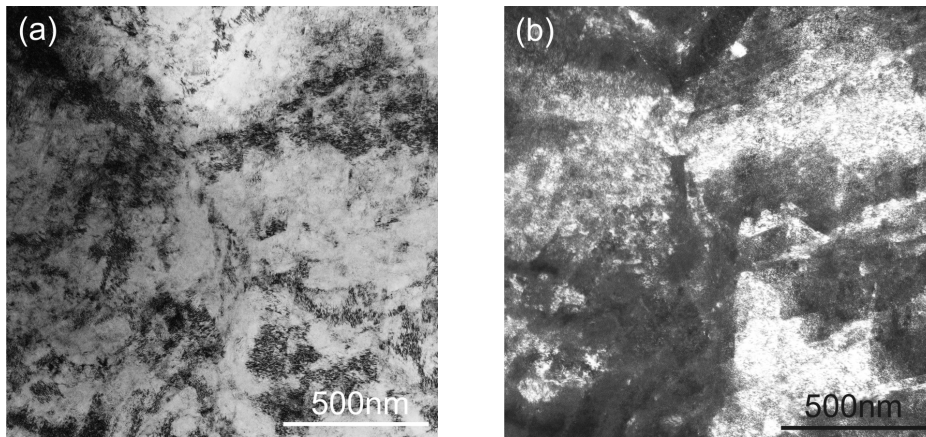
Figure 2.3: TEM images of the same area. (a) Bright-field image. Regions that are close to a Bragg orientation are darker. (b) Dark-field image. Areas with a crystal orientation that corresponds to the reflection selected by the objective aperture are bright.

a detailed analysis of the contrast of defects, image simulations including dynamic diffraction effects have to be carried out [97].

2.2.2 Dark-field imaging

In DF imaging, a special Bragg reflection is chosen and transmitted while all the other reflections (including the central beam) impact on the objective aperture. In order to reduce the effect of the spherical abberation on the image, the illumination of the specimen is usually tilted so that the transmitted diffracted electrons travel along the optical axis (known as centred dark-field). This method leads to bright areas in the image at the positions that contribute to the intensity of the selected diffracted beam [94], as shown in Fig. 2.3(b). All the bright areas in the image therefore have a similar crystal orientation with respect to the diffracting plane, provided that the areas have the same crystal structure. In the case of nanocrystalline materials, DF imaging allows an estimation of the grain sizes present in the specimen by measuring the size of bright areas in the image.

2.2.3 Selected area diffraction

To get a DP, the intermediate lens has to be adjusted in a way that the back focal plane of the objective lens is imaged on the screen or camera. To get
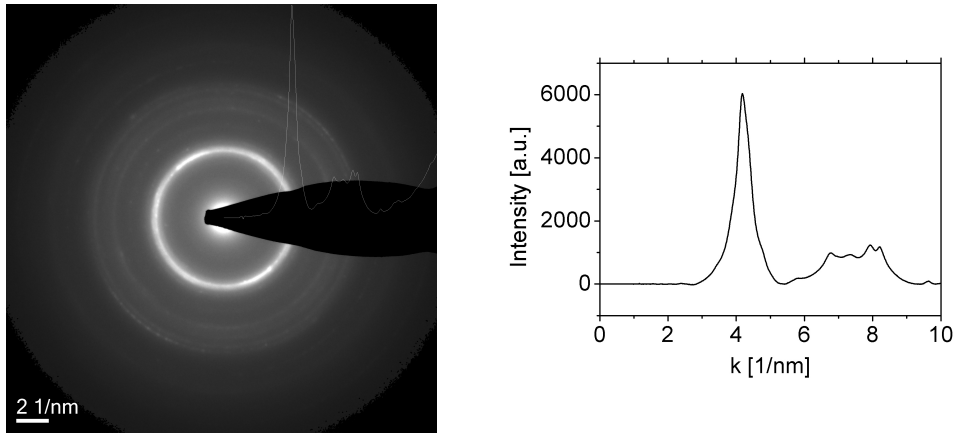
Figure 2.4: DP of NC Zr_3Al. The integrated, background-subtracted intensity profile is shown as an overlay in the DP and in the graph.

the diffraction information of an area of interest, a selected area aperture is inserted in the image plane of the objective lens.

In nanocrystalline materials, usually a lot of differently oriented grains are present within small areas leading to a transition from discrete spot patterns to ring patterns for decreasing grain sizes. After azimuthal integration and subsequent analysis of the ring patterns (e.g. using the Peak Analysis for Selected Area Diffraction (PASAD) software [98], cf. Fig. 2.4), intensities as a function of spatial frequencies are obtained. Under certain conditions, this allows an analysis of electron diffraction patterns analogous to X-ray diffraction profiles on a very local scale.

2.2.4 High-resolution TEM

Due to the interaction with the sample, the incident beam is split up into a central beam and diffracted beams. If no objective aperture is inserted or if multiple beams can pass the objective aperture, the beams can interfere. The intensity at a certain point on the screen is then dependent on the squares of the sum of the amplitudes and phases of the electron waves at that point. The phases of the electron waves are dependent on the electro-optical path length in the sample. This deviates from the real path length by a contribution of the potential along the way through the sample.

Neglecting relativtistic contributions, the wavelength of an electron in a

potential is

$$\lambda = \frac{h}{\sqrt{2me(E + V(x, y, z))}} \tag{2.3}$$

  h Planck constant

  m electron mass

  e elementary charge

  E kinetic energy of the electron

  V potential

Together with an integration constant $\sigma = \frac{\pi}{\lambda E}$ and the projected potential $V_t(x, y) = \int_0^t V(x, y, z)dz$, the phase shift $d\Phi$ is

$$d\Phi = \sigma V_t(x, y). \tag{2.4}$$

In this simplified model for thin specimens, contrasts in the image only arise because of phase shifts due to differences in the potential, which are caused by the atoms in the path of the electrons. This leads to the possibility of atomic resolution images in the TEM. HRTEM images are used in this work to support the identification of very small crystallites, which in DF images only show up as bright dots. Resolving these crystallites in high resolution is an unambiguous proof of their crystalline nature and allows to accurately determine their size and get information about intragranular lattice defects (e.g. twins and small lattice rotations).

2.2.5   Sample Preparation for TEM

A prerequisite for meaningful TEM results is a suitable sample thickness, i.e. less than ~ 100 nm for standard TEM methods (e.g. BF, DF) and less than ~ 10 nm for HRTEM. In this work, several different sample preparation methods were used. For plan-view TEM samples, electropolishing was used. The electrolyte, temperature and voltage used are described in the sections 'experimental details' of the following chapter. Cross section samples from defined areas (chosen using SEM images) were prepared using the focused ion beam (FIB) method. There, a small wedge is cut out of a specimen with a Ga ion beam. The wedge is lifted out of the specimen with a nanomanipulator

and subsequently thinned with the Ga ion beam until electron transparency is achieved.

A big advantage of the more time-consuming FIB method relative to electropolishing is the possibility to choose the position of the TEM sample with submicron precision whereas there is always an uncertainty in the range of a few tens of millimeters where the electron transparent region forms during electropolising. This is especially important in samples with an inhomogeneous microstructure at the scale of several tens of microns.

2.3   Scanning Electron Microscopy

Scanning electron microscopy (SEM) is a tool for materials characterisation from a scale of a few nanometers up to a few millimeters. A focused electron beam scans across the sample surface and electrons or photons emitted from the sample (backscattering of incident electrons, emission of secondary electrons, emission of characteristic X-rays) is detected. In this work, two SEM modes were used to get information about the grain structure of undeformed samples and the cross section phase structure of deformed samples:

Backscattered electron detection (BSED): Incident electrons are scattered in the material and some of the electrons are backscattered into the backscatter detector. Since the backscatter coefficient is dependent on the atomic number of the material, illuminating regions with a high average atomic number will cause a stronger signal in the backscatter detector [99]. Neglecting topographical contributions, this leads to a pure Z contrast image. This is in particular useful in the case of Zr_3Al because the distinction of different phases with different average atomic numbers (Zr: 40, Zr_3Al: 33.25, Zr_2Al: 31) can easily be done without the necessity of identifying either the crystal structure or characteristic X-rays.

Electron backscatter detection (EBSD): Similar to the case of BSED, backscattered electrons are detected. The major difference is that in the case of EBSD, the backscatter detector is an area detector (e.g. a CCD camera) making it possible to image diffraction patterns of the backscattered electrons [100]. In the course of this work, EBSD was used to identify the grain size of the initial material (cf. Fig. 2.5). However, it was not possible to get EBSD results of highly deformed samples. This might be due to the small grain size in combination with a high defect density in the severely

deformed material. In principle, it was shown that a resolution down to $\sim$ 10 nm is possible. In this context, it should be mentioned that a higher average atomic number enables a better spatial resolution in EBSD [101].

2.3.1 Sample Preparation for SEM

For cross section BSED samples, the HPT disks were cut in half. One half of the disk was then embedded in molten wax at 350 - 360 K. After solidification of the wax, the cross section surface of the sample was manually ground with diamond foils with subsequently decreasing grit sizes. The final abrasive size was 1μm because at smaller sizes, the surfaces got scratched relatively pronounced. Wax was used instead of epoxy resin because of its superior grinding properties, resulting in a very plane transition from wax to sample. This was beneficial because if there had been a difference in height between sample and the surrounding material, the sample edges would have been rounded resulting in a loss of information near the edges.

To get the surface quality that is necessary for EBSD investigations, samples were first mechanically ground with a 15 μm diamond suspension and a force of 30 N. Afterwards, the surface was mechanochemically polished using a chemically aggressive (pH 9.8) suspension based on SiO_2 (Struers OP-S) mixed with H_2O_2 in a 1:1 ratio for one hour. The EBSD preparation was done at the National Institute for Materials Science in Tsukuba, Japan.

2.4 Hardness testing

Apart from structural investigations using the above-mentioned methods, the hardness was studied for different deformation conditions. This was done on a Zeiss Axioplan optical microscope equipped with a microindenter for Vickers hardness measurements. With a load of 1.5 N, a diamond tip with a square-based pyramid shape is pressed into the sample with a load increase of 0.1 N/s. After holding the maximum force for 10 s, the tip is retracted and the indent is measured in the optical microsope (cf. Fig. 2.6). The hardness H is determined according to the formula:

$$H = \frac{1.854 \ F}{d^2} \qquad (2.5)$$

F load (force)
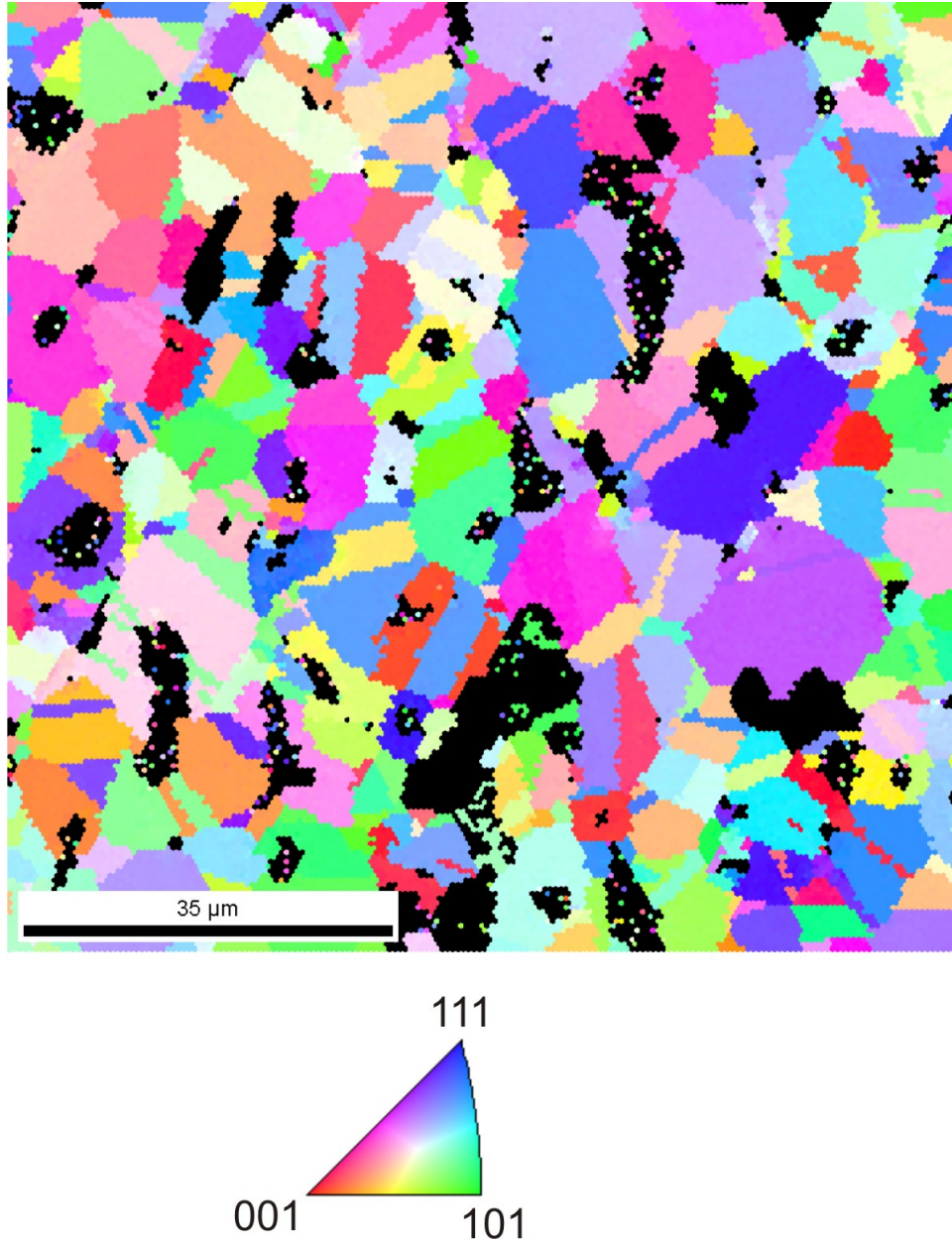
Figure 2.5: Crystal orientation map of undeformed Zr_3Al obtained by EBSD. The orientation of the black areas could not be identified, the colors correspond to orientations as seen in the orientation triangle below the map.
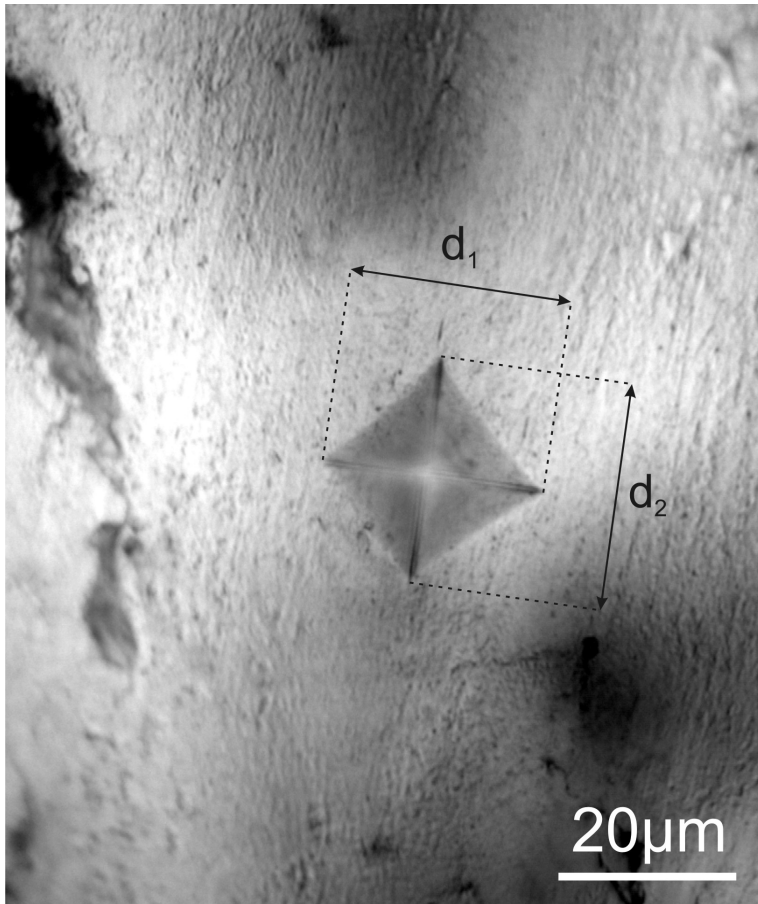
Figure 2.6: Optical micrograph of a Vickers indentation in a Zr_3Al sample that was compressed under a pressure of 4 GPa in an HPT device without any torsion. Inserting the average of d_1 and d_2 in eq. 2.5 gives the Vickers hardness of the material at the site of indentation, in this case 4.3 GPa.

d diagonal of the imprint

The above formula yields the Vickers hardness in SI units (i.e. Pa if the load and the diagonal are given in N and m, respectively). For the sake of completeness, it should be mentioned that the Vickers hardness is often given in kgf (kilogram force) per mm^2. To convert the latter to MPa, the following relation must be used: $9.81\ HV[\frac{kgf}{mm^2}] = HV[MPa]$.

2.5 Differential Scanning Calorimetry

Differential scanning calorimetry is an important tool for integral insight into the behaviour upon temperature change of materials. The principle of the DSC method used for this work (i.e. heat flux DSC using a Netzsch DSC 204 Phoenix) is the comparison of the heat fluxes between a reference and a sample that are kept at the same, but in general non-constant temperature. If exothermic or endothermic reactions occur in the sample that do not occur in the reference upon heating or cooling, the difference in heat fluxes provides information about the reaction enthalpy.

In metastable nanocrystalline (and also amorphous) materials, DSC is an important tool to determine amongst other material characteristics the thermal stability of the nanocrystalline (or amorphous) structure. The temperatures at which devitrification (in case of amorphous materials) and grain growth occurs can be measured. By integration of the peaks, the enthalpy of these reactions is determined. To assess the activation enthalpies of these processes, a Kissinger plot can be done (cf. Fig. 2.7): For various heating rates, $(ln\frac{\phi}{T_p^2})$ versus $(\frac{1}{T_p})$ (ϕ heating rate, T_p peak temperature) must be plotted. The negative slope of a linear fit of these values gives the activation energy for the corresponding process [102].
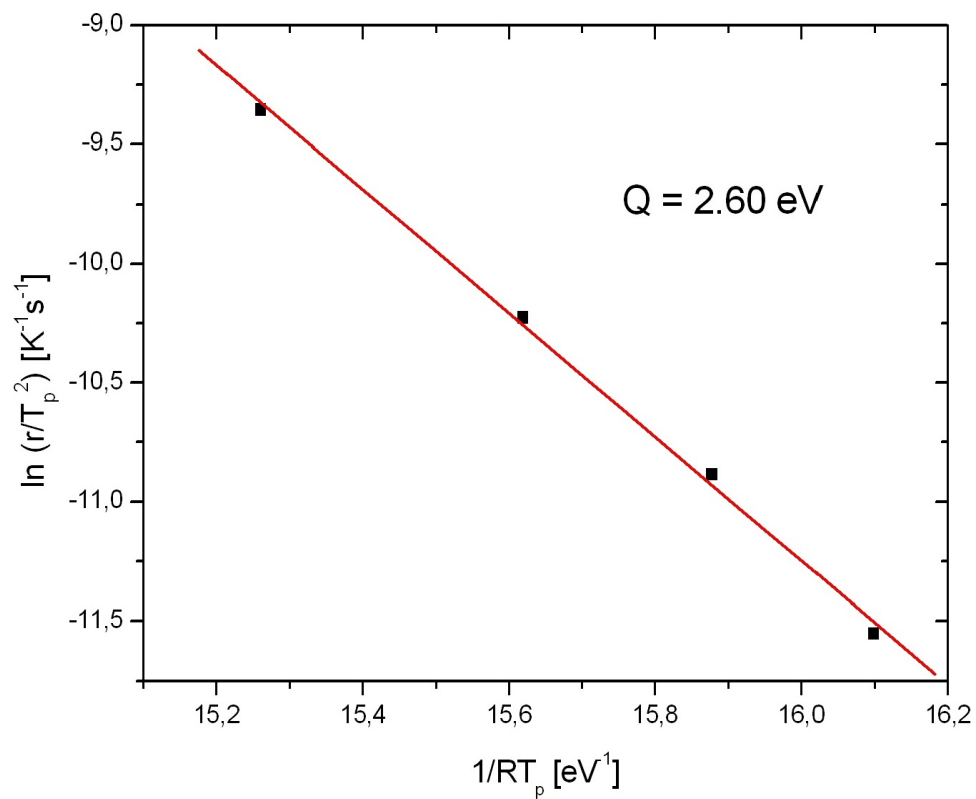
Figure 2.7: Kissinger plot of crystallization peak of Zr_3Al. The slope gives the activation energy.

Chapter 3

Plan view TEM of HPT deformed Zr_3Al[1]

3.1 Overview

The L1$_2$-structured intermetallic compound Zr_3Al can be rendered amorphous easily by several techniques. In the present study the structural evolution during high pressure torsion (HPT) was investigated systematically by transmission electron microscopy (TEM) methods. Zr_3Al samples were deformed at room temperature to different grades of deformation up to shear strains of 140 000%. TEM investigations revealed that the tendency to grain fragmentation, disordering and the formation of a nanocrystalline structure is weak compared to other L1$_2$ ordered alloys like Ni_3Al. In addition, an amorphous phase has not been encountered. The present results differ strongly from previous ones obtained from ball-milled materials. Possible reasons for the different behaviour are discussed on the basis of the temperature dependent dissociation scheme of the superlattice dislocations gliding in Zr_3Al.

3.2 Introduction

Zr_3Al (L1$_2$ long range ordered) was intensely investigated as a possible nuclear reactor material due to its corrosion resistance and low thermal-neutron capture cross section [66]. Deformation occurs by the glide of superlattice

---

[1]This chapter is based on publication [S1].

dislocations with Burgers vector $a \langle 110 \rangle$. Holdway and Staton-Bevan [86] reported two different dislocation mechanisms occurring in different temperature regimes. It was also discovered that Zr_3Al can be rendered amorphous by ion irradiation [81, 82], by hydrogenation [103] and by electron irradiation [65]. Benameur and Yavari [83] reported that amorphization of Zr_3Al by ball-milling is possible with milling times that are a lot shorter than those needed to amorphize Ni_3Al which is also a $L1_2$-structured compound. In this work, the effect of HPT on Zr_3Al is investigated. Samples were deformed to a wide variety of deformation degrees. The structural evolution of the HPT-processed Zr_3Al is compared to HPT-processed Ni_3Al and the effect of different deformation methods (ball-milling, HPT) on Zr_3Al is discussed.

3.3   Experimental Details

The composition of the material used was Zr-8.6wt.%Al. After alloying, it was kept at 1160K for 24 hours to support the transformation of the high-temperature phases Zr_2Al and α-Zr to the lower-temperature Zr_3Al-phase. The microstructure finally consisted of approximately 90% $L1_2$-structured Zr_3Al, the rest being Zr_2Al and α-Zr. Cylindric HPT-samples with a height of 0.6 to 0.8 mm and a diameter of 8 mm were punched by spark erosion. The samples were deformed at room temperature at a quasi-hydrostatic pressure of 4 GPa to shear deformations up to 140 000%. To avoid mismatch between nominal and actual degree of deformation caused by possible sliding between sample and dies, especially in the case of a large number of HPT turns, the samples were marked prior to HPT by two lines, one line above the other, on the top and on the bottom surface. After the deformation, the lines were still well-visible and changed their relative orientation according to the number of turns (e.g. they kept their relative orientation for an integer number of turns). Continuous measurement of the torque during HPT that did not show any anomalies is another argument for the consistency of nominal and actual degree of deformation. The hardness of the deformed samples was measured by micro indentation. TEM samples were punched out of the HPT discs and electropolished with a polishing solution consisting of 5% perchloric acid and 95% ethanol at 246 K and a voltage of 11V. TEM observations were carried out with a Philips CM 200 transmission electron microscope operating at an acceleration voltage of 200kV. Images
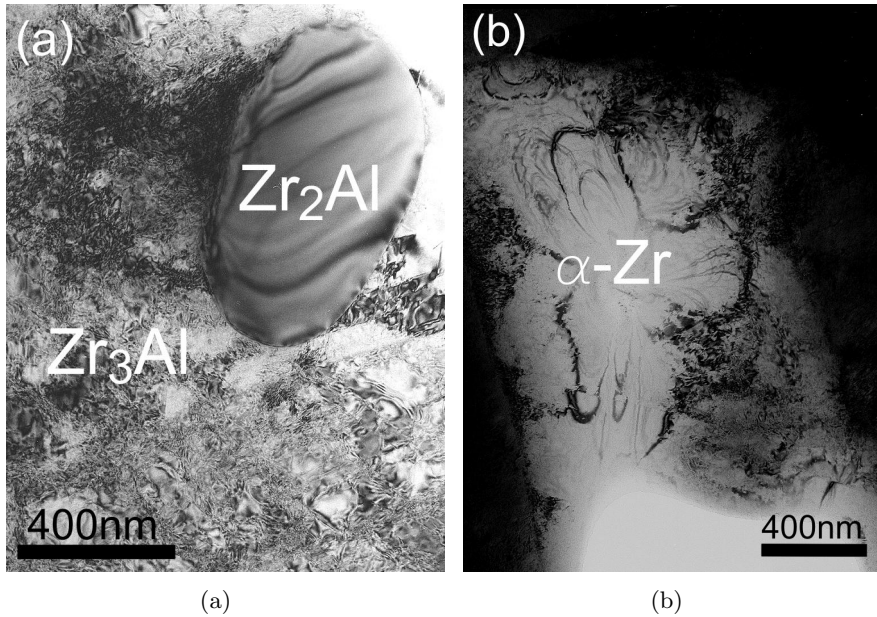
Figure 3.1: TEM bright field images of Zr-25at.%Al deformed to 600% shear strain. a) B8$_2$-structured Zr$_2$Al precipitate in L1$_2$-structured Zr$_3$Al. b) hexagonal α-Zr. Zr$_2$Al and α-Zr are nearly dislocation-free, whereas numerous dislocations can be seen in the Zr$_3$Al matrix.

and diffraction patterns of the material deformed to various grades were taken. To ensure that the investigated region is consisting of Zr-25at.%Al, energy-dispersive X-ray (EDX) measurements were conducted.

3.4 Experimental Results

3.4.1 Phase structure of Zr25at.%Al deformed to 600% shear strain

The material was investigated by TEM and EDX methods to elucidate the phase structure at relatively low degrees of deformation. Fig. 3.1 shows TEM bright field images of different areas corresponding to a nominal shear strain $\sim$ 600%. In the various crystal structures, differences in dislocation density can be seen. The corresponding compositions were measured by EDX. While the L1$_2$-phase Zr$_3$Al (74.1at.%Zr) shows quite a high dislocation density, the hexagonal α-Zr (96.7at.%Zr) and the B8$_2$-structured Zr$_2$Al

(66.7at.%Zr) phases are nearly dislocation-free. The contrast fringes visible in the latter phases are bend contours and originate from bent lattice planes; they are not a direct indication for crystal defects. This means that the deformation is accommodated mostly by the L1$_2$-phase, so it is reasonable to neglect the deformation accommodated by other phases than L1$_2$-structured Zr$_3$Al. It can also be seen that the electropolishing solution removes the phases differently. In Fig. 3.1a, the Zr$_2$Al is not as thin as the Zr$_3$Al matrix. In Fig. 3.1b, the α-Zr is surrounded by Zr$_3$Al that is not even thinned to electron transparency.

3.4.2   Structure of the Zr$_3$Al phase at 600% shear strain ($\frac{1}{4}$ turn)

Fig. 3.2 shows a TEM weak-beam dark field image of a single-phase Zr$_3$Al region in a specimen deformed to 600% shear strain. A dense network of dislocations can be seen. Nevertheless, the dislocation density is low enough for the identification of individual dislocations. Another feature of the image are numerous fringes, which correspond to superlattice intrinsic stacking faults (SISF). The SISF visible in Fig. 2 are located on {111} planes that are not in projection. The different orientations of the planes comprising the SISF lead to fringes along different directions.

3.4.3   Zr$_3$Al deformed to 14 000% shear strain (5 turns)

Fig. 3.3 shows dark-field images revealing fragmentation of grains by crystallographic boundaries and twin boundaries parallel to {111} planes. In the diffraction pattern, mirrored reflections are a clear evidence for a twinned structure. Fig. 3.3a and b are dark-field images of the same region taken using a {111} reflection of the twin and the matrix, respectively. The contrast varies not only at the twin boundary and the crystallographic boundaries, but also in the direction parallel to the twin boundary. This is due to slight variations of orientation within the twinned region caused by SPD. Streaks in the diffraction pattern parallel to {111} reflections indicate accumulations of SISF. Superlattice diffraction spots are clearly visible, thus order is preserved. Grain refinement is no major effect of the deformation process since the grain size is still in the order of magnitude of microns.
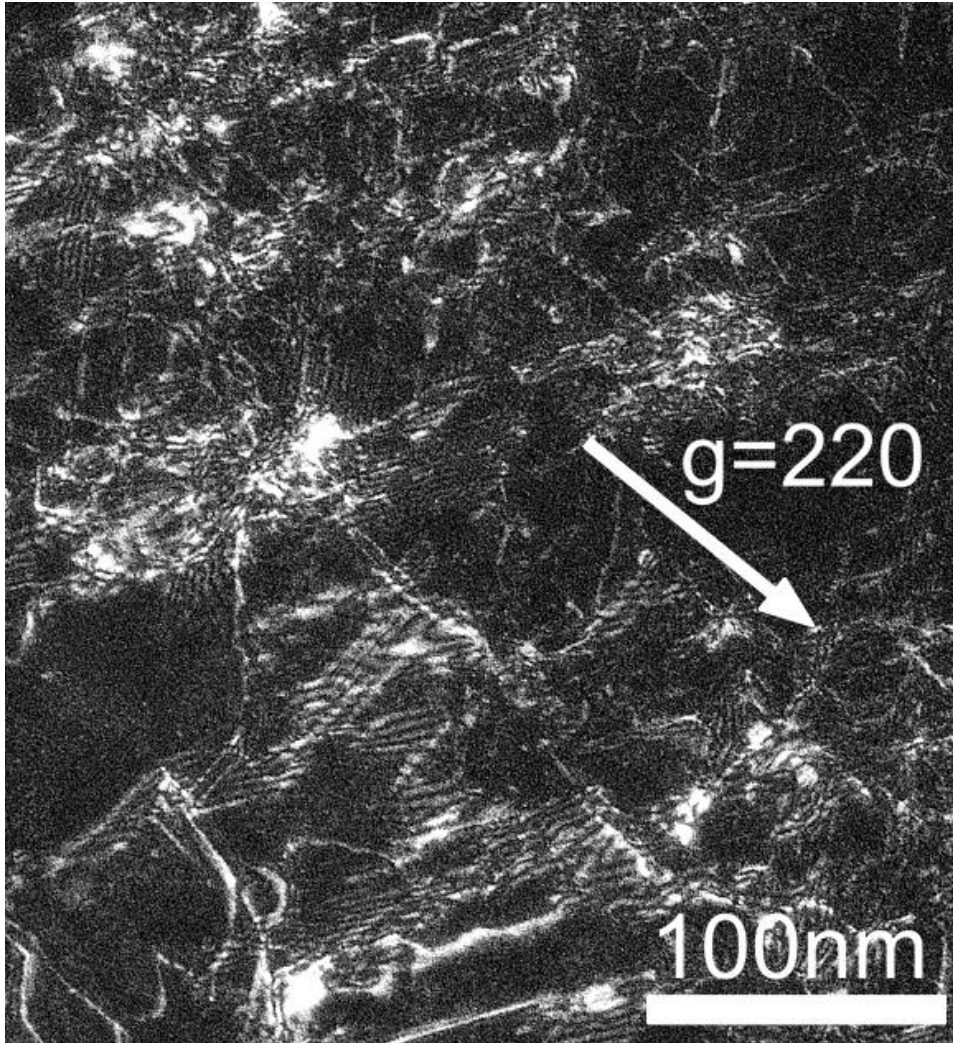
Figure 3.2: TEM weak-beam dark field image of Zr$_3$Al deformed to 600% shear strain (diffraction vector g=220 used for the image). Numerous fringes originating from stacking faults bounded by dislocations can be seen. Individual dislocations are also visible.
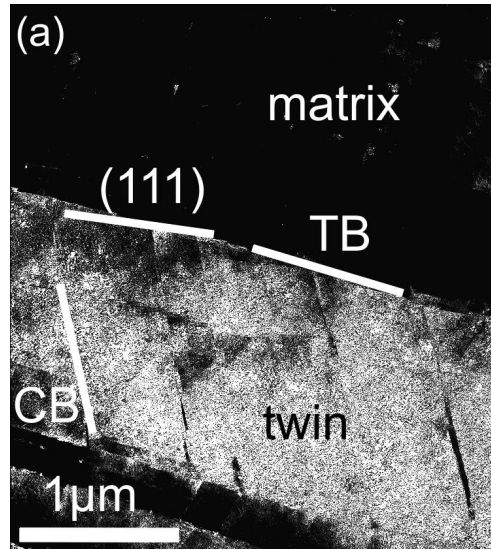
(a)
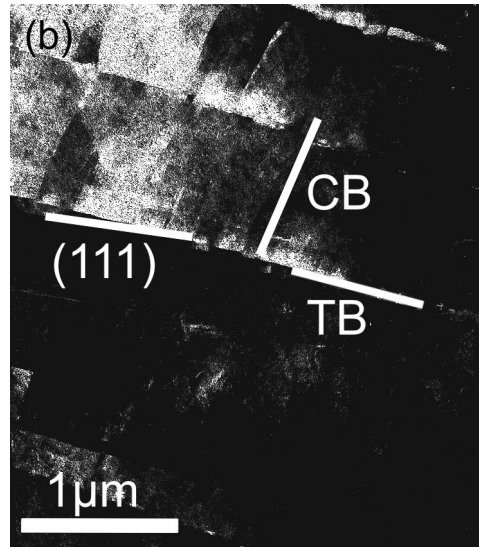
(b)

Figure 3.3: Dark field images of Zr_3Al deformed to $14\,000\%$ shear strain. a) and b) are taken using {111} twin and matrix spots, respectively. Abrupt change in intensity at the twin boundary (TB) and at crystallographic boundaries (CB) and continuous change of the intensity in the direction parallel to the twin boundary can be seen. Steps in the twin boundary result in a slight misorientation of the (111) plane to the corresponding twin boundary.

3.4.4 Samples deformed to 140 000% shear strain (40 turns)

Figure 3.4 shows a TEM bright-field image of a Zr_3Al region that was deformed to 140 000% shear strain. Like in the less-deformed samples, crystallographic boundaries parallel to {111} planes are observed. In contrary to the sample deformed to 14 000% shear strain, this sample does not show any indications for twinning. From the presence of streaks in the diffraction pattern it can be assumed that all crystallographic boundaries are composed of accumulated SISF-dissociated dislocations. The diffraction pattern still consists of a rather well-defined spot pattern, even after this extremely high grade of deformation. This means that the grain size is not significantly reduced by the SPD process and the variation of orientation is only small. It is important to note that like for the less-deformed material, superlattice reflections show that order is still preserved.

3.4.5 Microhardness measurements

Additional to the TEM investigations, measurements of the Vickers hardness were conducted via micro indentation. There is a significant difference in microhardness between undeformed and deformed samples. Within the deformed samples, the hardness values are mostly within the error bars. The grade of HPT deformation does not have a strong influence on the hardness of the material.

3.5 Discussion

In contrast to $L1_2$-structured intermetallic compounds like Ni_3Al [104] and Cu_3Au [105], Zr_3Al shows no sign of disordering or nanocrystallization upon HPT at room temperature. A possible reason is the difference in dislocation mechanisms. In Ni_3Al and Cu_3Au, a superlattice dislocation with Burgers vector $\langle 110 \rangle$ dissociates into two superpartials gliding on {111} planes with Burgers vector $\frac{1}{2} \langle 110 \rangle$ confining an anti-phase boundary (APB) (Fig. 3.5). The APB causes local disorder, so a large number of APB reduces the degree of order significantly. The different mechanisms leading to an accumulation of APB faults are described elsewhere [106]. For Zr_3Al, Holdway and Staton-Bevan [86] and Shang et al. [88] reported that superlattice dislocations dissociate into two superpartials with Burgers vector $\frac{1}{2} \langle 110 \rangle$ only at
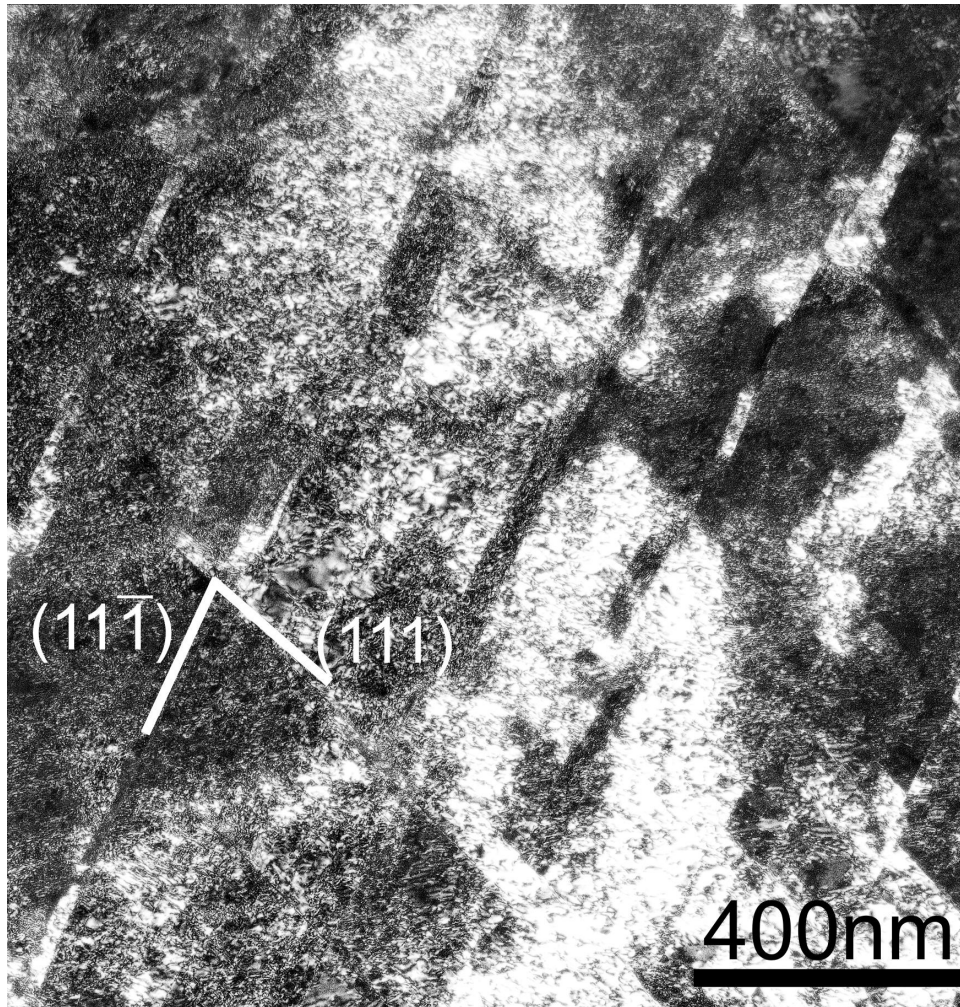
Figure 3.4: TEM bright field image of Zr$_3$Al deformed to 140 000% shear strain. The contrast indicates that the variation of orientation is only small.
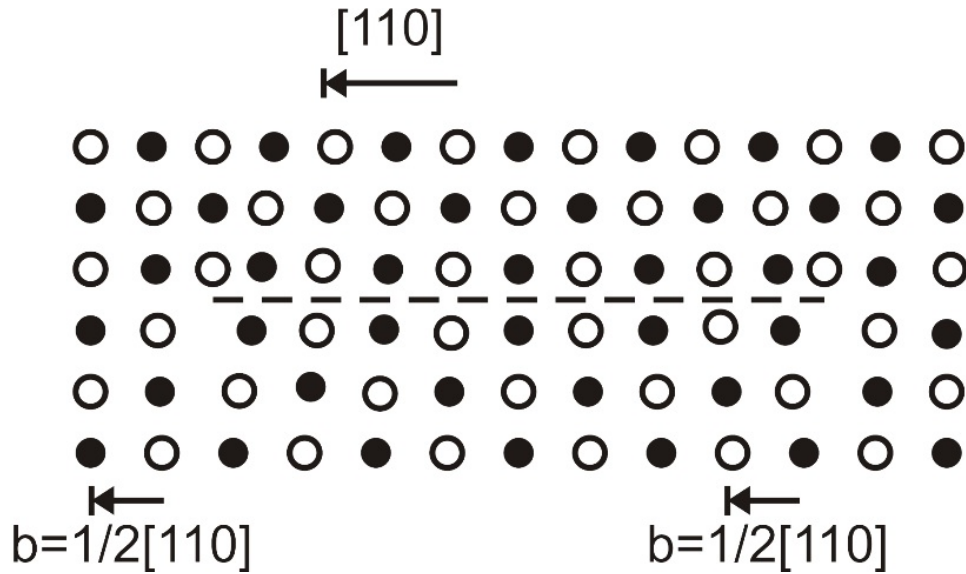
Figure 3.5: Schematic drawing of two $\frac{1}{2}[110]$ superpartial dislocations confining an APB (dashed line). At the APB, the order is destroyed.

elevated temperatures. In deformation experiments at room temperature, they found that SISF confined by super Shockley dislocations with Burgers vector $\frac{1}{3}\langle 211 \rangle$ gliding on $\{111\}$ planes are the predominant type of defect, a finding that is consistent with our TEM results. As our HPT experiments were conducted at room temperature, the lack of APB hinders disordering, since SISF preserve the ordered structure. Disordering is expected to cause a higher mobility of dislocations and therefore to assist nanocrystallization.

The ball milling experiments of Benameur and Yavari [83] showed that Zr_3Al is easy to amorphize by ball milling. Similar to our material, they used a $L1_2$ compound Zr_3Al with some residual Zr_2Al (that was not transformed to Zr_3Al) and possibly some α-Zr. One difference to our experiments is, apart from the different deformation method, the grain size of the initial material. Due to melt spinning prior to ball milling, their initial grain size was about 80 nm, while the initial grains in this work were several microns large. Moreover, a difference in temperature rise on a local scale may exist between ball milling and HPT. Suryanarayana [107] reported estimates of local temperature rises upon the impact of the milling balls up to 1000 K during ball milling for some materials. If the temperature rise during ball milling of Zr_3Al is sufficiently high to get the material in the temperature

regime of the deformation mechanisms resulting in APB (above 873 K [86]), then this significant difference to HPT possibly explains why disordering followed by amorphization happens for ball milled samples, but not for HPT-processed ones.

3.6   Summary

L1$_2$-structured ordered intermetallic Zr$_3$Al was deformed by HPT at room temperature. TEM investigations were conducted of samples deformed to shear strains ranging from 600% to 140 000%. Crystallographic boundaries consisting of SISF-dissociated dislocations arise on {111} planes upon deformation. In samples sheared to an intermediate grade of deformation (14 000%), twin structures were observed. No significant grain refinement, disordering, nanocrystallization or amorphization was observed at any grade of deformation. This fundamentally different behaviour compared to other L1$_2$-structured compounds can arise by a lack of disordering which may impede nanocrystallization and amorphization.

Chapter 4

HPT of different L1$_2$ compounds[1]

4.1 Overview

Severe plastic deformation (SPD) can be used to make bulk, nanostructured materials. Three L1$_2$ long-range ordered (LRO) intermetallic compounds were studied by TEM methods. The superlattice glide dislocations can dissociate according to two schemes: anti-phase boundary (APB) coupled unit dislocations or superlattice intrinsic stacking fault (SISF) coupled super Shockley partials; both of them are analysed by weak-beam TEM methods. The nanostructures resulting from SPD carried out by high pressure torsion (HPT) are strongly affected by the different dissociation schemes of the dislocations. APB-dissociated superlattice dislocations and especially the APB tubes they form lead to the destruction of the LRO by HPT deformation as observed in Cu$_3$Au and Ni$_3$Al whereas in Zr$_3$Al heavily deformed ($\sim 100\ 000\%$ shear strain) at low temperatures the order is not destroyed since the deformation occurs by SISF-dissociated dislocations. In addition to the effects on the LRO the different dissociation schemes of the dislocations have a strong impact on the refinement and destruction of the crystalline structure by SPD. They seem to be decisive for the dynamic recovery considered as the limiting factor for the final grain sizes and the possibility to reach amorphization. Finally, the correlation between the reduction of the LRO

---

[1]This chapter is based on publication [S2]. The experimental results of Zr$_3$Al were obtained by the author of this thesis, the other materials were investigated by co-authors of the publication.

and the structural refinement occurring during SPD is different in the three different alloys: In Cu$_3$Au the LRO is already strongly reduced before the structural refinement reaches saturation, in Ni$_3$Al both are occurring simultaneously whereas in Zr$_3$Al the formation of the nanograins does not seem to be connected with disordering.

4.2   Introduction

Severe plastic deformation (SPD) is a novel tool to produce bulk nanostructured materials, i.e. materials with a typical grain size less than 100 nm [6]. By this top-down approach, bulk materials are deformed. The process of deformation introduces numerous lattice defects, which can lead to grain refinement down to grain sizes in the range of nanometers or in the case of alloys, even to amorphization [108, 55, 109]. The current interest in bulk nanocrystalline (NC) materials arises because they offer improved mechanical and other physical properties [4]. In this context long range ordered (LRO) intermetallics are of special interest because they are usually rather brittle due to their partly covalent bonding. SPD of intermetallic alloys can lead to a reduction of LRO and it has been shown that SPD-deformed Ni$_3$Al exhibits even superplastic behaviour [110]. In the present study, the method of high pressure torsion (HPT) is used to carry out SPD that produces bulk, non-porous specimens with a pure shear deformation up to 100 000% [7]. This large amount of shear strain requires the activation of a huge number of dislocations. In this work, we focus on L1$_2$ LRO intermetallic compounds. In this case, the deformation occurs by the movement of superlattice dislocations on {111} planes having a Burgers vector: $\mathbf{b} = a \langle 110 \rangle$ (a: lattice constant). The glide dislocations can reduce their energy by dissociation. In the L1$_2$ structure, there are two dissociation schemes for a $a[\overline{1}01](111)$ glide dislocation:

$$a[\overline{1}01] \rightarrow \frac{a}{2}[\overline{1}01] + APB + \frac{a}{2}[\overline{1}01] \tag{4.1}$$

$$a[\overline{1}01] \rightarrow \frac{a}{3}[\overline{2}11] + SISF + \frac{a}{3}[\overline{1}\overline{1}2]. \tag{4.2}$$

Eq. 4.1 shows the dissociation into unit dislocations bounding an antiphase boundary (APB) fault. The unit dislocations have the same Burgers vector

as the glide dislocations in the fcc structure and they undergo a further dissociation into Shockley partials bounding a complex stacking fault in the L1$_2$ structure [111]. Eq. 4.2 shows the dissociation into super Shockley partial dislocations bounding a superlattice intrinsic stacking fault (SISF). An important difference is that in case of Eq. 4.1 the chemical order is locally destroyed by the APB fault whereas in case of Eq. 4.2 the order is not affected by the SISF. Both dissociation schemes are observed to occur in L1$_2$ intermetallics [112]. Therefore, we selected for the present study three different L1$_2$ intermetallics: (i) Cu$_3$Au where the glide dislocations dissociate according to Eq. 4.1, (ii) Ni$_3$Al where both dissociation schemes are encountered although that of Eq. 4.1 is prevailing and (iii) Zr$_3$Al where the dissociation according to Eq. 4.2 is dominating at room temperature (RT) deformation.

4.3 Experimental Procedure

4.3.1 Ni$_3$Al

The Ni$_3$Al samples were grown as L1$_2$ LRO single-crystals using a modified Bridgman technique. They were homogenized at 1473 K for 120 h to reduce the grown-in dendritic structure. Samples oriented for single slip (compression axis [$\bar{1}$23]) were deformed in compression with a shear strain of 22% and cut parallel to the primary glide plane (111) to make TEM foils.

4.3.2 Cu$_3$Au

To get L1$_2$ ordered Cu$_3$Au samples, a special heat treatment was carried out since Cu$_3$Au has an order-disorder transition at 663 K. Samples with a grain size of about 200 μm were annealed at 623 K for 140 h and subsequently cooled by 10 K per day down to 433 K. After this treatment, the order parameter is close to 1 and the size of the grown-in domains is $\sim$ 500 nm. For the HPT deformation, disks with a diameter of 8 mm and a thickness of 0.8 mm were made by spark cutting. The HPT deformation was conducted at a quasi-hydrostatic pressure of 4 GPa at RT.

4.3.3 Zr$_3$Al

The Zr$_3$Al samples were annealed at 1160 K for 24 h to facilitate the phase transformation α-Zr + Zr$_2$Al $\rightarrow$ Zr$_3$Al since the L1$_2$ phase of Zr$_3$Al is stable only for temperatures lower than 1261 K, whereas the melting point is at 1623 K. The resulting material consisted of 80-90 % L1$_2$ ordered polycrystalline Zr$_3$Al containing residual Zr$_2$Al and α-Zr. The HPT experiments were carried out analogous to the Cu$_3$Au ones. In addition, HPT experiments at liquid nitrogen temperature (LNT) were also conducted with the other parameters staying the same.

4.3.4 TEM

Out of the HPT disks of Cu$_3$Au and Zr$_3$Al, TEM disks were cut and thin foils were prepared by electropolishing using the polishing parameters described in [113] for Cu$_3$Au and 5% perchloric acid and 95% ethanol at 246 K and 11 V for Zr$_3$Al. For the Ni$_3$Al samples, 11% perchloric acid, 5% glycerin, 30% 2-butoxyethanol and 54% ethanol at 263 K and 22.5 V were used for electropolishing. The TEM studies were carried out at acceleration voltages 150 kV and 200 kV. Diffraction contrast images (bright-field (BF), dark-field (DF), weak-beam dark-field (WBDF)) were taken as well as diffraction patterns (DP) at regions of different degrees of deformation. Diffraction patterns of the Zr$_3$Al samples were recorded on a CCD and subsequently analysed using the PASAD software to get information about the state of order of the material deformed at different temperatures [98].

4.4 Results

4.4.1 Glide dislocations and antiphase boundary tubes in Ni$_3$Al

In Ni$_3$Al, mainly glide dislocations according to Eq. 4.1 are activated at room temperature; still in a few cases a transition from the dissociation scheme of Eq. 4.1 to that of Eq. 4.2 is observed. Such a transition is shown in Fig. 4.1 (WBDF images taken under different diffraction conditions). In Fig. 4.1(a) ($\mathbf{g} = [\bar{2}02]$, BD $\sim$ [111]) both unit dislocations and both superlattice Shockley dislocations are imaged near (1) and (2), respectively. The super Shockleys have a tendency to align along $\langle 110 \rangle$ directions (as

it is seen near (2)) since in this orientation they can undergo a further dissociation leading to the formation of a locked dislocation (Giamei lock) [114]. In Fig. 4.1(b) ($\mathbf{g} = [02\overline{2}]$) only one of the super Shockleys (the upper one) is in contrast since $\mathbf{g} \cdot \mathbf{b} \equiv [02\overline{2}] \cdot \frac{a}{3}[\overline{2}11] = 0$ for the lower one. In Fig. 4.1(c) the segment of the dislocation containing the APB fault (near (1)) is out of contrast whereas the SISF of the adjacent dislocation segment (near (2)) is in contrast. Although glide dislocations dissociate according to Eq. 4.1 at RT deformation, SISF are encountered in connection with dipoles since dipoles pulled out from normal glide dislocations with APB faults frequently convert into dipoles containing SISF [114]. The lines of weak contrast along $\mathbf{b}$ visible in Fig. 4.1(b) and 4.1(c) are out of contrast in Fig. 4.1(a); they are identified as APB tubes built up by four intersecting APB faults. In a hard sphere model of the L1$_2$ structure the APB fault is a pure chemical fault and therefore an APB tube does not contain stair-rod dislocations at the intersection lines of the faults. 78 APB tubes show up in superlattice reflections [115]; they should not be visible in fundamental reflections as it is the case in Fig. 4.1(b) and 4.1(c). In this context, it has to be mentioned that recent studies showed that in Ni$_3$Al the APB faults contain in addition to the chemical fault a tiny structural component giving rise to their image contrast in fundamental reflections (as imaged in Fig. 4.1(b) and 4.1(c)). In the case of intersecting APB faults this leads to very weak stair-rod dislocations ($\mathbf{b} = \frac{a}{25} \langle 110 \rangle$ or $\mathbf{b} = \frac{a}{25} \langle 200 \rangle$) [116].

In Fig. 4.2 APB tubes are imaged in a fundamental reflection ($\mathbf{g} = [02\overline{2}]$). They show up as straight, weak lines. It is interesting to note that their density is at least locally quite high after only 22% of deformation. Several mechanisms have been put forward to explain the formation of APB tubes: they can be pulled out from non-aligned jogs of gliding APB-dissociated superlattice dislocations [118] and they can be formed during the cross-slip process of APB-dissociated superlattice dislocations, e.g. in the course of their annihilation [119, 120].

4.4.2 Antiphase boundary tubes in HPT deformed Cu$_3$Au

Fig. 4.3 shows a DF image and the corresponding DP of Cu$_3$Au deformed to shear strain $\gamma \sim 1000\%$ by HPT at RT. In Fig. 4.3(a) the APB domains are in contrast since a superlattice reflection is used as reflection vector ($\mathbf{g} = [0\overline{1}1]$). Contrary to Ni$_3Al, Cu_3$Au contains grown-in APB domains.

(a)

(b)

(c)
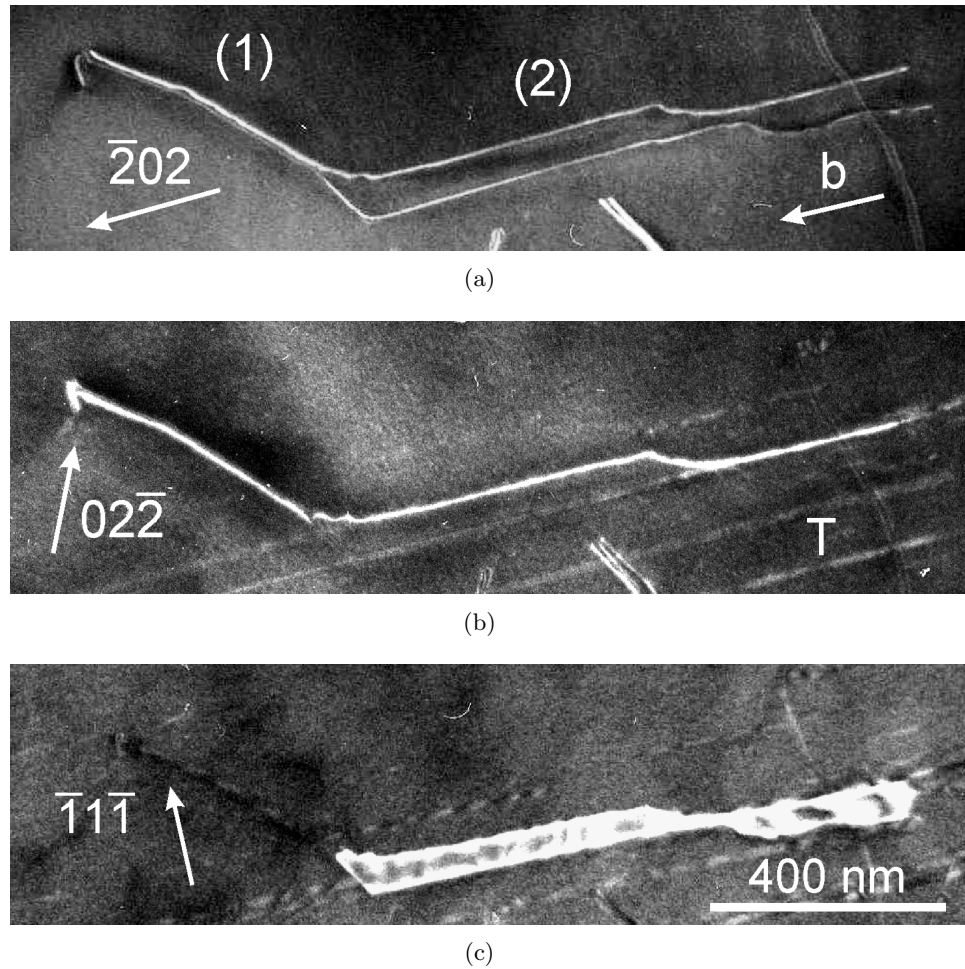
Figure 4.1: WBDF images of Ni$_3$Al deformed in compression (22% shear strain) at RT. Superlattice glide dislocation showing a transition from the dissociation scheme with the APB fault to that with the SISF (marked (1) and (2), respectively). (a) **g** ∥ **b**; all dislocations in contrast. (b) One super Shockley partial out of contrast near (2). APB tubes (e.g. near (T)) in contrast. (c) Superlattice dislocation (1) out of contrast, SISF and APB tubes in contrast [117].
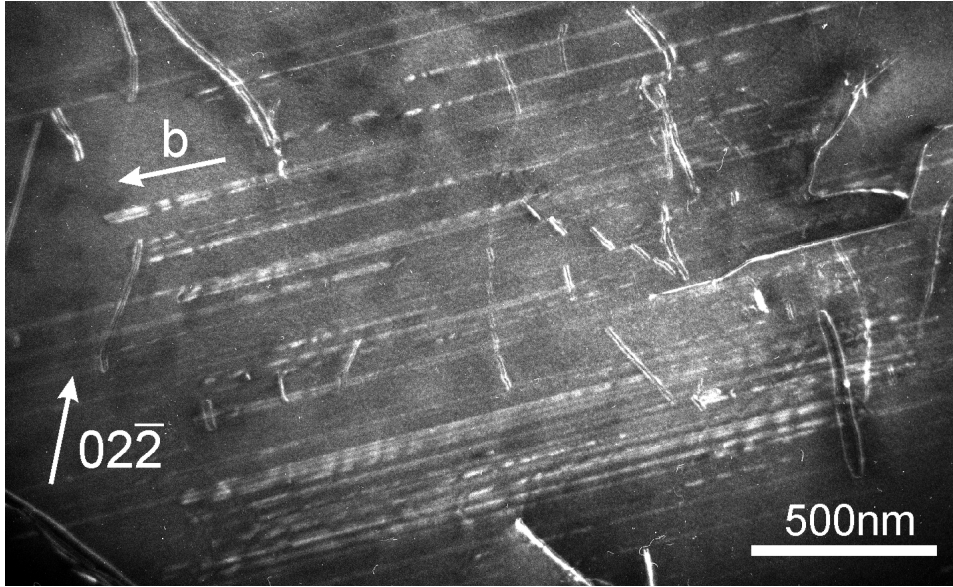
Figure 4.2: WBDF image of Ni$_3$Al deformed in compression (22% shear strain) at RT. A high density of APB tubes aligned along **b** and several edge dipoles of superlattice dislocations containing APB faults [117].

After deformation their density is increased as they are cut by glide dislocations. In addition to them, APB faults aligned along the traces of the $(1\bar{1}1)$ planes (which are parallel to the projection of $\mathbf{b} = \pm a[10\bar{1}]$) are visible in Fig. 4.3(a). They are identified as APB tubes by analysing the DP (cf. Fig. 4.3(b)). The DP contains the fundamental and superlattice spots corresponding to the beam direction BD $\sim$ [011]. (The fundamental spots are split since Au is redeposited epitactically on the surface during electropolishing.) In addition to the spots, streaks are observed going through superlattice spots only [106]. It is concluded that they are caused by disks in reciprocal space since their extension and intensity is relatively large near superlattice reflections (e.g. $\pm$[100]) that are rather weak under the given reflection condition ($\mathbf{g} = [0\bar{1}1]$). Therefore it can be followed that a high density of APB tubes is present after HPT deformation leading to a gradual reduction of the LRO.
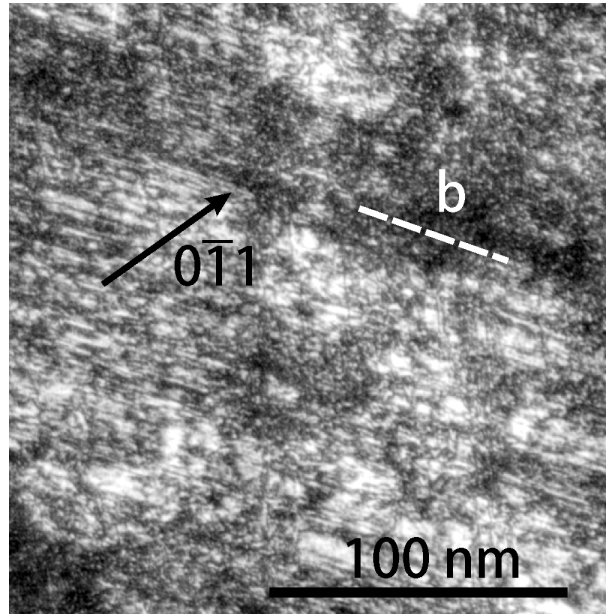
(a)
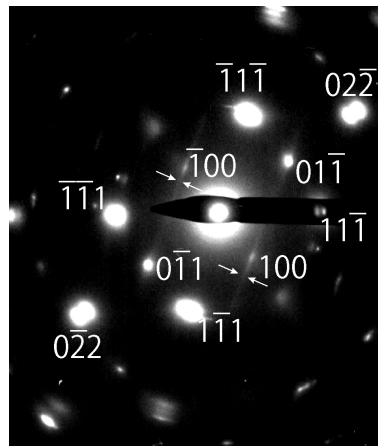
(b)

Figure 4.3: Cu$_3$Au deformed by HPT at RT (shear $\sim$1000%). (a) DF image taken with a superlattice reflection showing a high density of the grown-in APB domains cut by the glide dislocations and APB faults extended along **b** (dashed line, does not lie in image plane) identified as APB tubes by the DP. (b) DP showing fundamental and superlattice reflections. The APB tubes are causing the streaks going through the superlattice reflections only.

4.4.3 SISF and amorphization in Zr_3Al

Figure 4.4(a) shows a DF image (BD $\sim$ [011]) and the corresponding DP of a region with a high density of SISF in Zr_3Al. Due to the inhomogeneous deformation in the sample, the value of the local shear strain can only be estimated to be less than 10 000% in the imaged region. The DF image was taken by placing the objective aperture on the streak connecting the fundamental reflection spots (cf. dashed circle in Fig. 4.4(b)). The streaks are caused by SISF. They are parallel to the $\langle 111 \rangle$ directions since the SISF lie on $\{111\}$ planes. No streaks are observed near the superlattice spots indicating that APB faults are not occurring in a high density.

The influence of the deformation temperature on the structural changes by HPT deformation (of about the same amount) in Zr_3Al is shown in Fig. 4.5 and Fig. 4.6. In Fig. 4.5 the results of a sample deformed at LNT are illustrated. A band of amorphous material (labelled A) surrounded by NC regions is observed. The analysis of the DP by PASAD [98] of Fig. 4.5 reveals unambiguously that the chemical order is still present in the NC regions (grain size 10 to 20 nm) surrounding the amorphous band. Fig. 4.6 shows the results of a sample deformed at RT. The structure is NC (grain size again 10 to 20 nm), amorphous regions have not been encountered. The DP reveals that the amount of the order retained after the RT deformation is much less compared to that after LNT deformation although the amount of deformation and the grain sizes are similar in both cases.

4.5 Discussion

4.5.1 Destruction of LRO by SPD

From the experimental results shown in Chapter 4.4 it is concluded that the destruction of the LRO occurring during SPD is facilitated by glide dislocations containing APB faults (cf. Eq. 4.1).

In $L1_2$ LRO Cu_3Au the glide dislocations correspond to the scheme of Eq. 4.1 at RT deformation. SISF have not been observed. The destruction of the LRO by deformation is very effective since it occurs by both the cutting of the grown-in domains and the formation of a high density of APB tubes (cf. 4.4.2); the destruction seems to saturate at 5000% of deformation [105]. It should be pointed out that on a local (atomic) scale the structure
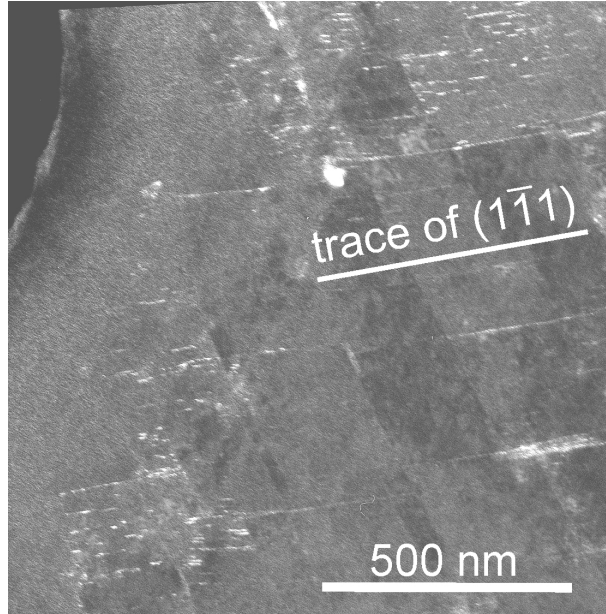
(a)
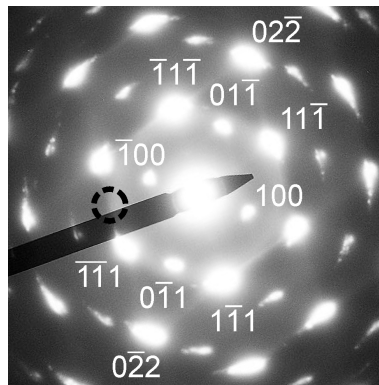
(b)

Figure 4.4: Zr$_3$Al deformed by HPT at RT (shear strain < 10000%) (a) DF image of the SISF taken by placing the objective aperture on a streak between two fundamental reflections. The SISF are imaged as straight lines of bright contrast since BD ∼ [011]. (b) DP with the position of the objective aperture encircled lying on a streak caused by the SISF. Streaks going through the superlattice reflections indicating APB faults have not been encountered.
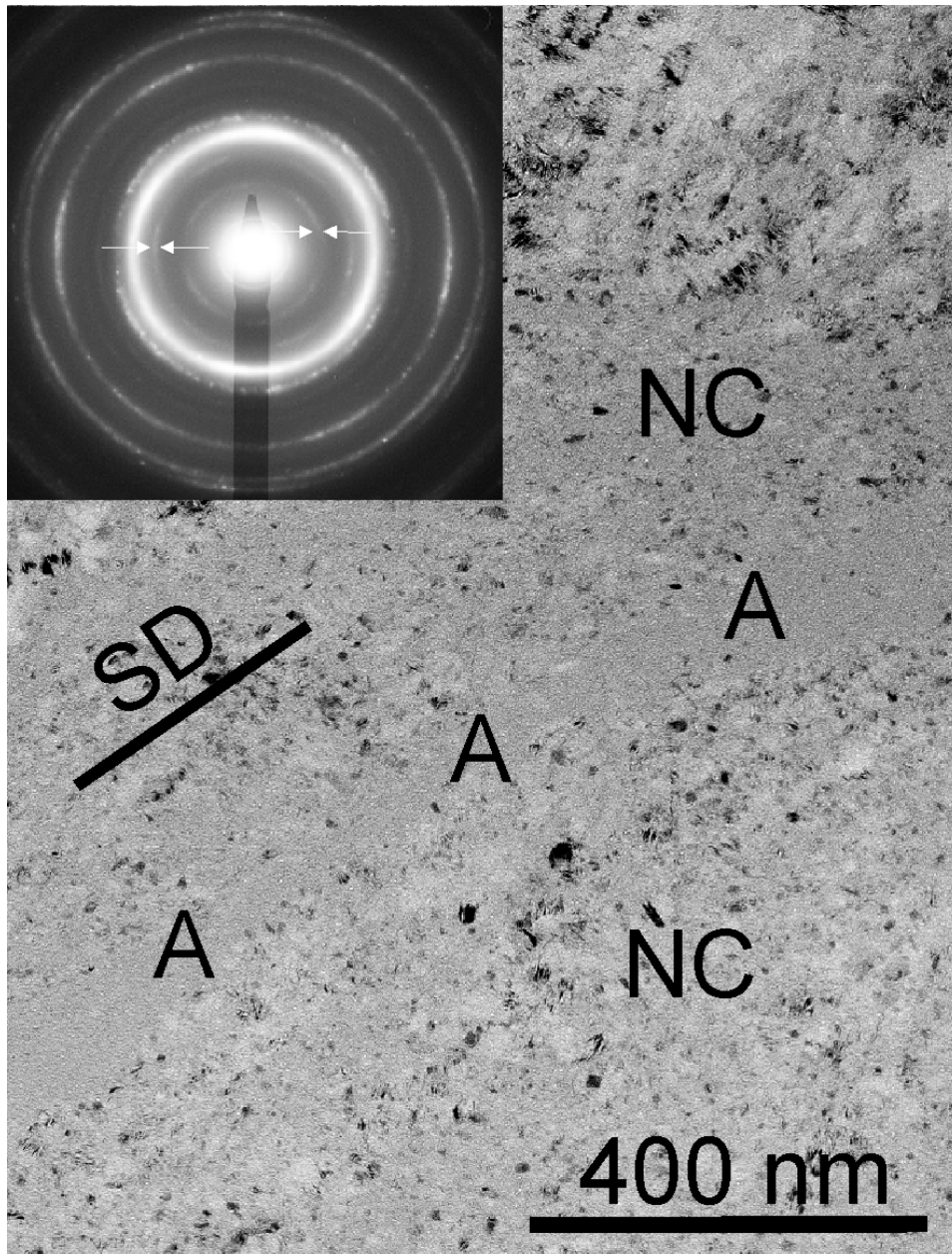
Figure 4.5: BF image and DP of Zr$_3$Al deformed by HPT at LNT to a shear strain of ~100 000%. NC phase (grain size 10 to 20 nm with an embedded amorphous band A~50 nm wide) lying about parallel to the shear direction (SD). The inserted diffraction pattern shows rings of superlattice reflections (marked by arrows) indicating that NC region is not disordered.
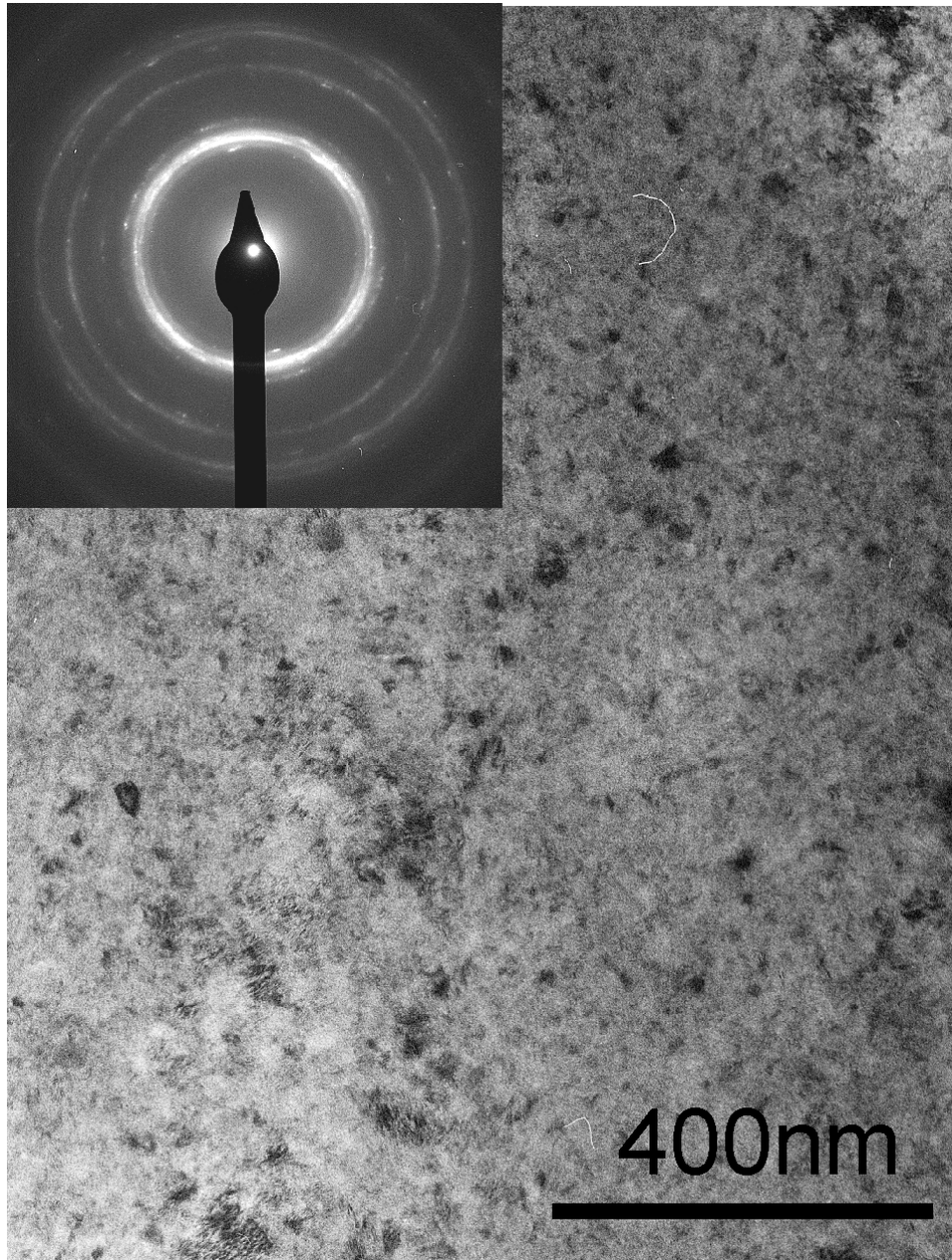
Figure 4.6: BF image and DP of Zr$_3$Al deformed by HPT at RT to a shear strain of $\sim$100 000%. The size of the nanocrystals is similar to that in Fig. 4.5, the difference is that the DP of the NC region shows only weak rings of superlattice reflections. Amorphous regions have not been encountered.

will be rather inhomogeneous after the destruction of the LRO by SPD and therefore locally not equivalent to a disordered or short-range ordered (SRO) structure made by thermal treatment.

In Ni_3Al deformed at RT the vast majority of the glide dislocations contains APB faults; cases where a transition to a SISF-dissociated glide dislocation (as shown in Fig. 4.1) is observed are very rare. SISF are found to occur in Giamei locked dipoles aligned along $\langle 110 \rangle$ directions. (It should be mentioned that in samples deformed at LNT a clear increase of the density of the SISF is occurring.) In Ni_3Al the dislocation structure observed after RT deformation contains mainly edge dislocations and only a few screws indicating that they cross-slip and annihilate thus giving rise to the formation of APB tubes [121] (This agrees with the fact that RT is below the temperature regime with an anomalous increase of the yield strength caused by screws converting to Kear-Wilsdorf locks [122]).

The destruction of the LRO starts locally in the regions of high deformation (e.g. at geometrical boundaries and slip bands); extensive disordering leading to the global loss of LRO seems to be directly associated with the process of dynamic recovery followed by nanocrystallization [104]. In the nanocrystalline state, only a very small amount of residual order could be detected by high-resolution TEM [123]. It is proposed that for the process of disordering the APB tubes are more important than the stored superlattice dislocations containing APB faults. The density of APB tubes can be much higher than that of the dislocations since the long-range stress field of the tubes is very small compared to that of the dislocations (up to a factor 15). It is interesting to point out that the Ni_3Al samples with LRO destructed by SPD could be used to make in a bulk material tailored metastable APB domains of nanodimension that cannot be achieved by quenching.

In Zr_3Al the dislocation scheme of the glide dislocations is strongly dependent on the deformation temperature: Above 873 K APB-dissociated glide dislocations are prevailing; at temperatures below 673 K SISF-dissociated dislocations get more and more dominant the lower the temperature is [86, 88]. This agrees with the experimental findings of 4.4.3, yielding that the destruction of the LRO is more pronounced after the RT deformation than after LNT deformation. When the grain size is small, as in HPT-deformed Zr_3Al (10 to 20 nm), a reduction of the LRO arises together with a destruction of the structure by the atoms at the grain boundaries. This

effect is even more pronounced in HPT deformed alloys since after HPT deformation, the grain boundaries are highly irregular.

4.5.2   Refinement and destruction of the crystalline structure by SPD

The SPD of metals and alloys leads to a reduction of the grain size by a process that is mediated by dislocations down to grain sizes of about 20 nm. At smaller grain sizes other deformation mechanisms (e.g. grain boundary mediated processes) are getting more and more important until at least in some alloys an amorphous structure is reached by destruction of the crystalline one.

In different L1$_2$ intermetallics different dissociation schemes of the glide dislocations are occurring. Superlattice glide dislocations bounding APB faults (cf. Eq. 4.1) are activated in Cu$_3$Au and Ni$_3$Al during RT deformation. At high densities caused by large strains they are leading to the reduction of the LRO (as discussed in 4.5.1). This has the important impact that after destruction of the LRO for a further deformation superlattice dislocations ($a \langle 110 \rangle$) are not necessary any more since the deformation can be carried by unit dislocations ($\frac{a}{2} \langle 110 \rangle$) like in fcc alloys. It seems safe to assume that dynamic recovery is the limiting factor for the deformation energy that can be stored by the dislocations during SPD. In Cu$_3$Au disordering takes place already in the coarse-grained material (cf. 4.4.2). Once the material is disordered, dynamic recovery (e.g. by cross-slip annihilation of screws) is easier than in the LRO structure.

This is used to explain the experimental result that in saturation, the grain size achieved by HPT deformation of Cu$_3$Au (100 to 500 nm) [105] is larger than that of Ni$_3$Al (4-200 nm) [124]. In Ni$_3$Al the structure stays ordered accumulating strain energy during the HPT deformation until it changes in a single step into a disordered NC structure. In Zr$_3$Al the dissociation of the superlattice dislocations with SISF is prevailing at RT deformation and completely dominating at LNT deformation. In this case dynamic recovery of the dislocations formed during HPT deformation is hindered since the widely dissociated super Shockley partials (cf. Fig. 4.1) will only partially annihilate leaving stair-rod dislocations ($\frac{a}{3} \langle 110 \rangle$) at the intersection line of the SISF behind. Therefore, a higher density of stored dislocations can be accumulated compared to the case of annihilating APB-

coupled dislocations. This could explain that in Zr_3Al the grain size yielded in saturation by HPT at RT is small and that by deformation at LNT even amorphization can be achieved.

4.6 Conclusions

(i) From TEM studies it is concluded that APB-dissociated superlattice dislocations and especially the APB tubes they form lead to the destruction of the LRO by the HPT deformation as observed in Cu_3Au and Ni_3Al.

(ii) From the result of Zr_3Al heavily deformed at LNT ($\sim$100 000% shear strain) by HPT it is concluded that deformation by SISF-dissociated superlattice dislocations does not destroy the LRO.

(iii) It is concluded that in $L1_2$ intermetallics the two dissociation schemes of superlattice glide dislocations also have a strong impact on the refinement and destruction of the crystalline structure by SPD. The intrinsic properties of the glide dislocations (e.g. the ability of screws to cross-slip and annihilate) seem to be decisive for the dynamic recovery considered as the limiting factor for the final grain sizes and the possibility to reach amorphization.

(iv) From the results of Zr_3Al deformed at LNT it is concluded that the formation of nanograins is not necessarily connected with disordering.

Chapter 5

Effect of Repeated Cold Rolling on Zr$_3$Al[1]

5.1 Overview

The intermetallic compound Zr$_3$Al is severely deformed by the method of repeated cold rolling. By X-ray diffraction it is shown that this leads to amorphization. TEM investigations reveal that a homogeneously distributed debris of very small nanocrystals is present in the amorphous matrix that is not resolved by X-ray diffraction. After heating to 773 K, the crystallization of the amorphous structure leads to a fully nanocrystalline structure of small grains (10 - 20 nm in diameter) of the non-equilibrium Zr$_2$Al phase. It is concluded that the debris retained in the amorphous phase acts as nuclei. After heating to 973 K the grains grow to about 100 nm in diameter and the compound Zr$_3$Al starts to form, that is corresponding to the alloy composition.

5.2 Introduction

The intermetallic compound Zr$_3$Al has been of special interest as a nuclear structural material although a drawback of the material is embrittlement under certain irradiation conditions [66]. Recently, it was shown that nanostructuring of materials can enhance the irradiation resistance, e.g. for the intermetallic compound NiTi [27]. One successful method to achieve nanos-

---

[1]This chapter is based on publication [S3].

tructuring in bulk materials is severe plastic deformation (SPD). The formation of the nanocrystalline structure can occur directly by grain refinement of the coarse grained material or by crystallization of SPD induced amorphous material. For example, crystallization of the intermetallic alloy NiTi amorphized by severe plastic deformation can lead to nanocrystalline structures and by modification of the deformation path and the heat treatment, properties of the alloy can be tailored [125].

Bulk intermetallic alloys can be deformed severely using high pressure torsion (HPT). For Zr_3Al, it was shown that HPT at room temperature leads to a final grain size of approximately 20 nm, but amorphization of a significant volume fraction of the sample has not been encountered [S2]. Furthermore, it was observed that upon HPT deformation, Zr_3Al exhibits inhomogeneous microstructures, as were also observed in the case of $L1_2$ structured Ni_3Al [104, 126, 127].

Deformation by cold rolling with intermediate foldings (repeated cold rolling - RCR) is an alternative promising deformation route to produce bulk nanocrystalline materials [128]. The minimum final grain sizes that can be achieved for a material are often smaller than the corresponding ones after SPD under high pressure (e.g. HPT, equal-channel angular pressing) [56]. In addition, RCR can lead to amorphization.

It is the aim of this work to study the effect of RCR on the grain refinement of Zr_3Al and the behaviour of the refined material upon heating to different temperatures. Crystallization of the amorphous phase is also of interest since the Zr-Al system exhibits several intermetallic phases (cf. Fig. 5.1) and the driving force to form the $L1_2$ structure was reported to be rather weak compared to the one of neighbouring phases [129].

5.3   Experimental Procedure

Zr_3Al was alloyed with an initial composition of Zr with 27 at.% Al. The alloy was homogenized at 1160 K for 24 h leading to the ordered $L1_2$ structure with 10% residual Zr_2Al and α-Zr. The material was cut to sheets 10mm x 10mm x 0.8mm in size. The thickness of the sheets was reduced to 0.25 mm by repeated cold rolling. Then they were folded and again cold rolled until a thickness of 0.25 mm was achieved. This process was repeated up to 80 times. During rolling the alloy was placed between two spring steel plates.
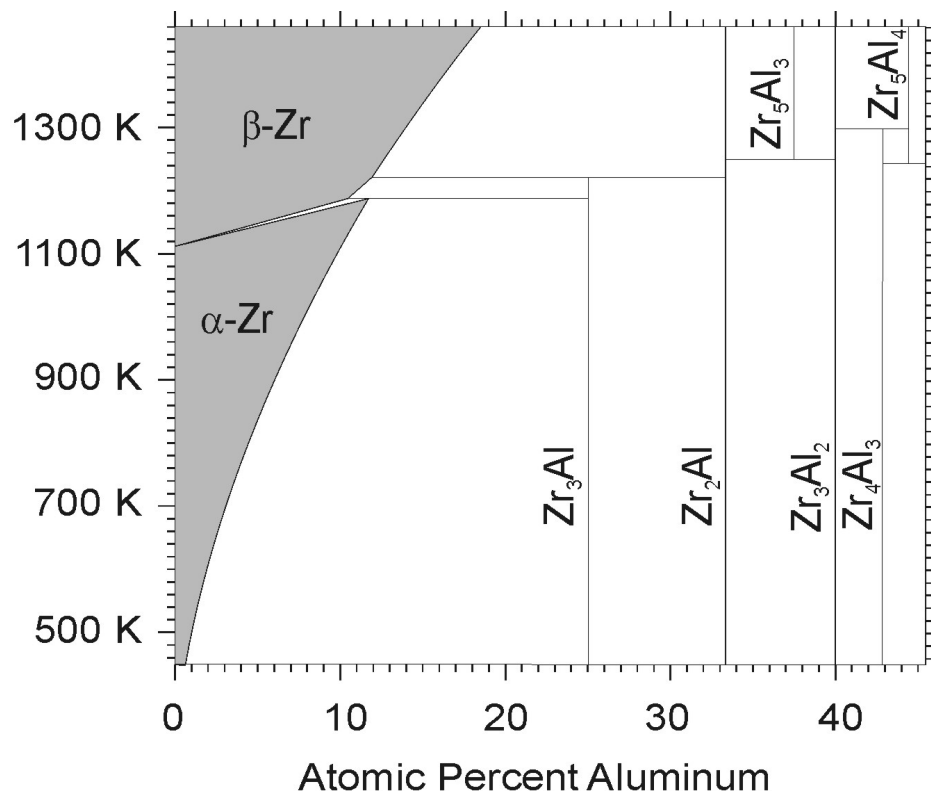
Figure 5.1: The Zr-rich side of the phase diagram of the Zr-Al system. Grey areas are existence regions. The intermetallic phases are all line compounds. The L1$_2$-phase at 25at% Al is stable up to 1261 K, at higher temperatures it decomposes to bcc β-Zr and Zr$_2$Al, which is of the B8$_2$-structure [61].

The deformed material with the highest strain (80 foldings, $\epsilon_{80} = 6600\%$) was heated to different temperatures at different heating rates in a differential scanning calorimeter (DSC). For the baseline subtraction, the material was kept at the maximum temperature after heating until the exothermic signal was negligible to avoid exothermic processes in the subsequent run that provided the baseline.

Undeformed samples, samples deformed for 80 foldings and samples heated to 773 K and 973 K at 20 K min^{-1} after deformation for 80 foldings were investigated by X-ray diffraction (XRD) and transmission electron microscopy (TEM). The XRD data were analysed to get information about the coherently scattering domain (CSD) size and the crystal structure of the samples.

The TEM preparation was done by cutting disks suitable for TEM preparation from samples of different states, subsequent grinding and dimpling and finally electropolishing using the same parameters as described in [S1]. Acceleration voltages of 200 kV and 300 kV were used for conventional TEM and high-resolution TEM, respectively.

5.4   Experimental Results

TEM analysis of samples deformed for 5, 10 and 20 foldings reveals that already at these relatively low strains ($\epsilon_5 = 530\%$, $\epsilon_{10} = 930\%$, $\epsilon_{20} = 1730\%$), grain refinement is clearly visible. At 80 foldings ($\epsilon_{80} = 6600\%$), XRD shows two broad peaks (cf. Fig. 5.2) indicating an amorphous sample. Complementary TEM images taken of the same material yield additional important information (cf. Fig. 5.3): a mostly homogeneous intensity distribution with a few remaining crystalline regions that are 100 to 200 nm in diameter (Fig. 5.4a). From dark-field images, it can be seen that the whole crystalline region is oriented in a similar way, so it is rather one crystallite than an agglomeration of many small crystallites. The complex contrast is an indication for a very high defect density in the crystallite. In addition, small crystallites were identified using high-resolution TEM in the amorphous matrix (Fig. 5.4b); they show up as dark dots in Fig. 5.3 (The large (< 500 nm) roundish bright areas originate from thickness variations in the TEM foil developed as an artifact during electropolishing.). Combining the XRD and TEM results, a small crystalline volume fraction of a few percent in a
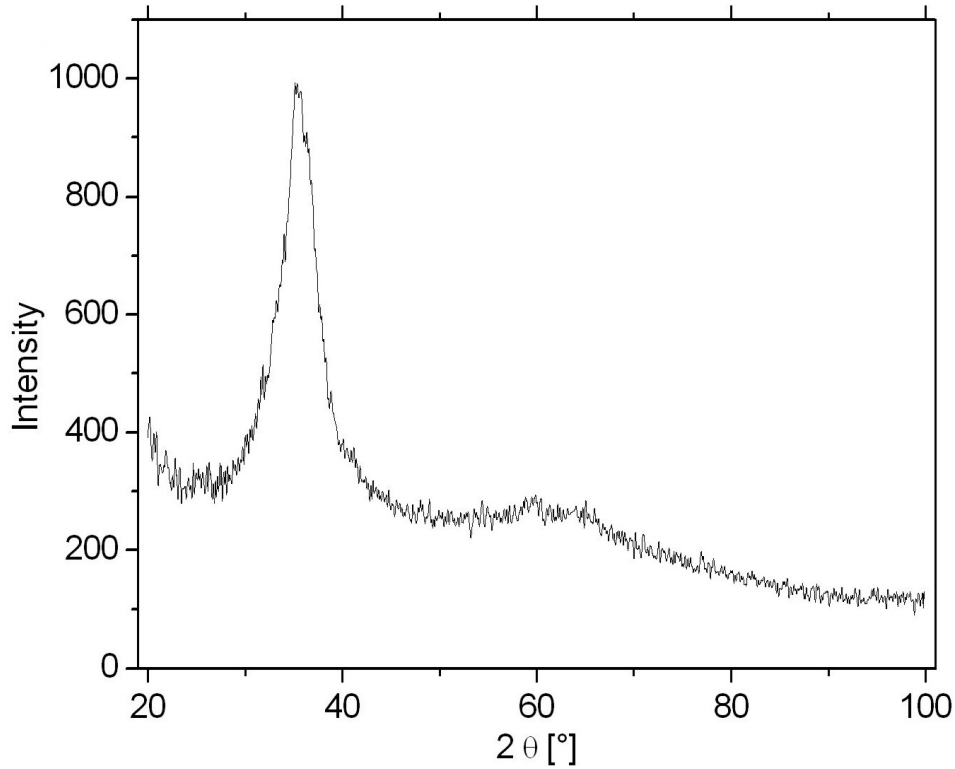
Figure 5.2: XRD analysis of the amorphous sample produced by repeated cold rolling with 80 intermediate foldings. The spectrum shows two broad peaks indicating a mostly amorphous sample.

mostly amorphous sample was identified as the sample structure after 80 foldings.

DSC experiments were conducted to clarify the thermal stability of the as-deformed material. Fig. 5.5 shows a baseline-subtracted DSC curve for a heating rate of 5 K min^{-1}. The baseline was obtained by a second run after annealing at 973 K for 30 min. Two exothermic peaks are revealed. The first peak (peak A) that starts at 650 K and has its maximum at 720 K is caused by crystallization of the amorphous phase. To determine the enthalpy of peak A, the following method (cf. inset in Fig. 5.5) was chosen under the assumption that the peak is symmetric and that peak B has a negligible influence on the low-temperature half of peak A: From the left integration limit $T_{start} = T_{peak} - 2(T_{peak} - T_{onset})$ (T_{onset} was determined using the tangent method), the enthalpy between a horizontal baseline and the DSC curve was integrated until T_{peak} (grey area in inset in Fig. 5.5). This value
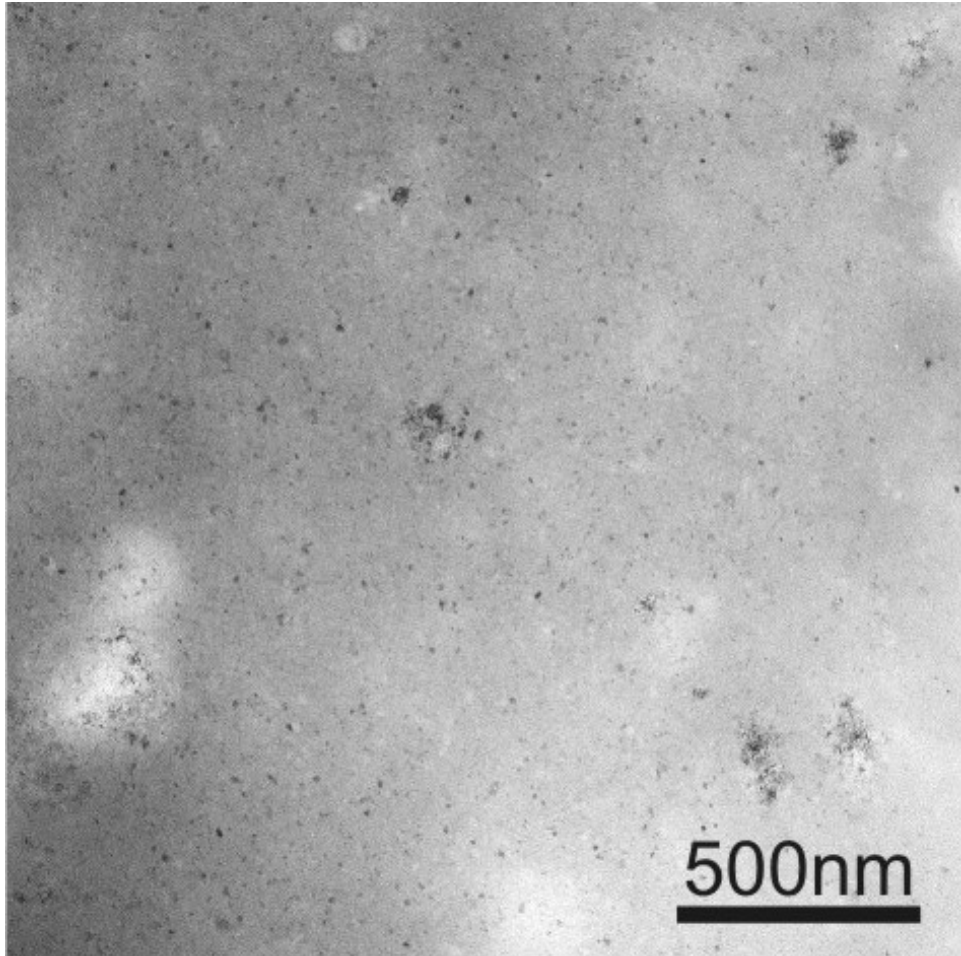
Figure 5.3: TEM bright-field image of the amorphous sample produced by cold rolling with 80 intermediate foldings showing large areas of homogeneous intensity. Some larger crystallites (100 - 200 nm) and several small crystallites (black spots, typically <10 nm) can be seen in the amorphous matrix.
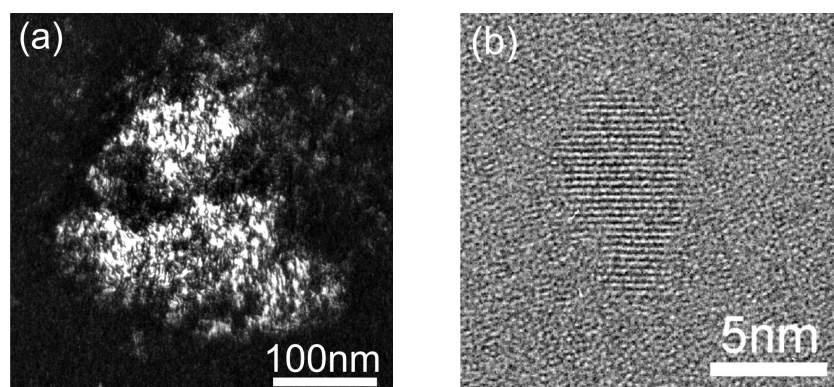
Figure 5.4: Crystallites in the amorphous matrix. (a) TEM dark-field image of one larger crystallite. The contrast shows that the crystallite contains a lot of structural defects. (b) High-resolution TEM image of a small crystallite embedded in an amorphous matrix

was taken as the enthalpy of the low-temperature half of the enthalpy of the peak. Due to the above-mentioned assumptions, doubling this value yields the total enthalpy of the peak. This method was chosen because the results of a regular peak fit differed strongly (20-80 J/g) at comparable qualities of the fit, even for a single heating rate. The determination of the enthalpies using the above-mentioned method for four different heating rates yielded a crystallization enthalpy of 41 ± 3 J/g. This statistical uncertainty, however, seems to underestimate the real one, that might be as high as 20%, due to systematic instrumental errors and the assumption of peak B not having an influence on the low-temperature half of peak A. A Kissinger plot using the four different heating rates ranging from 5 K min^{-1} to 50 K min^{-1} leads to an activation enthalpy of $Q = 2.60 \pm 0.10$ eV. The second exothermic peak with a plateau-like behaviour at high temperatures is attributed to a superposition of grain growth and phase transformation processes.

Using a heating rate of 20 K min^{-1}, samples were heated to 773 K and to 973 K, i.e. after the crystallization peak and to the maximum temperature of the DSC curve, respectively. Fig. 5.6a shows a TEM bright-field image of the sample heated to 773 K revealing nanocrystalline material with a grain size of approximately 10-20 nm. This grain size estimation is in reasonable agreement with a Williamson-Hall analysis of the CSD size as deduced from the corresponding XRD spectrum (cf. Fig. 5.6b) yielding a mean crystalline diameter of 40 nm (The grain sizes coming from TEM and
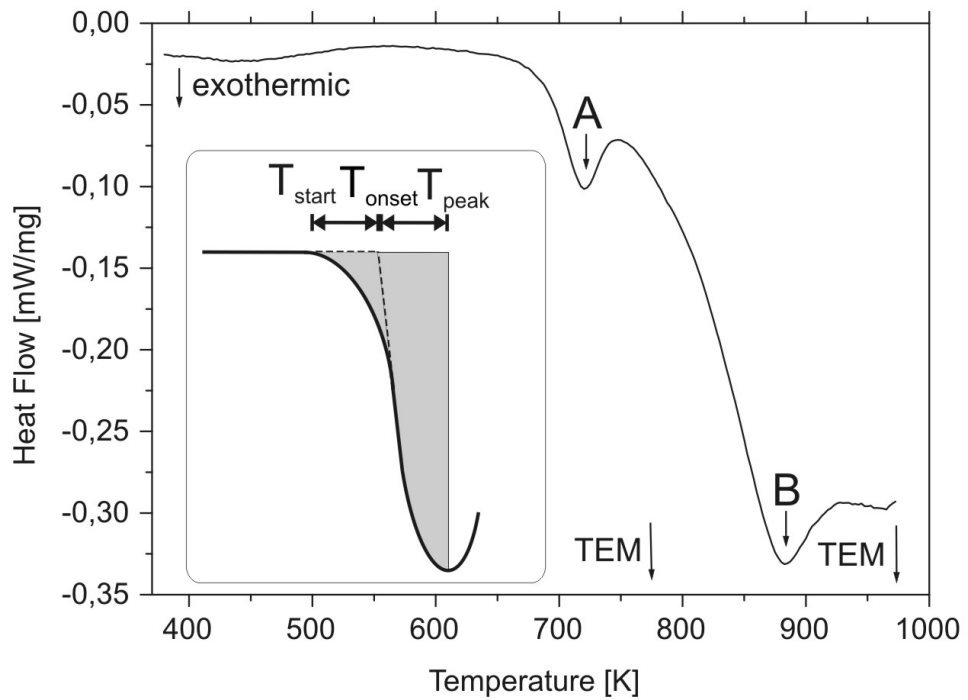
Figure 5.5: DSC curve (heating rate 5 K min^{-1}) of Zr$_3$Al deformed by 80 foldings. A crystallization peak (marked A) can be seen at 721 K. A large peak (marked B) occurs at higher temperature. The temperatures to which the TEM samples were heated are indicated. A sketch of the integration method is shown in the inset.

XRD are arithmetically and volume weighted, respectively, resulting in an intrinsic difference of the results). Apart from the CSD size, the XRD results show that the $B8_2$-structure is clearly predominant in the sample heated to 773 K. All the major peaks can be related to peaks of this structure, which is the equilibrium phase for Zr_2Al [130]. This result was also confirmed by analyzing the corresponding electron diffraction ring patterns using the PASAD software [98]. After heating the sample to 973 K, defect-free grains grow to a size of $\sim$ 100 nm as observed in the TEM bright-field image (cf. Fig. 5.7a). The corresponding XRD curve (cf. Fig. 5.6b) shows that the $L1_2$ structure (i.e. the equilibrium structure for Zr_3Al) starts to form. At this grain size, an estimation of the CSD size by XRD was not considered since the instrumental line broadening is about the same as the grain size broadening and this leads to a large uncertainty in grain size broadening after deconvolution of the peak. It should be mentioned that after heating to 973 K at 20 K min^{-1} and immediate subsequent cooling at the same rate, the $B8_2$ structure is still predominant.

5.5   Discussion

TEM analyses of samples deformed by RCR show that pronounced grain refinement takes place at much lower strain levels than it was reported for Zr_3Al deformed by high pressure torsion [S2]. After 80 foldings ($\epsilon = 6600\%$), at least 90% of the volume is amorphous and the grain structure is finer than that in the HPT experiment. This is in agreement with the results showing that the grain sizes after RCR can be smaller than those achieved by other SPD techniques [56].

As depicted in Fig. 5.3, a homogeneously distributed crystalline debris is retained in the amorphous material. Upon heating to 773 K, the crystallites that are only a few nm large can serve as pre-existing nuclei and lead to the formation of a fine nanocrystalline structure (10 - 20 nm, cf. Fig. 5.6a) because of their dense distribution. A similar behaviour was observed for NiTi, that was rendered amorphous by severe plastic deformation and afterwards heated in in-situ TEM experiments [125]. Peak A of the DSC curve (cf. Fig. 5.5) is therefore attributed to crystallization and grain growth until impingement. The peak temperature is about 70 K lower than that reported in [129] for ball-milled amorphous Zr_3Al. This difference can be
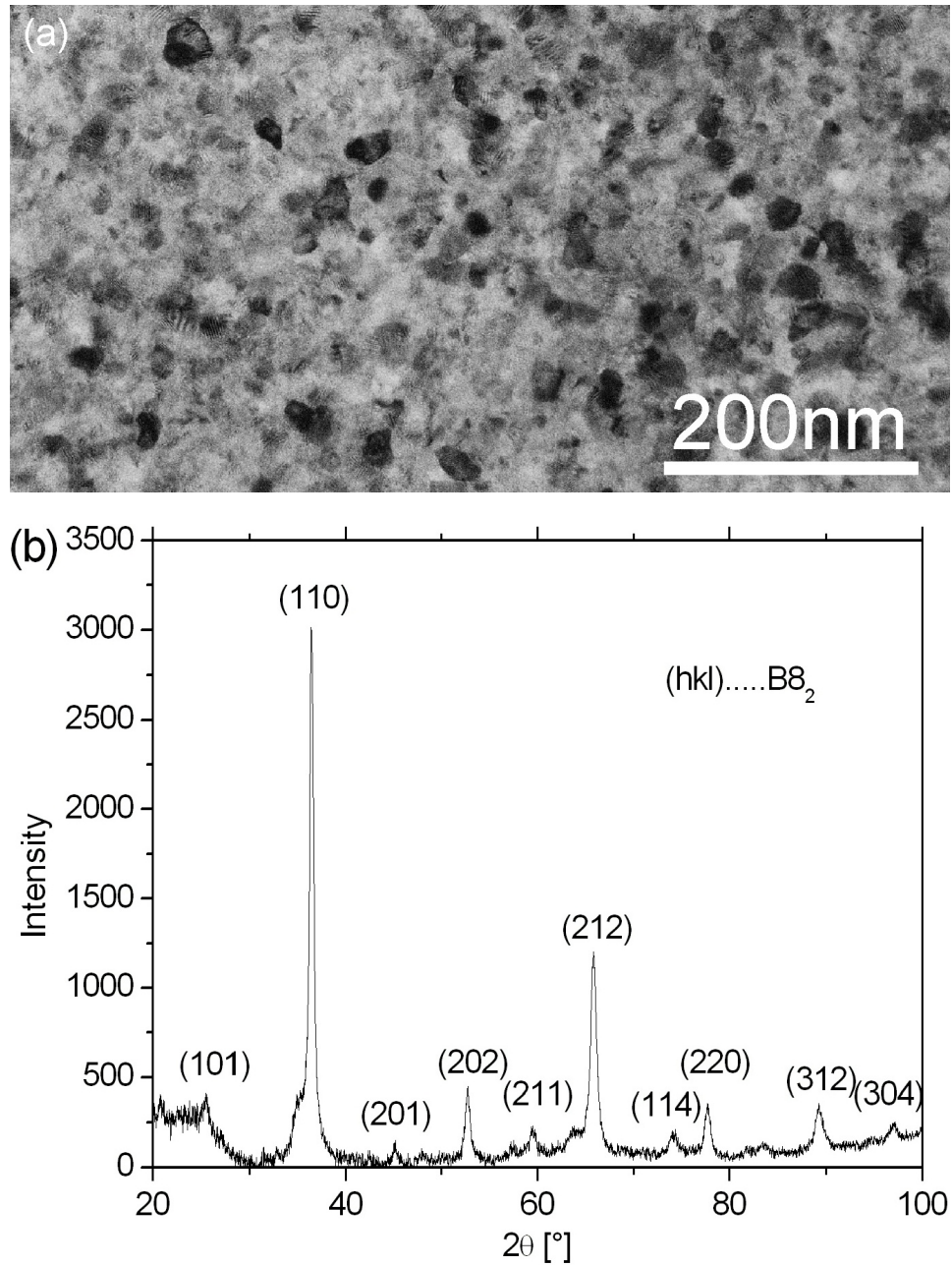
Figure 5.6: TEM and XRD of Zr_3Al deformed by 80 foldings and subsequently heated to 773 K. (a) TEM image. The grain size is 10 - 20 nm. (b) XRD spectrum. All the peaks correspond to the $B8_2$ structure. The corresponding lattice planes of the $B8_2$ structure are indicated; the pronounced background at low angles comes from the glass sample holder.
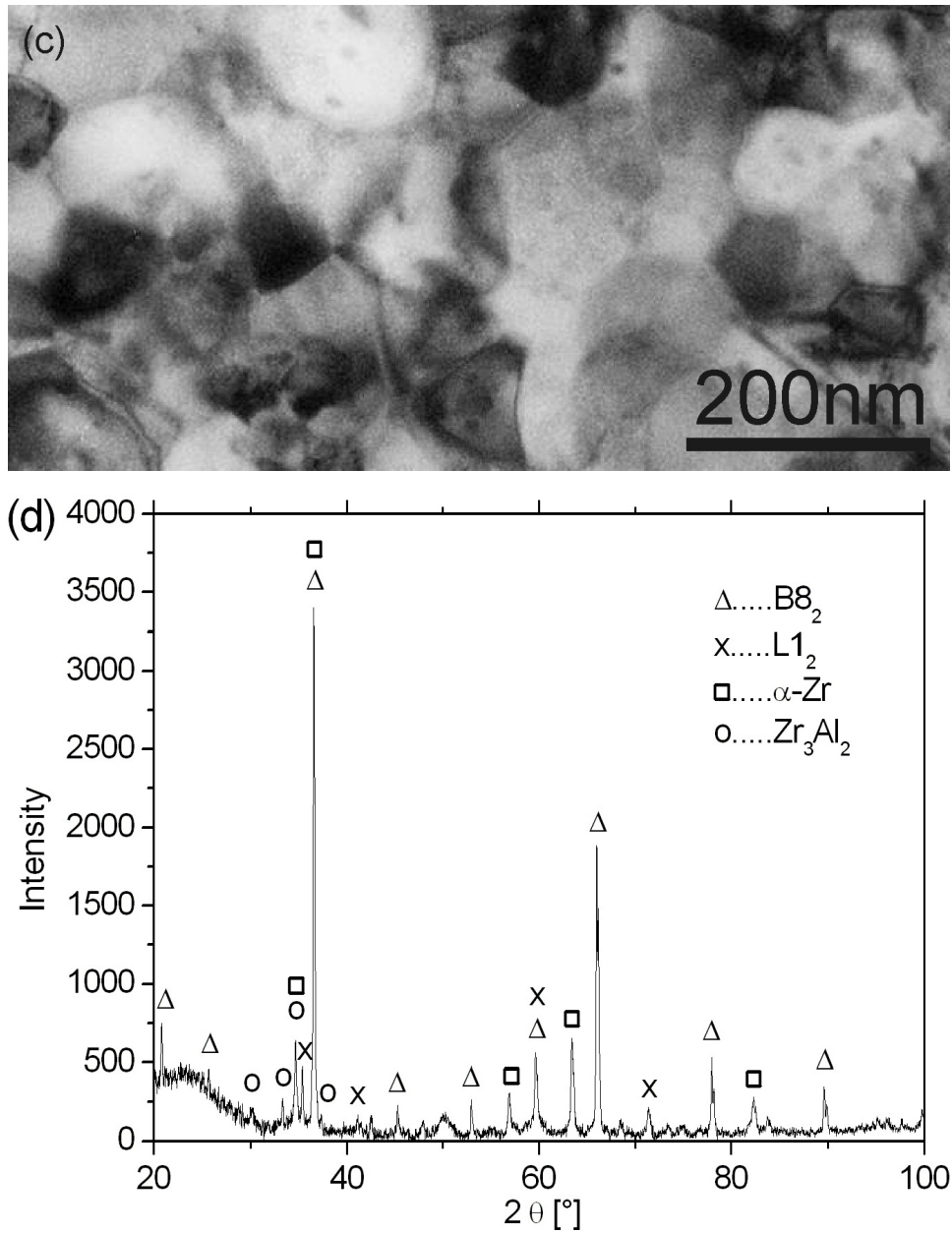
Figure 5.7: TEM and XRD of Zr_3Al deformed by 80 foldings and subsequently heated to 973 K. (a) TEM image showing defect-free grains with a grain size of $\sim$ 100 nm. (b) XRD spectrum. The major peaks mainly correspond to the $B8_2$ structure; minor peaks to the α-Zr, $L1_2$ and the equilibrium Zr_3Al_2 structure, the pronounced background at low angles comes from the glass sample holder.

explained by the presence of the crystalline debris in our samples. A similar behaviour was observed in NiTi with a peak temperature reduction of 100 K [125]. Therefore, it is concluded that the higher peak temperature reported for Zr_3Al in [129] indicates that the material did not contain a crystalline debris. Peak B of the DSC curve (cf. Fig. 5.5) is interpreted to be caused by grain growth and phase transformations between different intermetallic phases (cf. Fig. 5.7a and b).

By experimental and theoretical evaluation, Ma et al [131] deduced an enthalpy release caused by devitrification of Zr_3Al of ~ 85 J/g, which is about twice the amount that is determined here. Possible reasons for the higher crystallization enthalpy could be an additional contribution of grain growth, which is part of DSC peak B (cf. Fig. 5.5) in this work or a principal difference in the structure of the amorphous samples caused by the different processing conditions (strains, strain rates, deformation temperatures etc).

X-ray results show that the equilibrium $L1_2$ structure does not form in the initial crystallization process since only $B8_2$ structured Zr_2Al was detected after heating to 773 K (cf. Fig. 5.6b). It is well established that nanocrystalline material can have a different crystal structure than its coarse crystalline counterpart at the same composition and temperature [132, 133]. In the present case, antisites or vacancies on Al sites of the ordered $B8_2$ structure could in addition compensate for the difference between the nominal as-cast composition and that of stoichiometric Zr_2Al. From the DSC curve, the formation enthalpy of the present $B8_2$ structure (containing a high number of point defects causing excess enthalpy) is determined to lie between the one of the amorphous phase and the one of the $L1_2$ structure as given in [131]. This makes the transformation path *amorphous* $\rightarrow B8_2 \rightarrow L1_2$ thermodynamically reasonable. A comparison with data of Zr_5Al_3 and Zr_5Al_4 favors the substitution with vacancies [134]. Assuming a vacancy density that compensates for the aluminium deficiency in the formation of the $B8_2$ structure and ignoring grain size effects causing excess enthalpy gives a reasonable upper limit of 2.7 eV for the formation enthalpy of a vacancy.

After heating to 973 K, the Zr_2Al phase is still predominant, but some α-Zr, $L1_2$ structured Zr_3Al and a little Zr_3Al_2 of the space group $P4_2/mnm$ starts to form (cf. Fig. 5.7b).

The heat treatments presented in this work resulted in a very fine nanocrystalline structure dominated by the $B8_2$ phase (10 - 20 nm). It is suggested

that heat treatment of amorphous samples at low temperatures (~ 770 K) for several hours or even days might give rise to the formation of the $L1_2$ structure without causing excessive grain growth. It is concluded that the crystalline debris resulting from the amorphization by RCR is important for reducing the grain size of the crystallized material by providing a dense network of homogeneously distributed pre-existing nuclei.

5.6 Conclusions

- Zr_3Al can be rendered amorphous by repeated cold rolling as concluded from the X-ray results. The TEM studies show that the deformed material contains a crystalline debris that is not resolved by X-ray diffraction.

- Heating to 773 K leads to the crystallization of small (10 - 20 nm in diameter) $B8_2$-structured nanocrystals. In this nanocrystalline structure, the non-equilibrium Zr_2Al phase is clearly predominant.

- It is concluded that during heating, the crystalline debris (of the Zr_3Al phase retained in the amorphous phase) acts as nuclei for the crystallization process of the non-equilibrium phase Zr_2Al.

- When heating to 973 K, the equilibrium $L1_2$ phase starts to form and the crystals grow to a size of about 100 nm.

Chapter 6

Extreme structural inhomogeneities in high pressure torsion samples along the axial direction[1]

6.1 Overview

Structural inhomogeneities along the axial and not only the radial direction are shown to occur in Zr_3Al deformed by high-pressure torsion at room temperature. Scanning and transmission electron microscopy reveal a structure of nanocrystalline and coarse crystalline banded regions parallel to the shear plane. This contradicts the accepted equation for the microstructural evolution that is derivated from the geometry of the high pressure torsion deformation. Surface treatment of one set of samples prior to deformation allows a systematic study as it leads to the localization of the refined nanocrystalline structure at the sample surface. Once a $\sim 50\mu$m wide nanocrystalline banded layer is formed (10 turns), the residual structure remains coarse grained up to the highest deformations studied (80 turns). In the narrow interface region between coarse structure and nanocrystalline structure, the grain size decreases by three orders of magnitude within less than 10 μm. This is accompanied with a change in texture indicating the transition from a

---

[1]This chapter is based on publication [S4].

77

dislocation mediated deformation mechanism to a grain boundary mediated one. The results of the structural study are explained with the occurrence of work softening, as confirmed by microhardness measurements. Once a nanocrystalline layer being softer than the coarse structure is formed, the vast majority of strain is accomodated by that layer; this leads to extreme inhomogeneities, a large strain gradient along the axial direction and huge deviations of the actual local shear strain from the calculated one.

6.2   Introduction

High pressure torsion (HPT) is a widely used method of severe plastic deformation (SPD) [6, 7] to render disk shaped bulk materials ultrafine grained [135, 136], nanocrystalline [137, 104] or, in case of some alloys, even amorphous [138, 125]. In principle the microstructural evolution should correspond to the amount of deformation. HPT is, after a small initial compression, an almost pure shear deformation where the shear strain γ is given by the equation that is usually used to describe the HPT deformation [41]

$$\gamma = \frac{2\pi RN}{h},\tag{6.1}$$

where R is the radius of the HPT disk, N the number of rotations and h the thickness of the HPT disk.

During the last years, deviations concerning the dependence on R have been observed; e.g. after a certain amount of deformation saturation can be reached which means the structure of the HPT disk does not show a dependence on R any longer [47]. Several explanations have been put forward how this observed homogeneity can occur: e.g. due to the effects of the initial compression before the rotation is started or due to imperfect alignment of the axes of the anvils (e.g. a shift of the axes) [139]. The way how this homogeneity with respect to R is reached can be different in metals and alloys when microhardness measurements are used as an indicator for the strucutral development [140, 141]. Alternatively to the standard disk shaped samples, the use of ring samples has been proposed to achieve a homogeneous microstructure at all different stages of deformation [142].

Up till now most investigations were based on studies of plan view sections taken from the middle of the HPT disk (about at $\frac{h}{2}$) and it was assumed

that the structure does not vary within h (i.e. along the axial direction). For some materials, the homogeneity in the axial direction was shown directly (e.g. for nanocrystalline Ni [143]). Contrary to this, the present study of the $L1_2$ structured intermetallic compound Zr_3Al shows that this assumption can be misleading. Using cross section views it is demonstrated that extreme structural inhomogeneities arise in Zr_3Al HPT disks in the axial direction (direction of h). Therefore special care needs to be taken to assure that the structure of the whole HPT disk is homogeneous (i.e. does not vary within both h and R) as is frequently desired for practical applications.

6.3 Experimental procedure

The alloy Zr-26.9 at.% Al was annealed at 1160K for 24h. After this heat treatment, the samples consisted of intermetallic Zr_3Al plus about 10% residual Zr_2Al and α-Zr [66]. To prepare disks for the HPT deformation (initial thickness 0.8 mm and diameter 8 mm), the alloy was cut by spark erosion. In this study disks with two different surface treatments were used: (i) Disks with a surface as arising by spark cutting. For the HPT deformation, disks with surfaces made by spark cutting or sand blasting are frequently used since a certain roughness of the surfaces is considered to be advantageous to avoid slipping between the anvils and the disk during HPT deformation. (ii) Disks with mechanically polished surfaces (grit P120).

The HPT deformation was carried out at room temperature to various values of N from 0.25 up to 80 rotations (with a speed of 0.2 rotations min^{-1}) under a quasi hydrostatic pressure of 4 GPa. According to Eq. 6.1, at $N = 80$ a maximum shear strain of up to 250000% and a strain rate of 0.1 s^{-1} are expected to result for the outer rim of the HPT disk. Since h was reduced to about 0.6 mm by the compression and during the early stages of the deformation (N = 0.25), the final thickness of the disk was taken for the strain calculations.

Electron backscatter detection (EBSD) was performed for undeformed samples. Cross section SEM samples were prepared from the whole HPT disk. From selected regions, cross section TEM specimens were prepared using the focused ion beam (FIB) method with subsequent gentle ion milling. Plan view TEM specimens were cut from the HPT disks, grinded and electropolished in a twin jet polisher using an electrolyte consisting of 5% per-

chloric acid and 95% ethanol cooled to temperatures between 246 K and 253 K.

SEM samples were analyzed using backscattered electron detection. For conventional TEM and high resolution TEM (HRTEM) acceleration voltages of 200 kV and 300 kV were used, respectively. Both images and electron diffraction patterns were taken with a CCD camera. To gather information about the mechanical properties of the material, Vickers microhardness measurements were carried out using a load of 1500 mN.

6.4   Experimental results

6.4.1   HPT deformation of disks with spark-cut surfaces

Fig. 6.1 shows a cross section SEM image of a Zr_3Al disk prior to HPT deformation. In the upper region a multiphase structure consisting of Zr_3Al plus residual α-Zr (brighter than Zr_3Al because of its higher average atomic number) and Zr_2Al (darker) is observed. In the coarse crystalline structure (CS), the size of the residual phases is about 10 to 50 μm. As determined by EBSD, the average grain size is about 7 μm $\pm$ 2 μm and sometimes lamellae with grown-in twins are present that expand through the whole grain. In contrast to CS, a region with a rather homogeneous structure (SL, width $\sim$ 20 μm) can be seen near the surface of the disk. Frequently, in the interface region SL/CS, microcracks have been encountered. The investigation shows that the whole surface area of the HPT disk is covered by this layer that is caused by spark cutting and therefore already present prior to deformation.

Fig. 6.2 shows a cross section SEM image of an HPT disk deformed by 10 turns. Similar to the undeformed disk, a layer with a refined structure (RS) is visible near the surface of the disk. The thickness of this banded region near the surface increased from 20 μm for the undeformed disk to 50 μm. The size of the different phases in the sample interior is reduced to about 50% of that in the undeformed disk. Only close ($\sim 20\mu$m) to the interface RS/CS, a more pronounced reduction is observed and the phases exhibit elongated shapes parallel to the shear plane, perpendicular to the axial direction (AD). A sharp interface (marked by an arrow) seperates the multiphase region from region RS. Similar to the interface SL/CS, cracks have been encountered at the interface RS/CS. The thickness of RS is almost constant for a wide range of deformation degrees ($N = 10$ to 80).
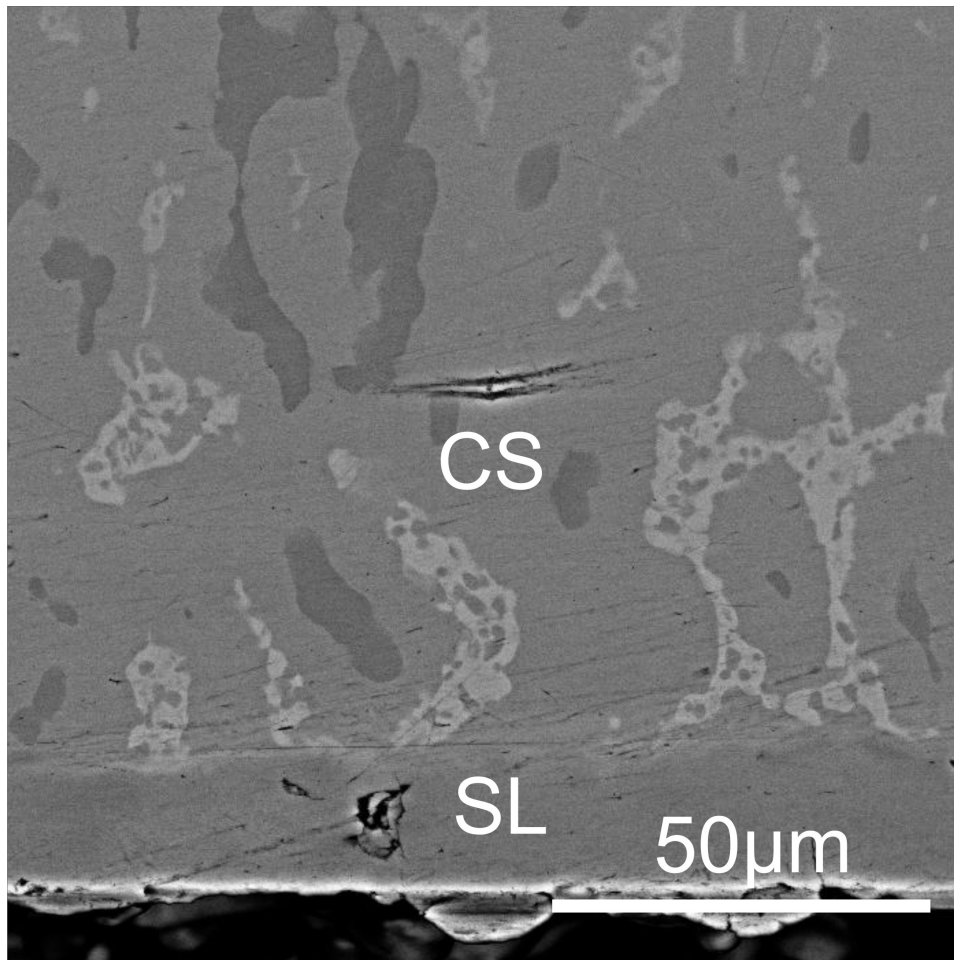
Figure 6.1: Cross section SEM image of as-cut, undeformed HPT disk. A coarse crystalline structure (CS) with grains of residual Zr_2Al (dark) and α-Zr (bright) in the Zr_3Al matrix and a surface layer (SL) affected by spark cutting that is approximately 20 μm thick are shown.
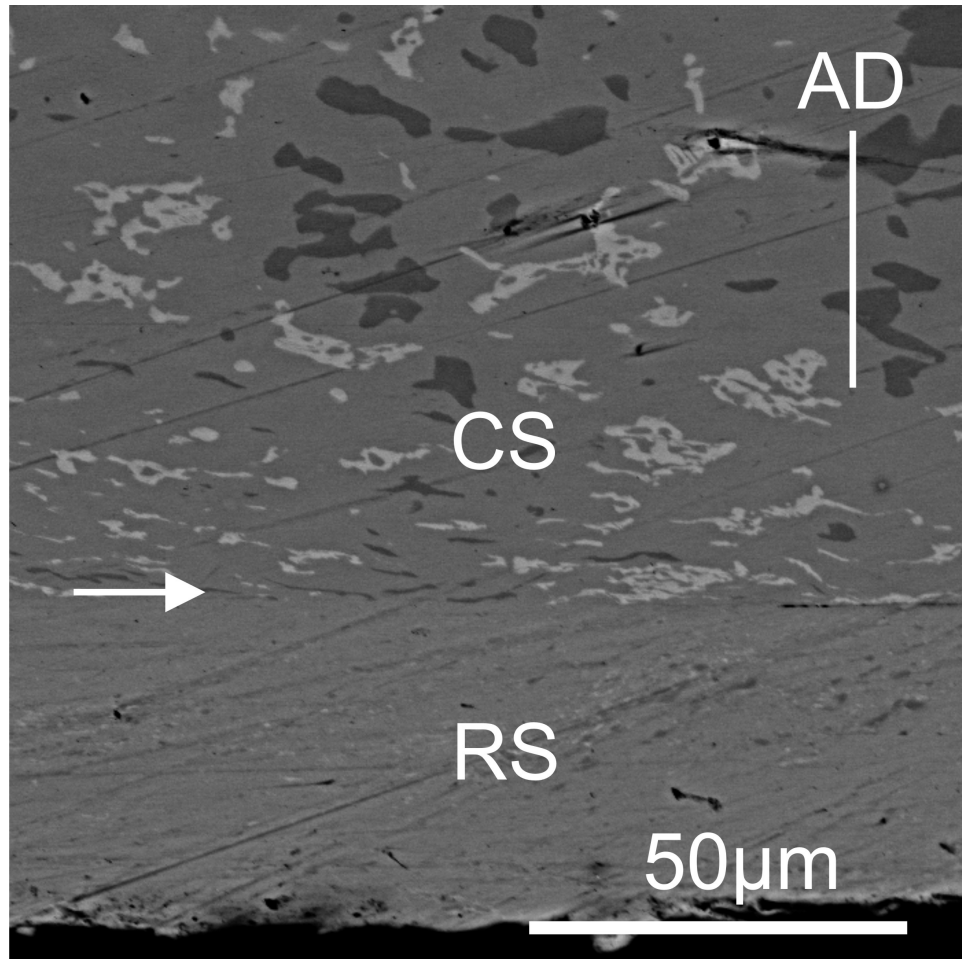
Figure 6.2: Cross section SEM image of HPT disk deformed by 10 turns. Different regions are clearly distinguishable and seperated by a sharp line (marked by arrow): a coarse crystalline structure (CS) with different phases and a region with homogeneous contrast indicating that the structure is refined (RS).

Fig. 6.3 shows a TEM dark field image of a cross section specimen that was prepared by FIB to analyze the structure of the interface region (cf. Fig. 6.2). The upper half of the image reveals a coarse grained structure (CS) with elongated grains. Evaluation of $\frac{\Delta x}{d}$ gives a rough estimate of the shear strain, which is in the order of $250 - 350$ % for the indicated grain. Near and below the bright lamella (marked by an arrow and referred to as the interface CS/RS), the grains get more and more refined and about $1\mu m$ below the lamella, a fine nanocrystalline grain structure can be seen in the region RS. Bright contrast indicates that (111) planes lie perpendicular to the axial direction since the image was taken with a (111) reflection.

Fig. 6.4 allows a detailed analysis of the refinement of the structure by a series of cross section TEM images and their corresponding diffraction patterns that were taken in the surrounding of the bright lamella (indicated in Fig. 6.3), which was used as a reference line. Fig. 6.4(a) shows a DF image of the coarse grained region, 5 μm away from the lamella. A large, horizontally elongated grain divided into subgrains is imaged. The grain size in the elongated direction is in the order of microns. Similar grains can be seen in the CS region near the interface (cf. Fig. 6.2). In Fig. 6.4(b), the diffraction pattern corresponding to Fig. 6.4(a) is presented; both fundamental and some weak superlattice reflections (e.g. {100} and {110}, marked by arrows) are present, indicating that the chemical order is reduced by the deformation [S2]. One set of {111} planes is approximately perpendicular to the axial direction (i.e. parallel to the shear plane). An analysis using the PASAD software [98] and the Scherrer formula for the {111} reflection yields a mean size of the coherently scattering domains (CSD) of 11 ± 2 nm (i.e. the subgrain size). A finer structure is visible in Fig. 6.4(c), taken in region CS about 1 μm off the lamella. The grain size is in the order of one hundred nanometers for the larger grains. The CSD size is 4 ± 1 nm, as deduced from the diffraction pattern Fig. 6.4(d). The diffraction pattern shows the development of a texture with one set of {111} reflections being perpendicular to the shear plane (leading to increased intensity of the {111} ring near the direction of AD) and two additional pairs of {111} reflections. It should be noted that the pattern remains similar when the TEM specimen is tilted around AD. Fig. 6.4(e) shows a dark field image taken adjacent ($1\mu m$ away) to the lamella in the nanocrystalline region RS. Hardly any grains are larger than 100 nm; several grains are only 10 nm
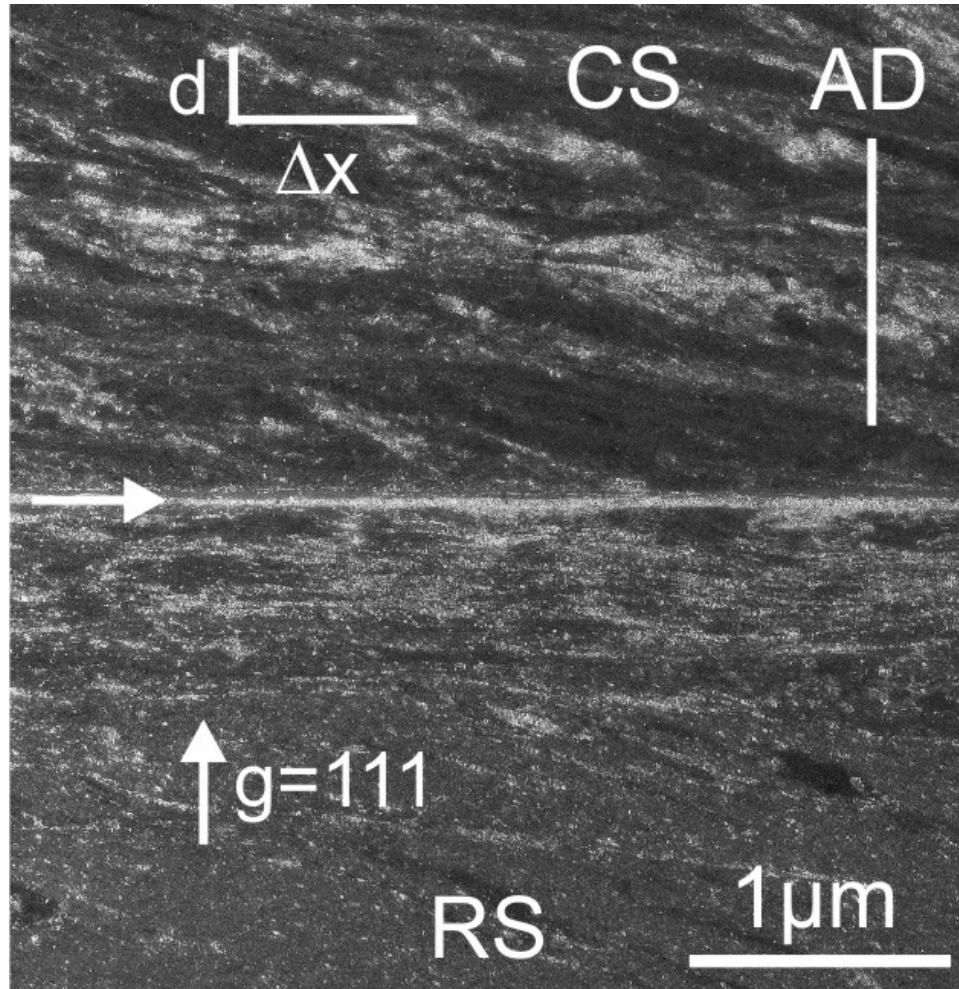
Figure 6.3: Cross section TEM dark field image of the transition area in Fig. 6.2 taken with a (111) reflection. In the upper half, relatively coarse structures (CS) with elongated grains are visible. Near and below the bright lamella, the structures are finer and at a distance of $> 1\mu$m below the lamella, a fine nanocrystalline structure is imaged near RS. Evaluation of the value $\frac{\Delta x}{d}$ allows a rough estimation of the shear strain.

small. The corresponding diffraction pattern (cf. Fig. 6.4(f)) indicates a textured nanocrystalline structure similar to Fig. 6.4(d) with a mean CSD size of 2.5 ± 1 nm. In Fig. 6.4(g) (taken in region RS, 7 μm off the lamella) most of the grains are 10 nm or smaller. The corresponding diffraction pattern (cf. Fig. 6.4(h)) shows hardly any texture and the intensity profile (resulting from PASAD) indicates the content of some amorphous material.

High resolution TEM (HRTEM) of the interface region was conducted as shown in Fig. 6.5. Across the HRTEM image, a crystalline band with a thickness of 15–25 nm can be seen that corresponds to the lamella marked by an arrow in Fig. 6.3. Lattice planes aligned parallel to the band and therefore parallel to the shear plane are visible quite clearly. Several Moiré patterns are visible, e.g. the one near M (marked by arrows) with a periodicity of 4.3 to 5 nm.

Fig. 6.6 shows a plan view TEM bright field image of an HPT disk deformed by 80 turns; the TEM specimen was cut out near the periphery of the disk. As usual for plan view specimens, the TEM foil was taken from the middle of the disk ($\sim \frac{h}{2}$). The Zr_3Al phase is imaged. The dislocation density is very high and contrast lines are observed that are interpreted as accumulations of superlattice intrinsic stacking faults lying on (111) planes, that are imaged end on (marked in Fig. 6.6). Only little reduction of the grain size relative to the undeformed sample has been encountered. This finding is also confirmed by the electron diffraction pattern (cf. inset Fig. 6.6) that shows discrete diffraction spots and superlattice reflections (the latter are marked by arrows). Therefore, grain refinement is rather weak and no significant disordering occurs in the the middle of the HPT disk. In plan view specimens, similar microstructures were observed for lower deformations (0.25, 5 and 40 turns) in Zr_3Al deformed by HPT [S1]. This means, based on the results of plan view TEM images the sample interior does not show indications for disordering, nanocrystallization or amorphization even at high deformations with N=80.

In Table 6.1 the results of the microhardness measurements are summarized. The hardness (measured at $\frac{h}{2}$) increases by the high pressure (leading to a compression of about 1.4%) at the start of the HPT deformation. The hardness saturates quickly at a rather small deformation as it hardly changes for deformations from N=0.25 to N=80 (as resulting from Eq. 6.1 this corresponds to nominal shear strains of 600 to 250000% for the outer rim of
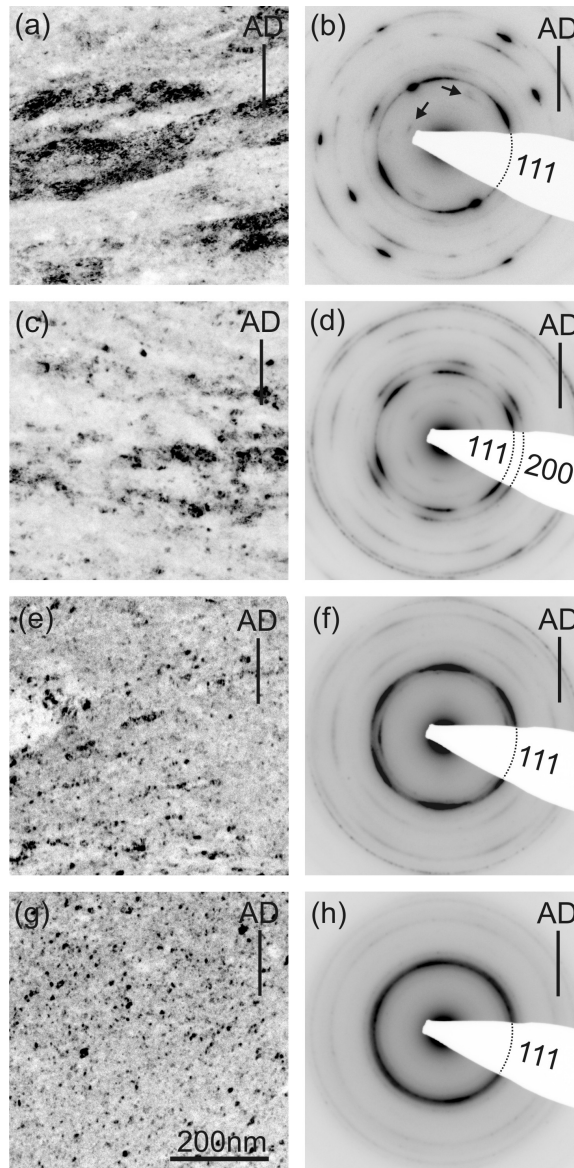
Figure 6.4: Cross section dark field images of HPT disk ($R = 10$) using a {111} reflection and their diffraction patterns with {111} and {200} rings marked (N.B. black/white inverted for better visibility). (a) and (c) are in CS region, 5 and 1 μm off the lamella, (e) and (g) are in RS, 1 μm and 7 μm off the lamella, respectively. (b), (d), (f) and (h) are the corresponding diffraction patterns. The grain size decreases from (a) (> 1 μm) to (g) ($<$ 10 nm). (h) indicates the presence of some amorphous material. In (b), superlattice reflections are marked by arrows.
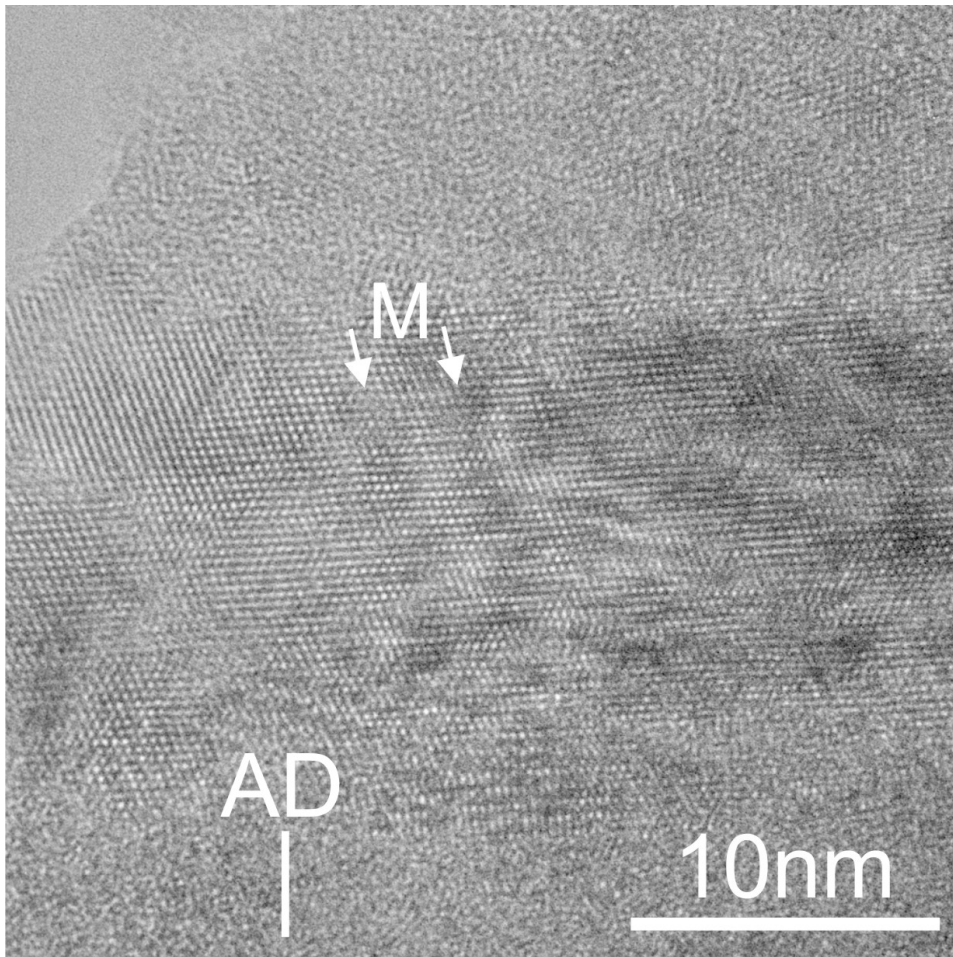
Figure 6.5: High resolution TEM image of the lamella in the interface region CS/RS. The crystallinity of the white band of Fig. 6.3 and the lattice planes in the elongated direction of the band can be seen. Moiré fringes are visible, e.g. near M (marked by arrows).
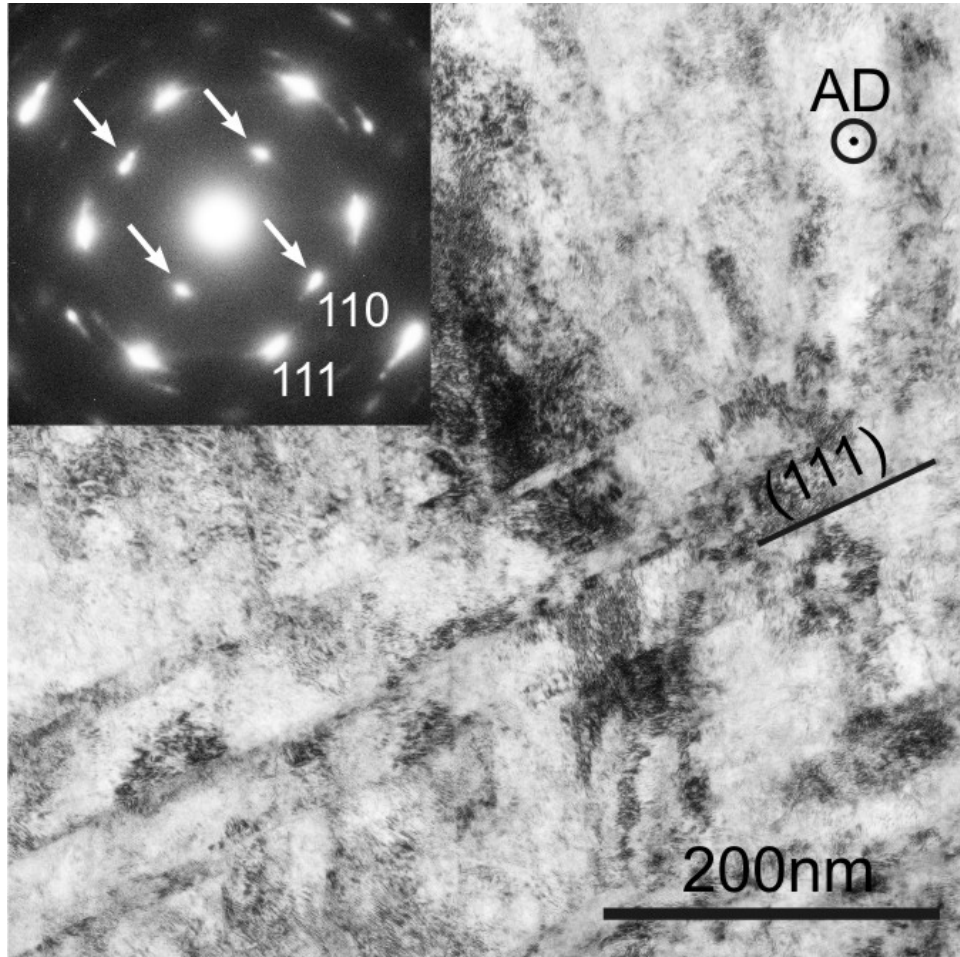
Figure 6.6: Plan view TEM bright field image and diffraction pattern of the CS region of a Zr$_3$Al HPT disk (deformed by 80 turns). The contrast indicates a high dislocation density. Traces of the (111) planes containing stacking faults are visible. The diffraction pattern shows fundamental reflections and superlattice reflections (marked by arrows) as the material is still in a coarse grained, ordered state.

deformation	region	hardness [MPa]
none	CS	2630± 60
N=0, compression only: 1.4%	CS	3180±270
HPT: N=0.25	CS	4650±130
HPT: N=80	CS	4830±130
HPT: N=40	RS	4380± 30

Table 6.1: Vickers microhardness values of the HPT disks after different deformations measured in the coarse structure (CS) and refined structure (RS).

the disk). It should be pointed out that the hardness values measured at $\frac{h}{2}$ after deformation with $N \geq 0.25$ are higher than the value measured in the layer of the refined structure.

6.4.2 Disks with mechanically polished surfaces

In addition to the disks with surfaces affected by spark erosion, disks with mechanically polished surfaces were deformed by HPT. In Fig. 6.7 and 6.8, two regions of an SEM cross section of a disk deformed for 10 turns can be seen. Fig. 6.7 and 6.8 show cross sections ~ 1.2 and 2 mm away from the rotation axis, respectively. The local occurrence of the refinement of the structure in the disk is much less systematic than in the disks with spark eroded surfaces.

Fig. 6.7, in contrast to Fig. 6.2, reveals a coarse structure near the surface with the different phases not being finer than in the undeformed structure (cf. Fig. 6.1). Approximately 100 μm away from the surface, a rather sharp transition to a refined banded region, which is about 100 μm thick, is visible. The different phases can still be identified in this region since, despite of the refinement, the larger ones are still ~ 1 μm thick and 20 μm in their elongated direction. Approaching the middle region of the disk ($\frac{h}{2}$), another transition region leads to a less refined region, similar to region CS in Fig. 6.2.

Fig. 6.8 illustrates that further away from the rotation axis ($R = 2$ mm), a different layer structure is occurring. The strongly refined banded region already visible in Fig. 6.7 is close to the surface in the left half and directly at the surface in the right half of Fig. 6.8. The refinement of the band gets more pronounced with increasing R and the individual phases cannot be resolved

anymore in the band. A sharp interface separates this band from a coarser region that shows an increasing phase size with increasing distance from the surface. In this context it must be mentioned that neither the extent of the refinement nor the distance of the refined layers from the surface of the disk exhibit a systematic correlation to R, as it may seem from the two images displayed. In the disks with polished surfaces, the appearance and the grade of refinement of the different banded regions show, apart from elongations perpendicular to the axial direction (AD), a random behaviour.

6.5   Discussion

6.5.1   Inhomogeneity of deformed disks

The experimental results show that extreme structural inhomogeneities arise in disks of Zr_3Al deformed by HPT. The inhomogeneities are found to occur in disks having surfaces prepared with and without spark erosion (cf. Fig. 6.2, 6.7 and 6.8, respectively). Still the surface layer (cf. SL in Fig. 6.1) caused by spark erosion seems to trigger the nucleation of a layer of refined structure formed during the HPT deformation (cf. RS in Fig. 6.2). This correlation facilitates by its simple geometry the present systematic study. The SL layer (molten and quenched during the spark erosion process) consists of hard, fine grained material with microcracks at the interface SL/CS. It is proposed that there, at the beginning of the shear deformation, large strains arise that start to transform CS to RS. The results of Fig. 6.6 confirm the conclusion that the deformation is highly inhomogeneous since after 80 turns, the structure at $\frac{h}{2}$ is still coarse grained and very similar to the one after much less ($N = 0.25$) and less ($N = 10$ and 40) deformation. This indicates that the inhomogeneous deformation is already in a state of saturation when the banded region of the refined structure is about 40–50 μm thick (at about $N = 10$). Therefore, the amount of deformation at both $\frac{h}{2}$ and near the surface of the HPT disk does not correspond to the value of nominal deformation as in the case when the deformation along the axial direction is homogeneous. Since the region of the coarse crystalline structure does not change significantly its structure or width from 0.25 to 80 turns, it can be estimated that it is sheared by only <600% in the outer rim (i.e. the value for 0.25 turns assuming homogeneous deformation) even in the case of 80 turns. Since 600% is a negligible shear deformation in the case of 80 turns,

Figure 6.7: Cross section SEM image of disk deformed by 10 turns with SL removed prior to deformation at R ≈ 1.2 mm. The surface is coarse grained, contrary to the disks affected by spark erosion. Finer banded regions are visible further away from the surface.
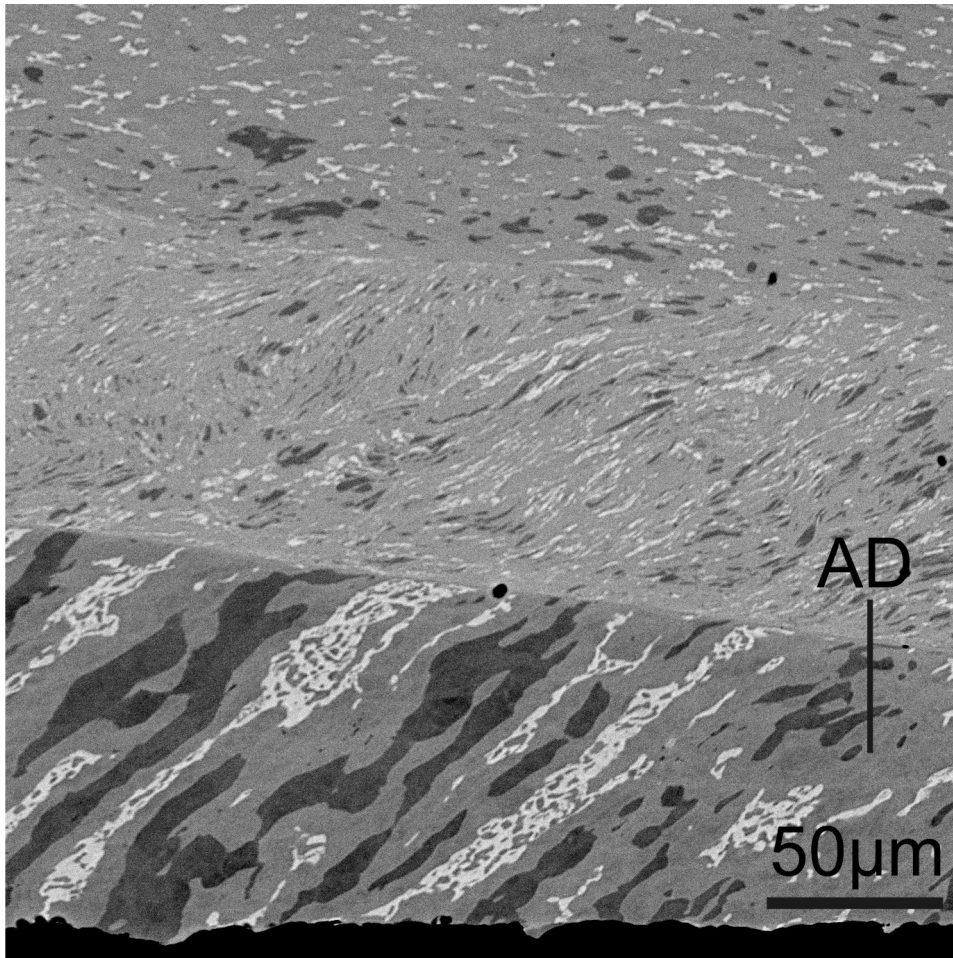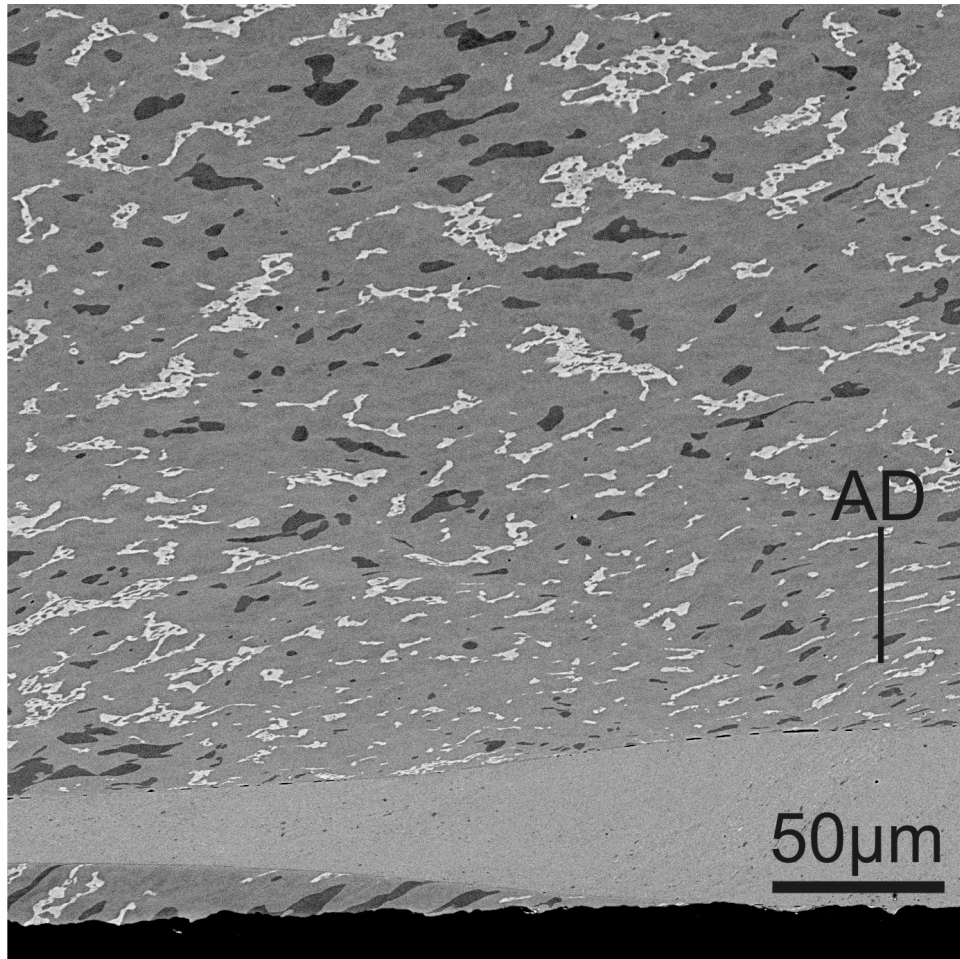
Figure 6.8: Cross section SEM image of disk deformed by 10 turns with SL removed prior to deformation at R $\approx$ 2 mm. Similar to Fig. 6.2, a banded region with homogeneous contrast can be seen at the surface of the disk in the right half of the image. In the sample interior, phases refined to different extents can be identified.

it can be concluded in good approximation that the shear deformation only takes place in the RS regions near the surfaces. By replacing the sample thickness in Eq. 6.1 by two times the width of the surface RS structure (to account for the top and bottom surface layer), the strain of the regions RS for $N = 80$ is $\sim 1400000\%$ for the outer rim. Compared to the value 250000% resulting from Eq. 6.1 for homogeneous deformation, the actual shear strains in RS and CS differ by a factor of 5 and 400, respectively.

The disks with polished surfaces do not have a similar predefined volume and thus, refined banded regions arise in a more random fashion (cf. Fig. 6.7 and 6.8), e.g. due to imperfections of the deformation process or grain orientations prone to local deformation. The formation of a continuous horizontal layer of RS through the whole disk at constant height (as it is the case for disks affected by spark erosion) is therefore not encountered. This facilitates the refinement of a higher volume fraction since the macroscopic deformation cannot be accommodated completely by RS layers if they are not covering a complete horizontal section of the disk. This also leads to the situation that in disks deformed to $N = 40$, a slightly larger volume fraction is refined as compared with disks deformed to $N = 10$.

It should be pointed out that the structural inhomogeneities observed in $L1_2$ ordered Zr_3Al seem to be of a different nature than the ones observed in $L1_2$ ordered Ni_3Al recently. There, structural inhomgeneities were found near $\frac{h}{2}$ and were at least partly attributed to material flow upon the initial compression in combination with a quasi-constrained HPT device [127]. They are present in the form of narrow nanocrystalline bands at the beginning of the deformation and in the form of single coarse grains embedded in the nanocrystalline structure at a later stage [124, 144, 126]. Since none of these characteristics are found in the present Zr_3Al samples, there does not seem to be a close correlation between the formation of inhomogeneities in the two cases.

Inhomogeneities in the axial direction after HPT deformation were also found in disks with a high thickness to diameter ratio in several materials. Homogeneous refinement could not be achieved by compressive torsion processing (i.e. in principle constrained HPT at comparably low pressures) at RT for Al5%Mg using samples 25 mm in diameter and 10 to 20 mm in thickness [50]. HPT of an Al-Mg-Sc alloy using samples 10 mm in diameter and 8 mm thick also lead to inhomogeneities [49]. It was shown for Fe that the

thickness to diameter ratio should be smaller than $\sim \frac{1}{13}$ to achieve strongly homogeneous deformation along the axial direction [51]. For the sample shown in Fig. 6.7 and 6.8, this ratio was $\frac{1}{12.3}$, for all the other samples it was between $\frac{1}{13}$ and $\frac{1}{14.3}$. This leads to the conclusion that the thickness to diameter ratio is not a major reason for the pronounced inhomogeneities observed in the present work. Moreover, it should be mentioned that the three examples with large thickness to diameter ratio, which all had experimental setups different from each other, showed different, but always systematic inhomogeneities with the structures being dependent on the position in the sample. These effects could be caused by differences in friction processes occurring between sample and anvil due to the differences in the experimental setups. In the present study, systematic inhomogeneities similar to those occurring in samples with high thickness to diameter ratio were not observed which strongly supports the conclusion that the geometry of the present samples is not a major reason for the observed inhomogeneities.

6.5.2 Structure of the interface region

The cross section TEM images allow to study the structural changes in the interface region CS/RS (cf. Fig. 6.3 and Fig. 6.4). The estimation of the shear strain $\frac{\Delta x}{d}$ of the grains in the upper half of Fig. 6.3 yields values of a few hundred percent, which is in good accordance with the estimation that the coarse grained regions are deformed by less than 600% (cf. section 6.5.1). From the results showing that in the region CS the values of the grain size are about two orders of magnitude larger than those of the coherently scattering domain size (cf. Fig. 6.4), it is concluded that the region CS is heavily deformed by dislocation mechanisms leading to many subgrain boundaries. The texture emerging in the interface region (cf. Fig. 6.4(d) and (f)) can be explained by the occurrence of the A component fiber texture $\{111\}\langle uvw \rangle$ that was theoretically predicted for torsion of fcc materials [145] and experimentally confirmed for torsion of Al and Cu [146]. Recently, the A component fiber texture found in conventional torsion was shown to contribute to the texture of HPT-deformed Al [147]. This texture component can explain the additional pair of $\{111\}$ reflections visible in Fig. 6.4 (d) and (f) and the insensibility of the diffraction pattern when tilting the specimen (cf. results of Fig. 6.4(d)). The occurrence of three pairs of $\{200\}$ reflections (instead of one as usually for a $\langle 110 \rangle$ beam direction) can

be explained as follows: one additional pair of {200} reflections arises due to the pronounced contribution of the A component of the texture. In addition, it is proposed that twinning of the nanocrystalline grains can cause the second additional pair of {200} reflections. This is supported by the specific material and deformation conditions that are valid in the present case since it was suggested that twinning is facilitated by [148]: (i) a low stacking fault energy (cf. e.g. [87] and [88]), (ii) a low deformation temperature (in the present case, the homologous temperature is ~ 0.17 for room temperature) and (iii) a nanocrystalline grain size (which is the case for the regions showing three pairs of {200} reflections).

At the bright contrast in the interface region CS/RS (marked by arrows in Fig. 6.3), lattice planes are aligned parallel to the macroscopic shear planes of the HPT deformation. In principle, it would be possible that the straight lamella could be caused by the deformation-induced elongation of a grain, but from the well defined straight shape of the lamella, this seems rather unlikely. An alternative, more likely explanation for the occurrence of a (111) oriented lamella is related to the observation of grown-in lamellae (cf. section 6.4.1). It is suggested that in such a very narrow grown-in lamella, nucleation of dislocations is hindered and therefore fragmentation is impeded. Thus, at a deformation stage at which the grains adjacent to this lamella are already severely refined, the lamella is still several microns long. Still, some defects are visible in the lamella as shown in the HRTEM image (cf. Fig. 6.5). From the distance of the Moiré fringes (marked by arrows near M), the lattice rotation between overlapping crystalline areas can be calculated [105] to be $7 - 8°$, which corresponds to a small angle grain boundary (i.e. a subgrain boundary) that does not refine the grain severely. An additional aspect providing increased stability for this lamella is the fact that the macroscopic shear plane and the lattice plane in the lamella have the same orientation. This greatly favours a single slip system and thus makes the formation of 3D dislocation networks leading to grain boundaries less likely. In initially coarse crystalline regions not oriented in this special way, a 3D slip structure develops due to slip on planes inclined to the macroscopic shear plane and by the action of internal stresses.

In the RS region, the observed nanocrystalline structures with grains < 10 nm and the occurrence of some amorphous phase lead to the conclusion that in this area, the deformation mechanism is not dominated by disloca-

tions but by alternative mechanisms (e.g. grain boundary sliding). This is confirmed by the loss of the texture in region RS (cf. Fig. 6.4(h)). This transition from a dislocation mediated deformation mechanism to a grain boundary mediated one agrees with an XRD study of the texture evolution with increasing strain in Ni deformed by repeated cold rolling [56]. The highly different values of strain in the interface region CS/RS, which are causing a decrease in grain size by three orders of magnitude within less than 10μm (cf. Fig. 6.4) yield a large strain gradient causing the cracks that are observed sometimes when the HPT pressure is released.

6.5.3   Reasons for the inhomogeneous deformation

The results of the microhardness measurements (cf. Table 6.1) can be used to explain the extreme structural inhomogeneities occurring in the HPT disks. It is important to note that the value of the hardness of the refined structure is even lower than that of the coarse grained material after a rather small HPT deformation (0.25 turns only). This occurrence of work softening has the consequence that once a softer layer is formed it will carry most of the deformation which is in agreement with the microstructural findings (cf. Fig. 1–4). Since an amorphous phase can be formed in the case of shear localization [141] and sliding interfaces [149], it is suggested that together with the structural refinement, that decreases the grain size by three orders of magnitude within a few micrometers, an amorphous phase starts to form that facilitates the softening. It seems safe to assume that in samples that deform inhomogeneously in their axial direction due to a high thickness to diameter ratio [50, 49, 51], such a process leading to an inverse Hall-Petch behaviour could intensify and stabilize the inhomogeneities.

It should be mentioned that in the case of an HPT deformation the occurrence of work softening does not lead to a mechanical instability since the confined deformation geometry does not allow shape changes of the disk. Therefore work softening will cause structural inhomogeneities in an HPT deformed disk whereas work softening occurring in a tensile deformation will lead to mechanical failure of the sample.

To bypass the occurrence of inhomogeneities unwanted for applications, alternative methods of SPD of a bulk material could be used: For example in the case of the intermetallic compound Zr_3Al, repeated cold rolling leads to homogeneous nanocrystalline or even amorphous structures [S3]. It is

proposed that in this case, the preservation of coarse grained, relatively low deformed regions is suppressed by the complex 3D rolling geometry. In contrast, in the case of the pure shear deformation of a well aligned HPT deformation, the shape of the sample is unchanged and a refined structure that is softer can carry the induced deformation thus facilitating the survival of coarse grained regions.

Finally, the SEM and the TEM observations together with the hardness measurements of the different structures allow to draw a consistent picture explaining the extreme structural inhomogeneities in HPT disks, be they affected by spark erosion or not.

6.6 Conclusions

Systematic investigations are used to analyze the structural inhomogeneities in L1$_2$ long range ordered Zr$_3$Al subjected to deformation by HPT from the atomic scale to the scale of the HPT disk. The analysis of the experimental findings leads to the following conclusions:

- The SEM and TEM cross section results show structural inhomogeneities parallel to the axis of the HPT deformation. This leads to the conclusion that the equation used to describe the HPT deformation ($\gamma = \frac{2\pi RN}{h}$) is not fulfilled.

- The inhomogeneities consist of banded regions of nanograined and coarse grained material aligned predominantly parallel to the shear plane. A surface treatment can be used to localize the nanograined region thus facilitating a systematic study.

- In the interface region between the nanograined and the coarse grained material, the grain size decreases by three orders of magnitude and the diffraction pattern changes from a pronounced fiber texture to diffraction rings of rather homogeneous intensity. This leads to the conclusion that the deformation mechanism changes from dislocation mediated intragranular processes to grain boundary mediated intergranular processes.

- The results of the microhardness measurements show a softening of the nanocrystalline material. Therefore it is concluded that banded

regions that are softened by deformation cause structural inhomogeneities. It is proposed that any deformation mechanism causing work softening in HPT (e.g. inverse Hall-Petch) will lead to similar results.

- Localisation of the strain can explain the deviations from the calculated strain. In the case of 80 turns, the shear strains induced in the banded surface layer and in the coarse grained sample interior are 5 times higher and 400 times lower, respectively, than the calculated strain for homogeneous deformation.

- Inhomogeneous deformation leads to strain gradients that can cause crack formation. It is concluded that the geometric confinement of the HPT setup prevents catastrophic failure during the deformation as it would be expected to occur in the case of work softening in a tensile deformation.

Chapter 7

Summary and Outlook

7.1 Summary

In the present thesis, the effect of SPD on the intermetallic compound Zr_3Al was investigated. Based on TEM, SEM and XRD measurements, the structural evolution and the phase transitions during SPD were studied. DSC and microhardness measurements elucidated the thermal stability and the hardness changes of the metastable structures obtained after different SPD treatments.

In chapter 3, Zr_3Al deformed by HPT at room temperature was investigated by TEM. No significant grain refinement or disordering could be observed, although by marking the top and bottom surfaces of the HPT samples it was shown that the actual global shear strain induced corresponded to the one calculated from Eq. 1.3. It was successfully shown at a later stage of this thesis and is presented in detail in chapter 6, that the local deformation behaviour was highly inhomogeneous. It was revealed that this was due to the chosen HPT sample preparation (spark erosion affected surfaces). In combination with the TEM sample preparation method (plan view samples cut from a region away from the top and bottom surfaces of the HPT disk), only slightly deformed sample volumes were studied in the TEM leading to the observation of a high density of dislocations and SISF, but no significant grain refinement. Twinned structures were observed which are, after taking into account all the results obtained in the course of this thesis, believed to be caused by growth rather than by deformation. The EBSD measurements described in chapter 6 (cf. Fig. 2.5) showing twins in the undeformed

structure support this view. The comparison of the findings in chapter 3 to the findings in chapter 6 shows that cross section studies of disks deformed by HPT can be very important for a comprehensive understanding of the applied deformation process.

In chapter 4 the dissociation of dislocations in the three $L1_2$ structured intermetallic alloys Cu_3Au, Ni_3Al and Zr_3Al and its influence on the saturation grain sizes were compared. Despite the similarity of the long-range ordered structure, these three compounds exhibit a different dislocation dissociation behaviour at room temperature, at which deformation was done. $\langle 110 \rangle$ superlattice glide dislocations dissociate into $\frac{1}{2} \langle 110 \rangle$ full dislocations comprising an APB in Cu_3Au and mostly into $\frac{1}{3} \langle 211 \rangle$ super Shockley dislocations comprising SISF in Zr_3Al. In Ni_3Al, both dissociations are observed at room temperature, the former being more dominant. This difference lead to more pronounced disordering and a larger average saturation grain size upon HPT for the compounds with stronger dominance of the APB-dissociated dislocations. It was suggested that grain size reduction is limited by disordering since the formation of superlattice dislocations is not necessary anymore in disordered structures to carry deformation and therefore, recovery is facilitated (e.g. by cross-slip annihilation of screw dislocations). In Zr_3Al these processes are less pronounced and in addition, the widely dissociated superlattice partials cannot fully annihilate leading to a high density of residual dislocations that are causing further grain refinement and eventually amorphization. This idea is supported by the fact that amorphization in the Zr_3Al samples studied was only observed for deformation at liquid nitrogen temperature. There, the fraction of SISF-dissociated dislocations is even higher than at room temperature, which was shown by the retained chemical order in NC samples.

In chapter 5, the effect of RCR on Zr_3Al at room temperature was reported. It was shown that after relatively small deformations (compared to the HPT deformations), the effect on the structural evolution of the material was much more pronounced than in the HPT experiments. It was shown by XRD that after 80 foldings, the sample was rendered amorphous. TEM showed small residual crystallites (typically < 10 nm) homogeneously distributed in the amorphous matrix. DSC measurements revealed a crystallization peak at ~ 720 K. The crystallization enthalpy was determined to be about 40 J/g. After the crystallization, the sample consisted of NC ($10 - 20$

nm) grains with the $B8_2$ structure. It was suggested that the densely distributed residual crystallites in the amorphous matrix acted as nuclei for the crystallization and were thus causing the small grain size. Upon heating to 973 K in the DSC, a second peak could be seen, which was caused by grain growth and phase transformations. The samples heated to 973 K exhibited a grain size of $100-200$ nm. The $B8_2$ structure was still dominant, but the $L1_2$ structure already started to form amongst others after this temperature treatment.

In chapter 6, a detailed systematic analysis of Zr_3Al deformed by HPT was presented to complement the findings of chapter 3. A combination of SEM and TEM measurements allowed a multiscale study of the deformation process and showed extreme structural inhomogeneities in the axial direction of the HPT disks. Samples with thin surface layers ($\sim 20\mu m$ thick) affected by spark erosion and samples with the surface layers removed prior to deformation were deformed for different numbers of HPT turns. SEM cross section images showed that the presence of thin surface layers affected by spark cutting lead to a continuous surface layer with refined NC structure of $\sim 50\mu m$ thickness after HPT deformation. The residual sample volume was only slightly refined which means that the vast majority of deformation took place in the surface layers. If the surface layers were removed prior to the HPT deformation, refined banded regions that are aligned parallel to the shear plane were formed at random positions in the sample upon deformation. Apart from the volume in the refined banded regions, in both cases the samples showed grain sizes $> 1\mu m$ and a high grade of chemical order, as was also shown in chapter 3. In a sample affected by spark erosion and subsequently deformed by HPT, the interface region between the refined layer and the coarse grained sample interior was analyzed by a cross section TEM study. It was shown that the transition from coarse grains (in the order of $10\mu m$) to small NC grains ($\sim 10nm$) occurred within a distance of a few microns only. Within this region, electron diffraction patterns indicating a typical torsion texture developed in the coarser grained area and transformed into NC patterns with hardly any texture in the finer grained area. This indicated a localized change in the deformation mechanism from dislocation mediated to grain boundary mediated processes within the transition region. In the refined region, electron diffraction patterns indicated the presence of some amorphous material. Vickers microhardness

measurements showed that the refined regions are $\sim 10\%$ softer than the work-hardened coarse-grained regions. From that it was concluded that the softening leads to a localization of the deformation in the refined regions. Therefore, the coarse grained regions were hardly deformed anymore once a refined region had been formed, leading to huge discrepancies between the shear strain calculated for an ideal torsion experiment and the locally induced shear strain.

7.2   Main conclusions

Based on the findings in the course of this thesis, the following main conclusions can be drawn:

- The dislocation dissociation behaviour strongly influences the state of chemical order, the final grain size and the amorphization behaviour of intermetallic compounds of the $L1_2$ structure deformed by HPT. Differences in the dislocation dissociation behaviour can be caused by both an intrinsically different behaviour for different compounds or by a change in the deformation temperature.

- RCR shows a higher potential for amorphization than HPT in the case of Zr_3Al. After 80 foldings, the samples deformed by RCR are almost fully amorphous. It is concluded that the complex 3D rolling geometry is more beneficial for amorphization than the pure shear deformation of HPT.

- Densely distributed residual nanocrystals (typically < 10 nm) were found in Zr_3Al amorphized by RCR. This debris acting as nuclei is the reason for the small grain size of the material after heating it to the crystallization temperature.

- HPT of Zr_3Al can lead to tremendous structural inhomogeneities along the axial direction of the sample and therefore, large discrepancies between calculated (idealized) and actual local shear strain arise. A major reason for these inhomogeneities is deformation softening and thus, they can occur in all materials that exhibit work softening.

- In the interface region between coarse grained and nanograined regions in Zr_3Al deformed by HPT, local texture measuerments by electron

diffraction indicate that the reduction in grain size is accompanied by a change in the deformation mechanism from dislocation mediated processes to grain boundary mediated processes. The different deformation mechanism in the refined material is, together with the presence of some amorphous material, the reason for the observed softening.

7.3   Outlook

Cross section TEM and SEM studies of samples deformed by RCR to a low number of foldings could give an insight into the anisotropy of the structural evolution in the early stages of deformation.

The production of homogeneous NC long range ordered Zr_3Al could be accomplished by amorphization by RCR and a subsequent heat treatment different from the ones performed in the course of this thesis. It should be checked if long annealing times at relatively low temperatures lead to $L1_2$ structured samples without causing excessive grain growth.

Preliminary results give a hint on a beneficial effect of higher pressure on the sample homogeneity after HPT deformation. Systematic studies of Zr_3Al deformed by HPT at different pressures (from the lowest pressure possible without slipping between anvils and sample to high pressure (~ 10 GPa) could elucidate the effect of pressure on the homogeneity of samples deformed by HPT and are an additional possible way to get homogeneous NC Zr_3Al.

When bulk homogeneously NC samples are available, tensile tests would supplement the hardness tests to get more information about the mechanical properties of NC Zr_3Al. Irradiation tests of bulk NC samples could answer the still open question if the major drawback for the use of Zr_3Al as a reactor material (i.e. low irradiation resistance) could be overcome by nanostructuring.

List of included articles

[S1] D. Geist, C. Rentenberger, and H. P. Karnthaler. High pressure torsion of intermetallic Zr_3Al. *Materials Science Forum*, 584-586:553–558, 2008.

[S2] D. Geist, C. Gammer, C. Mangler, C. Rentenberger, and H. P. Karnthaler. Electron microscopy of severely deformed $L1_2$ intermetallics. *Philosophical Magazine*, 90(35-36):4635–4645, 2010.

[S3] D. Geist, S. Ii, K. Tsuchiya, H.P. Karnthaler, G. Stefanov, and C. Rentenberger. Nanocrystalline Zr_3Al made through amorphization by repeated cold rolling and followed by crystallization. *Journal of Alloys and Compounds*, 509(5):1815–1818, 2011.

[S4] D. Geist, H.P. Karnthaler, and C. Rentenberger. Extreme structural inhomogeneities in high pressure torsion samples along the axal direction. *Acta Materialia*, 2011. submitted.

Bibliography

[1] H. Gleiter. Nanocrystalline Materials. *Progress In Materials Science*, 33(4):223–315, 1989.

[2] G. Palumbo, S. J. Thorpe, and K. T. Aust. On the Contribution of Triple Junctions To the Structure and Properties of Nanocrystalline Materials. *Scripta Metallurgica Et Materialia*, 24(7):1347–1350, 1990.

[3] H. Gleiter. Nanostructured materials: Basic concepts and microstructure. *Acta Materialia*, 48(1):1–29, 2000.

[4] MA Meyers, A Mishra, and DJ Benson. Mechanical properties of nanocrystalline materials. *Progress In Materials Science*, 51(4):427–556, 2006.

[5] V. Viswanathan, T. Laha, K. Balani, A. Agarwal, and S. Seal. Challenges and advances in nanocomposite processing techniques. *Materials Science & Engineering R-reports*, 54(5-6):121–285, 2006.

[6] R. Z. Valiev, Y. Estrin, Z. Horita, T. G. Langdon, M. J. Zehetbauer, and Y. T. Zhu. Producing bulk ultrafine-grained materials by severe plastic deformation. *JOM*, 58(4):33–39, 2006.

[7] Alexander P. Zhilyaev and Terence G. Langdon. Using high-pressure torsion for metal processing: Fundamentals and applications. *Progress in Materials Science*, 53(6):893–979, 2008.

[8] ISI Web of Knowledge, http://apps.isiknowledge.com [accessed 2011-02-15].

[9] E. O. Hall. The Deformation and Ageing of Mild Steel .3. Discussion of Results. *Proceedings of the Physical Society of London Section B*, 64(381):747–753, 1951.

[10] N. J. Petch. The Cleavage Strength of Polycrystals. *Journal of the Iron and Steel Institute*, 174(1):25–28, 1953.

[11] J. Chen, L. Lu, and K. Lu. Hardness and strain rate sensitivity of nanocrystalline Cu. *Scripta Materialia*, 54(11):1913–1918, 2006.

[12] G. W. Nieman, J. R. Weertman, and R. W. Siegel. Mechanical behavior of Nanocrystalline Cu and Pd. *Journal of Materials Research*, 6(5):1012–1027, 1991.

[13] Y. M. Wang, M. W. Chen, F. H. Zhou, and E. Ma. High tensile ductility in a nanostructured metal. *Nature*, 419(6910):912–915, 2002.

[14] M. Dao, L. Lu, R. J. Asaro, J. T. M. De Hosson, and E. Ma. Toward a quantitative understanding of mechanical behavior of nanocrystalline metals. *Acta Materialia*, 55(12):4041–4065, 2007.

[15] P. G. Sanders, J. A. Eastman, and J. R. Weertman. Elastic and tensile behavior of nanocrystalline copper and palladium. *Acta Materialia*, 45(10):4019–4025, 1997.

[16] Y. T. Zhu and T. G. Langdon. Influence of grain size on deformation mechanisms: An extension to nanocrystalline materials. *Materials Science and Engineering A-Sstructural Materials Properties Microstructure and Processing*, 409(1-2):234–242, 2005.

[17] C. S. Pande and K. P. Cooper. Nanomechanics of Hall-Petch relationship in nanocrystalline materials. *Progress In Materials Science*, 54(6):689–706, 2009.

[18] R. A. Masumura, P. M. Hazzledine, and C. S. Pande. Yield stress of fine grained materials. *Acta Materialia*, 46(13):4527–4534, 1998.

[19] J. Schiotz and K. W. Jacobsen. A maximum in the strength of nanocrystalline copper. *Science*, 301(5638):1357–1359, 2003.

[20] H. Van Swygenhoven and P. M. Derlet. Grain-boundary sliding in nanocrystalline fcc metals. *Phys. Rev. B*, 64(22):224105–, 2001.

[21] T. Shimokawa, A. Nakatani, and H. Kitagawa. Grain-size dependence of the relationship between intergranular and intragranular deformation

of nanocrystalline al by molecular dynamics simulations. *Physical Review B*, 71(22):224110, 2005.

[22] H. S. Kim and Y. Estrin. Phase mixture modeling of the strain rate dependent mechanical behavior of nanostructured materials. *Acta Materialia*, 53(3):765–772, 2005.

[23] C. A. Schuh, T. G. Nieh, and H. Iwasaki. The effect of solid solution W additions on the mechanical properties of nanocrystalline Ni. *Acta Materialia*, 51(2):431–443, 2003.

[24] Tohru Yamasaki. High-strength nanocrystalline Ni-W alloys produced by electrodeposition and their embrittlement behaviors during grain growth. *Scripta Materialia*, 44(8-9):1497–1502, 2001.

[25] A. Giga, Y. Kimoto, Y. Takigawa, and K. Higashi. Demonstration of an inverse Hall-Petch relationship in electrodeposited nanocrystalline Ni-W alloys through tensile testing. *Scripta Materialia*, 55(2):143–146, 2006.

[26] Y. Chimi, A. Iwase, N. Ishikawa, A. Kobiyama, T. Inami, and S. Okuda. Accumulation and recovery of defects in ion-irradiated nanocrystalline gold. *Journal of Nuclear Materials*, 297(3):355–357, 2001.

[27] A. R. Kilmametov, D. V. Gunderov, R. Z. Valiev, A. G. Balogh, and H. Hahn. Enhanced ion irradiation resistance of bulk nanocrystalline TiNi alloy. *Scripta Materialia*, 59(10):1027–1030, 2008.

[28] J. M. Zhang, J. Lian, A. F. Fuentes, F. X. Zhang, M. Lang, F. Y. Lu, and R. C. Ewing. Enhanced radiation resistance of nanocrystalline pyrochlore Gd-2(Ti0.65Zr0.35)(2)O-7. *Applied Physics Letters*, 94(24):243110, 2009.

[29] Al Meldrum, Lynn A. Boatner, and Rodney C. Ewing. Size effects in the irradiation-induced crystalline-to-amorphous transformation. *Nuclear Instruments and Methods in Physics Research Section B: Beam Interactions with Materials and Atoms*, 207(1):28–35, 2003.

[30] Stefan Wurster and Reinhard Pippan. Nanostructured metals under irradiation. *Scripta Materialia*, 60(12):1083–1087, 2009.

[31] X. M. Bai, A. F. Voter, R. G. Hoagland, M. Nastasi, and B. P. Uberuaga. Efficient Annealing of Radiation Damage Near Grain Boundaries via Interstitial Emission. *Science*, 327(5973):1631–1634, 2010.

[32] M. Samaras, P. M. Derlet, H. Van Swygenhoven, and M. Victoria. Atomic scale modelling of the primary damage state of irradiated fcc and bcc nanocrystalline metals. *Journal of Nuclear Materials*, 351(1-3):47–55, 2006.

[33] P. Singh, A. Kumar, Deepak, and D. Kaur. ZnO nanocrystalline powder synthesized by ultrasonic mist-chemical vapour deposition. *Optical Materials*, 30(8):1316–1322, 2008.

[34] A. Simchi, R. Ahmadi, S. M. S. Reihani, and A. Mahdavi. Kinetics and mechanisms of nanoparticle formation and growth in vapor phase condensation process. *Materials & Design*, 28(3):850–856, 2007.

[35] T. Spassov and U. Koster. Thermal stability and hydriding properties of nanocrystalline melt-spun MgZr$_{63}$Ni$_{30}$Y$_7$ alloy. *Journal of Alloys and Compounds*, 279(2):279–286, 1998.

[36] L.D. Rafailovic, H.P. Karnthaler, T. Trisovic, and D.M. Minic. Microstructure and mechanical properties of disperse Ni-Co alloys electrodeposited on Cu substrates. *Materials Chemistry and Physics*, 120(2-3):409–416, 2010.

[37] D. R. Allen, J. C. Foley, and J. H. Perepezko. Nanocrystal development during primary crystallization of amorphous alloys. *Acta Materialia*, 46(2):431–440, 1998.

[38] V.M. Segal, V.I. Reznikov, A.E. Drobyshevskii, and V.I. Kopylov. Plastic Metal Working by Simple Shear. *Izv Akad Nauk SSSR Met*, (1):115–123, 1981.

[39] R.Z. Valiev, N.A. Krasilnikov, and N.K. Tsenev. Plastic deformation of alloys with submicron-grained structure. *Materials Science and Engineering: A*, 137:35–40, 1991.

[40] Ruslan Z. Valiev and Terence G. Langdon. Principles of equal-channel angular pressing as a processing tool for grain refinement. *Progress in Materials Science*, 51(7):881–981, 2006.

[41] R. Z. Valiev, R. K. Islamgaliev, and I. V. Alexandrov. Bulk Nanostructured Materials from Severe Plastic Deformation. *Progress in Materials Science*, 45(2):103–189, 2000.

[42] R. Y. Lapovok. The role of back-pressure in equal channel angular extrusion. *Journal of Materials Science*, 40(2):341–346, 2005.

[43] Yoshinori Iwahashi, Jingtao Wang, Zenji Horita, Minoru Nemoto, and Terence G. Langdon. Principle of equal-channel angular pressing for the processing of ultra-fine grained materials. *Scripta Materialia*, 35(2):143–146, 1996.

[44] R. Srinivasan, B. Cherukuri, and P. K. Chaudhury. Scaling up of equal channel angular pressing (ECAP) for the production of forging stock. *Nanomaterials By Severe Plastic Deformation*, 503-504:371–378, 2006.

[45] P. W. Bridgman. Effects of high shearing stress combined with high hydrostatic pressure. *Physical Review*, 48(10):825–847, 1935.

[46] R. Z. Valiev, O. A. Kaibyshev, R. I. Kuznetsov, R.Sh. Musalimov, and N. K. Tsenev. Low-temperature superplasticity of metallic materials. *Soviet Physics - Doklady*, 33(8):626–7, 1988.

[47] R. Pippan, S. Scheriau, A. Taylor, M. Hafok, A. Hohenwarter, and A. Bachmaier. Saturation of Fragmentation During Severe Plastic Deformation. *Annual Review of Materials Research*, 40:319–343, 2010.

[48] R. Pippan, S. Scheriau, A. Hohenwarter, and M. Hafok. Advantages and limitations of HPT: a review. *Materials Science Forum*, 584-586:16–21, 2008.

[49] G. Sakai, K. Nakamura, Z. Horita, and T. G. Langdon. Developing high-pressure torsion for use with bulk samples. *Materials Science and Engineering A-structural Materials Properties Microstructure and Processing*, 406(1-2):268–273, 2005.

[50] Y. Kume, M. Kobashi, and N. Kanetake. Homogeneity of Grain Refinement of Aluminum Alloy with Compressive Torsion Processing. *Advanced Materials and Processing*, 26-28:107–110, 2007.

[51] A. Hohenwarter, A. Bachmaier, B. Gludovatz, S. Scheriau, and R. Pippan. Technical parameters affecting grain refinement by high pressure torsion. *International Journal of Materials Research*, 100(12):1653–1661, 2009.

[52] M. Atzmon, K. M. Unruh, and W. L. Johnson. Formation and Characterization of Amorphous Erbium-based Alloys Prepared By Near-isothermal Cold-rolling of Elemental Composites. *Journal of Applied Physics*, 58(10):3865–3870, 1985.

[53] Y. Saito, N. Tsuji, H. Utsunomiya, T. Sakai, and R.G. Hong. Ultra-fine grained bulk aluminum produced by accumulative roll-bonding (ARB) process. *Scripta Materialia*, 39(9):1221–1227, 1998.

[54] Y. Saito, H. Utsunomiya, N. Tsuji, and T. Sakai. Novel ultra-high straining process for bulk materials–development of the accumulative roll-bonding (ARB) process. *Acta Materialia*, 47(2):579–583, 1999.

[55] G. Wilde, G. P. Dinda, and H. Rosner. Synthesis of bulk nanocrystalline materials by repeated cold rolling. *Advanced Engineering Materials*, 7(1-2):11–15, 2005.

[56] G.P. Dinda, H. Rosner, and G. Wilde. Synthesis of bulk nanostructured Ni, Ti and Zr by repeated cold-rolling. *Scripta Materialia*, 52(7):577 – 582, 2005.

[57] W. Lechner, W. Puff, G. Wilde, and R. Wurschum. Chemical sensitive positron-annihilation study of amorphization and nanocrystallization processes by repeated roll bonding. *Materials Science Forum*, pages 209–14, 2008.

[58] Nobuhiro Tsuji. *Bulk Nanostructured Materials*, chapter Fabrication of Bulk Nanostructured Materials by Accumulative Roll Bonding (ARB), pages 235–253. Wiley-VCH, 2009.

[59] T. Wang, Z. P. Jin, and J. C. Zhao. Thermodynamic assessment of the Al-Zr binary system. *Journal of Phase Equilibria*, 22(5):544–551, 2001.

[60] G. Ghosh and M. Asta. First-principles calculation of structural energetics of Al-TM (TM = Ti, Zr, Hf) intermetallics. *Acta Materialia*, 53(11):3225–3252, 2005.

[61] NIMS Atom Work database [accessed 2010-07-01] http://crystdb.nims.go.jp/.

[62] S. J. Kim, R. J. Kematick, S. S. Yi, and H. F. Franzen. On the Stabilization of Zr_5Al_3 in the Mn_5Si_3-type Structure by Interstitial Oxygen. *Journal of the Less-common Metals*, 137(1-2):55–59, 1988.

[63] H. Zhang and S. Q. Wang. The structural stabilities of the intermetallics and the solid-state phase transformations induced by lattice vibration effects in the Al-Zr system by first-principles calculations. *Journal of Materials Research*, 25(9):1689–1694, 2010.

[64] M. Alatalo, M. Weinert, and R. E. Watson. Stability of Zr-Al alloys. *Physical Review B*, 57(4):R2009–R2012, 1998.

[65] D. K. Tappin, I. M. Robertson, and H. K. Birnbaum. Enhancement of the Electron-Irradiation-Induced Amorphization of Zr_2Ni and Zr_3Al by Hydrogen. *Physical Review B*, 51(21):14854–14860, 1995.

[66] E.M. Schulson. *Structural Applications of Intermetallic Compounds*, chapter Zr_3Al: A Potential Nuclear Reactor Structural Material, pages 137–150. John Wiley & Sons Ltd, 1995.

[67] W. J. Meng, J. Faber, P. R. Okamoto, L. E. Rehn, B. J. Kestel, and R. L. Hitterman. Neutron-diffraction and Transmission Electron-microscopy Study of Hydrogen-induced Phase-transformations in Zr_3Al. *Journal of Applied Physics*, 67(3):1312–1319, 1990.

[68] A. Peruzzi. Reinvestigation of the Zr-rich End of the Zr-Al Equilibrium Phase-diagram. *Journal of Nuclear Materials*, 186(2):89–99, 1992.

[69] N.J. Clark and E. Wu. Hydrogen absorption in the Zr—Al system. *Journal of the Less Common Metals*, 163(2):227 – 243, 1990.

[70] Derek O. Northwood. The development and applications of Zirconium alloys. *Materials & Design*, 6(2):58–70, 1985.

[71] L. M. Howe, M Rainville, and E. M. Schulson. Transmission Electron-Microscopy Investigations of Ordered Zr_3Al. *Journal Of Nuclear Materials*, 50(2):139–154, 1974.

[72] E. M. Schulson. Tensile and Corrosion Behavior of Ordered Zr_3Al-based Alloys. *Journal of Nuclear Materials*, 50(2):127–138, 1974.

[73] E. M. Schulson and D. B. Graham. The Peritectoid Formation of Ordered Zr_3Al. *Acta Metallurgica*, 24(7):615–625, 1976.

[74] E. M. Schulson and J. A. Roy. Work Hardening of the $L1_2$ Phase Zr_3Al. *Acta Metallurgica*, 26(1):15–28, 1978.

[75] E. M. Schulson and J. A. Roy. The yield strength of the $L1_2$ phase Zr_3Al. *Acta Metallurgica*, 26(1):29–38, 1978.

[76] E. M. Schulson and T. P. Trottier. The Oxidation of Ordered Zr_3Al. *Metallurgical Transactions A-physical Metallurgy and Materials Science*, 11(5):727–738, 1980.

[77] H.E Rosinger and B.J.S Wilkins. The tensile properties and fracture toughness of a Zr_3Al-based alloy after fast neutron irradiation. *Journal of Nuclear Materials*, 89(2-3):347–353, 1980.

[78] H.E. Rosinger. Effect of fast neutron irradiation on the properties of Zr_3Al-based alloys. *Journal of Nuclear Materials*, 95(1-2):171–180, 1980.

[79] E.M. Schulson. The tensile and corrosion behaviour of ordered Zr_3Al-based alloys. *Journal of Nuclear Materials*, 50(2):127–138, 1974.

[80] H. Mori, H. Fujita, M. Tendo, and M. Fujita. Amorphous Transition in Intermetallic Compounds Induced by Electron Irradiation. *Scripta Metallurgica*, 18(8):783–788, 1984.

[81] L. E. Rehn, P. R. Okamoto, J. Pearson, R. Bhadra, and M. Grimsditch. Solid-State Amorphization of Zr_3Al: Evidence of an Elastic Instability and First-Order Phase-Transformation. *Physical Review Letters*, 59(26):2987–2990, 1987.

[82] P. R. Okamoto, L. E. Rehn, J. Pearson, R. Bhadra, and M. Grimsditch. Brillouin Scattering and Transmission Electron Microscopy Studies of Radiation-Induced Elastic Softening, Disordering and Amorphization of Intermetallic Compounds. *Journal of the Less-Common Metals*, 140:231–244, 1988.

[83] T. Benameur and A. R. Yavari. Disordering and Amorphization of L1$_2$-type alloys by mechanical attrition. *Journal of Materials Research*, 7(11):2971–2977, 1992.

[84] E. Ma. Amorphization and Metastable Polymorphs of Ordered Intermetallics Zr$_3$Al and Ni$_3$Al. *Journal of Materials Research*, 9(3):592–597, 1994.

[85] Y. Sun and P. Hazzledine. *Dislocations in solids - L1$_2$ ordered alloys*, volume 10, chapter Geometry of dislocation glide in L1$_2$ γ'-phase, pages 27–68. Elsevier Amsterdam, 1996.

[86] P. Holdway and A. E. Staton-Bevan. Dislocation-Structures in Zr$_3$Al-Based Alloys. *Journal Of Materials Science*, 21(8):2843–2849, 1986.

[87] J. Douin. A Dissociation Transition in Zr$_3$Al Deformed at Room-Temperature. *Philosophical Magazine Letters*, 63(3):109–116, 1991.

[88] P. Shang, I. P. Jones, and R. E. Smallman. Dislocation structures in deformed Zr$_3$Al. *Electron Microscopy And Analysis*, 147:467–470, 1995.

[89] T. Ungar, S. Ott, P. G. Sanders, A. Borbely, and J. R. Weertman. Dislocations, grain size and planar faults in nanostructured copper determined by high resolution X-ray diffraction and a new procedure of peak profile analysis. *Acta Materialia*, 46(10):3693–3699, 1998.

[90] B.D. Cullity. *Elements of X-ray diffraction*. Addison-Wesley Publishing Company, 1977.

[91] Eric Lifshin. *X-ray Characterization of Materials*. Wiley-VCH, 1999.

[92] M. B. Kerber, E. Schafler, and M. J. Zehetbauer. Processing and evaluation of X-ray line profiles measured from nanostructured materials produced by severe plastic deformation. *Reviews On Advanced Materials Science*, 10(5):427–433, 2005.

[93] Ludwig Reimer. *Transmission Electron Microscopy*. Springer-Verlag, 1984.

[94] David B. Williams and Barry C. Carter. *Transmission Electron Microscopy*. Plenum Press, 1996.

[95] Marc De Graef. *Introduction to Conventional Transmission Electron Microscopy.* Cambridge University Press, 2003.

[96] Manfred Von Heimendahl. *Werkstoffkunde - Band 1: Einfhrung in die Elektronenmikroskopie.* Friedr. Vieweg & Sohn Verlag, 1970.

[97] R. Schaublin and P. Stadelmann. A Method For Simulating Electron-microscope Dislocation Images. *Materials Science and Engineering A-structural Materials Properties Microstructure and Processing*, 164(1-2):373–378, 1993.

[98] C. Gammer, C. Mangler, C. Rentenberger, and H.P. Karnthaler. Quantitative local profile analysis of nanomaterials by electron diffraction. *Scripta Materialia*, 63(3):312 – 315, 2010.

[99] Ludwig Reimer and Gerhard Pfefferkorn. *Rasterelektronenmikroskopie.* Springer-Verlag Berlin Heidelberg New York, 1977.

[100] F. J. Humphreys. Review - Grain and subgrain characterisation by electron backscatter diffraction. *Journal of Materials Science*, 36(16):3833–3854, 2001.

[101] I. Brough and F. J. Humphreys. Evaluation and application of a fast EBSD detector. *Materials Science and Technology*, 26(6):636–639, 2010.

[102] S. Banerjee and P. Mukhopadhyay. *Phase Transformations: examples from titanium and zirconium alloys.* Elsevier Amsterdam, 2007.

[103] W. J. Meng, P. R. Okamoto, L. J. Thompson, B. J. Kestel, and L. E. Rehn. Hydrogen-Induced Crystal to Glass Transformation In Zr_3Al. *Applied Physics Letters*, 53(19):1820–1822, 1988.

[104] C. Rentenberger and H. P. Karnthaler. On the evolution of a deformation induced nanostructure in a Ni_3Al alloy. *Acta Materialia*, 53(10):3031–3040, 2005.

[105] C. Rentenberger, C. Mangler, and H. P. Karnthaler. Nanostructures in $L1_2$-ordered Cu_3Au processed by torsion under high pressure. *Materials Science and Engineering A-Structural Materials Properties Microstructure and Processing*, 387:795–798, 2004.

[106] C. Rentenberger and H. P. Karnthaler. Extensive disordering in long-range-ordered Cu_3Au induced by severe plastic deformation studied by transmission electron microscopy. *Acta Materialia*, 56(11):2526–2530, 2008.

[107] C. Suryanarayana. Mechanical alloying and milling. *Progress In Materials Science*, 46(1-2):1–184, 2001.

[108] H. Nakayama, K. Tsuchiya, Y. Todaka, X. J. Hao, M. Umemoto, K. Morii, and T. Shimizu. Partial amorphization of B2 type shape memory alloys by cold rolling. *Metastable, Mechanically Alloyed and Nanocrystalline Materials*, pages 283–288, 2003.

[109] M. Peterlechner, T. Waitz, and H. P. Karnthaler. Nanoscale amorphization of severely deformed NiTi shape memory alloys. *Scripta Materialia*, 60(12):1137–1140, 2009.

[110] X. McFadden, R. S. Mishra, R. Z. Valiev, A. P. Zhilyaev, and A. K. Mukherjee. Low-temperature superplasticity in nanostructured nickel and metal alloys. *Nature*, 398(6729):684–686, 1999.

[111] N. Baluc, H. P. Karnthaler, and M. J. Mills. TEM Observation of the Fourfold Dissociation of Superlattice Dislocations and the Determination of the Fault Energies in $Ni_3(Al, Ta)$. *Philosophical Magazine A-Physics of Condensed Matter Structure Defects and Mechanical Properties*, 64(1):137–150, 1991.

[112] Y.G. Sun and P.M. Hazzledine. *Ordered Intermetallics - Physical Metallurgy and Mechanical Behaviour*, chapter Observations of Dislocation Mechanisms Governing Yield Strength in $L1_2$ Alloys, pages 177–196. Kluwer Academic Publishers, 1992.

[113] M. J. Marcinkowski, N. Brown, and R. M. Fisher. Dislocation Configurations in $AuCu_3$ and $AuCu$ Type Superlattices. *Acta Metallurgica*, 9(2):129–137, 1961.

[114] Y.Q. Sun, M.A. Crimp, and P.M. Hazzledine. Locking of (112)/3 super-Shockley partials in $L1_2$ ordered single crystals deformed at 77 K. *Philosophical Magazine A: Physics of Condensed Matter, Structure, Defects and Mechanical Properties*, 64:223–244, 1991.

[115] CT Chou, PB Hirsch, M McLean, and E Hondros. Anti-Phase Domain Boundary Tubes in Ni$_3$Al. *Nature*, 300(5893):621–623, 1982.

[116] C. Rentenberger, T. Waitz, and H. P. Karnthaler. TEM investigation of the structure of deformation-induced antiphase boundary faults in Ni$_3$Al. *Physcal Review B*, 67(9):094109, 2003.

[117] E. Muehlbacher. Elektronenmikroskopische Untersuchungen der Versetzungsstruktur und der Fehlerenergien von binaerem einkristallinen Ni$_3$Al. Master's thesis, University of Vienna, 1993.

[118] AE Vidoz and LM Brown. On Work-Hardening in Ordered Alloys. *Philosophical Magazine*, 7(79):1167, 1962.

[119] PM Hazzledine and PB Hirsch. Antiphase domain boundary tubes in ordered alloys. In NS Stoloff, CC Koch, CT Liu, and Om Izumi, editors, *High-Temperature ordered intermetallic alloys II*, volume 81 of *Materials Research Society Symposium Proceedings*, pages 75–85, 1987.

[120] PB Hirsch. Kear-Wilsdorf locks, jogs and the formation of antiphase-boundary tubes in Ni$_3$Al. *Philosophical Magazine A-Physics of Condensed Matter Structure Defects and Mechanical Properties*, 74(4):1019–1040, 1996.

[121] C. Rentenberger and H. P. Karnthaler. The stability of screw dipoles in Ni$_3$Al studied by TEM. *Intermetallics*, 16(4):571–579, 2008.

[122] P. Veyssiere and G. Saada. *Dislocations in Solids Vol. 10*, chapter Microscopy and Plasticity of the L1$_2$ gamma' phase, pages 253–441. Elsevier Amsterdam, 1996.

[123] C. Rentenberger, C. Mangler, S. Scheriau, R. Pippan, and H. P. Karnthaler. TEM study of local disordering: a structural phase change induced by high-pressure torsion. *Materials Science Forum*, 584-586:422–427, 2008.

[124] C. Rentenberger and H. P. Karnthaler. Retained coarse grains in bulk nanocrystalline Ni$_3$Al. *International Journal of Materials Research*, 98(4):255–258, 2007.

[125] M. Peterlechner, T. Waitz, and H. P. Karnthaler. Nanocrystallization of NiTi shape memory alloys made amorphous by high-pressure torsion. *Scripta Materialia*, 59(5):566–569, 2008.

[126] O. Ciuca, K. Tsuchiya, Y. Yokoyama, Y. Todaka, and M. Umemoto. Effect of Nanocrystallization and Twinning on Hardness in Ni_3Al Deformed by High-Pressure Torsion. *Materials Transactions*, 50(5):1123–1127, 2009.

[127] O. Ciuca, K. Tsuchiya, Y. Yokoyama, Y. Todaka, and M. Umemoto. Heterogeneous Process of Disordering and Structural Refinement in Ni_3Al during Severe Plastic Deformation by High-Pressure Torsion. *Materials Transactions*, 51(1):14–22, 2010.

[128] G. Wilde. Synthesis of bulk nanocrystalline materials and bulk metallic glasses by repeated cold rolling and folding (RCR). *Materials Science Forum*, 579:109–33, 2008.

[129] E. Ma and M. Atzmon. Calorimetric Evidence For Polymorphous Constraints On Metastable Zr-Al Phase Formation By Mechanical Alloying. *Physical Review Letters*, 67(9):1126–1129, 1991.

[130] T.B. Massalski. *Binary Alloy Phase Diagrams*, volume 3. ASM International, OH, 2nd edition, 1990.

[131] E. Ma and M. Atzmon. Enthalpies of Formation and Crystallization of Amorphous $Zr_{1-x}Al_x$ and $Zr_{1-x}Ni_x$ Alloys - Calculations Compared With Measurements. *Journal of Alloys and Compounds*, 194(2):235–244, 1993.

[132] M. J. Mayo, A. Suresh, and W. D. Porter. Thermodynamics for nanosystems: grain and particle-size dependent phase diagrams. *Reviews on Advanced Materials Science*, 5(2):100–9, 2003.

[133] Q. Jiang and C. C. Yang. Size effect on the phase stability of nanostructures. *Current Nanoscience*, 4(2):179–200, 2008.

[134] R. V. Nandedkar and P. Delavignette. On the Formation of A New Superstructure In the Zirconium-aluminum System. *Physica Status Solidi A-applied Research*, 73(2):K157–160, 1982.

[135] A. P. Zhilyaev, B. K. Kim, J. A. Szpunar, M. D. Baro, and T. G. Langdon. The microstructural characteristics of ultratine-grained nickel. *Materials Science and Engineering A-structural Materials Properties Microstructure and Processing*, 391(1-2):377–389, 2005.

[136] T. Hebesberger, H.P. Stuwe, A. Vorhauer, F. Wetscher, and R. Pippan. Structure of Cu deformed by high pressure torsion. *Acta Materialia*, 53(2):393–402, 2005.

[137] O. N. Senkov, F. H. Froes, V. V. Stolyarov, R. Z. Valiev, and J. Liu. Microstructure and microhardness of an Al-Fe alloy subjected to severe plastic deformation and aging. *Nanostructured Materials*, 10(5):691–698, 1998.

[138] J. Y. Huang, Y. T. Zhu, X. Z. Liao, and R. Z. Valiev. Amorphization of TiNi induced by high-pressure torsion. *Philosophical Magazine Letters*, 84(3):183–190, 2004.

[139] A. Vorhauer and R. Pippan. On the homogeneity of deformation by high pressure torsion. *Scripta Materialia*, 51(9):921–925, 2004.

[140] C. Xu, Z. Horita, and T. G. Langdon. The evolution of homogeneity in processing by high-pressure torsion. *Acta Materialia*, 55(1):203–212, 2007.

[141] Y. B. Xu, J. H. Zhang, Y. L. Bai, and M. A. Meyers. Shear localization in dynamic deformation: Microstructural evolution. *Metallurgical and Materials Transactions A-physical Metallurgy and Materials Science*, 39A(4):811–843, 2008.

[142] Y. Harai, Y. Ito, and Z. Horita. High-pressure torsion using ring specimens. *Scripta Materialia*, 58(6):469–472, 2008.

[143] M. Hafok and R. Pippan. Post-shear deformation of high pressure torsion-deformed nickel under hydrostatic pressure. *Scripta Materialia*, 56(9):757–760, 2007.

[144] C. Rentenberger, T. Waitz, and H. P. Karnthaler. Formation and structures of bulk nanocrystalline intermetallic alloys studied by transmission electron microscopy. *Materials Science and Engineering A-*

structural Materials Properties Microstructure and Processing, 462(1-2):283–288, 2007.

[145] G. R. Canova, U. F. Kocks, and J. J. Jonas. Theory of torsion texture development. *Acta Metallurgica*, 32(2):211–226, 1984.

[146] F. Montheillet, M. Cohen, and J. J. Jonas. Axial stresses and texture development during the torsion testing of Al, Cu and α-Fe. *Acta Metallurgica*, 32(11):2077–2089, 1984.

[147] Dmitry Orlov, Pinaki Prasad Bhattacharjee, Yoshikazu Todaka, Minoru Umemoto, and Nobuhiro Tsuji. Texture evolution in pure aluminum subjected to monotonous and reversal straining in high-pressure torsion. *Scripta Materialia*, 60(10):893–896, 2009.

[148] Y. T. Zhu, J. Narayan, J. P. Hirth, S. Mahajan, X. L. Wu, and X. Z. Liao. Formation of single and multiple deformation twins in nanocrystalline fcc metals. *Acta Materialia*, 57(13):3763–3770, 2009.

[149] D. A. Rigney and S. Karthikeyan. The Evolution of Tribomaterial During Sliding: A Brief Introduction. *Tribology Letters*, 39(1):3–7, 2010.

Acknowledgments

First of all, I want to thank Ao. Univ.-Prof. Mag. Dr. Christian Rentenberger for the supervision of this thesis and the possibility of employment in the IK in the early stages and in his project in the later stages of the thesis. I want to thank him especially for the innumerable hours of support, be it in experimental issues or in theoretical considerations.

I also want to thank Univ.-Prof. i.R. Dr. Hans-Peter Karnthaler, who helped me a lot in preparing publications and presentations and took part in a lot of fruitful discussions, often introducing interesting new sights to problems. I also want to thank him for the financial support through the IK during the early stages of the thesis.

Ao. Univ.-Prof. Mag. Dr. Thomas Waitz was always supportive and I want to thank him for that. I also want to express my gratitude to him for being a vital factor in making my stay as a visiting scientist at the National Institute for Materials Science in Tsukuba, Japan, possible.

I want to thank Mag. Dr. Clemens Mangler, Mag. Dr. Martin Peterlechner and DI Christoph Gammer for their constant support and the good collaboration in a wide variety of fields ranging from experimental methods and materials science problems to computer issues and many more.

Ing. Andreas Berger deserves thanks for the help with specimen preparation involving many different devices and also for always knowing where tools and similar equipment can be found and how to use it in a proper way.

I want to thank the whole group Physics of Nanostructured Materials for the great working climate and support whenever it was needed, especially Regina Pinter for having forms filled out before I even thought about needing them and Claudia Wich for her help, in particular for developing the TEM films.

Special thanks are due to the colleagues of the National Institute for

Materials Science (NIMS) in Tsukuba, Japan. Prof. Dr. Koichi Tsuchiya was a great supervisor and spent a lot of time supporting my studies during this scientifically valuable and personally precious two months in Japan and I am thankful for that. I also want to thank Dr. Seiichiro Ii, Dr. Susan Farjami and Dr. Octav Ciuca for support at the NIMS.

For support in technical SPD issues, I want to thank Dr. Georgi Stefanov for the help with the rolling device and Dr. Stephan Scheriau, DI Peter Kutleša and Susi Kahofer for support with the HPT deformation.

I want to thank Prof. Dr. Erland M. Schulson, whom I do not know personally, but whose sample material has accompanied me for the last four years.

I want to thank O.Univ.Prof. Dipl.-Ing. Dr. Hans-Peter Degischer and Prof. Dr. Jürgen Eckert for agreeing to examine the present thesis.

Last but not least I want to thank my family and friends. Special thanks are due to my parents who provided the very general foundation for the completion of this thesis in the last 28 ± 0.2 years. I also want to thank the rest of my family and my friends for many discussions making it possible to learn a lot about all different areas from them and also to meet the need to tell about my work. Special thanks are due to Barbara who has without doubt always been the first to tolerate my mood and balance my state of mind for the last three years.

Curriculum vitae

Personal Details

Name: Mag. David Geist
Born: May 28th, 1982 in Vienna, Austria
Nationality: Austria

Education

January 2009
Participation at the Electron Microscopy for Materials Science (EMAT) Winter School in Antwerp, Belgium

From March 2007
PhD student, thesis title: "Deformation induced phase transformation in Zr_3Al studied by transmission electron microscopy" at the Faculty of Physics, University of Vienna

March 2007
Graduation in physics with distinction

February 2006 – February 2007
Diploma thesis "Transmission Electron Microscopy Investigation of Protein Crystals" at the Institute of Materials Physics, University of Vienna

July 2005 – January 2006
Semester abroad at The Australian National University, Canberra, Australia
Research Project „Cross-section Transmission Electron Microscopy Analysis of Germanium Implanted GaAs" at the Department of Electronic Materials Engineering

October 2002 – March 2007
Physics, University of Vienna

Professional Scientific Activities

From August 2010
Research Associate at the University of Vienna within the project Metastable Phases in bulk Intermetallics – TEM study

March 2010 – July 2010
Contractor at the University of Vienna

January 2010 – March 2010
Invited researcher at the National Institute for Materials Science, Tsukuba, Japan

March 2007 – December 2009
Research associate at the Faculty of Physics, University of Vienna within the doctoral college of the University of Vienna "Experimental Materials Science – Nanostructured Materials"

Scientific Conferences

September 2010
Participation and talk at the 60th Annual Meeting of the Austrian Physical Society, Salzburg, Austria

July 2010
Participation and talk at the "17th International Symposium on Metastable, Amorphous and Nanostructured Materials (ISMANAM)", Zurich, Switzerland

September 2009
Invited talk at the conference "Electron Microscopy and Diffraction of Defects, Nanostructures, Interfaces and Amorphous Materials", Oxford, UK

September 2009
Participation and poster presentation at the Microscopy Conference 2009 in Graz, Austria

September 2008
Participation at the Tutorial and Discussion Meeting "Multiscale Phenomena in Materials" in Vienna, Austria

September 2008
Participation and poster presentation at the 14th European Congress for Microscopy in Aachen, Germany

August 2008
Participation and poster presentation at the 4th International Conference on Nanomaterials by Severe Plastic Deformation in Goslar, Germany

June 2007
Participation and poster presentation at the 8th Multinational Congress on Microscopy, Prague, Czech Republic

Prizes and Awards

Silver Medal "Best Poster" at the 4th International Conference on Nanomaterials by Severe Plastic Deformation 2008 in Goslar, Germany

Merit grant of the University of Vienna for the academic year 2006/07

Teaching at University

October 2008 – September 2009 and from March 2011
Physics laboratory course 1 and 2

Publications

D. Geist, C. Rentenberger, H.P. Karnthaler. Extreme structural inhomogeneities in high pressure torsion samples along the axial direction. *Acta Materialia*. submitted

V. Kozina, D. Geist, L. Kubinova, E. Bilic, H.P. Karnthaler, T. Waitz, J. Janacek, O. Chernyavskiy, I. Krhen, D. Jezek. Visualization of Reinke's crystals in normal and cryptorchid testis. *Histochemistry and Cell Biology* doi: 10.1007/s00418-011-0782-6

D. Geist, S. Ii, K. Tsuchiya, H.P. Karnthaler, G. Stefanov, C. Rentenberger. Nanocrystalline Zr_3Al made through amrphization by repeated cold rolling and followed by crystallization. *J All Comp* **509** 5 (2011) 1815

D. Geist, C. Gammer, C. Mangler, C. Rentenberger, H.P. Karnthaler. Electron Microscopy of severely deformed $L1_2$ intermetallics. *Phil Mag* **90** 35-36 (2010) 4635

D. Jezek, V. Kozina, D. Geist, L. Kubinova, H.P. Karnthaler, L. Banek. Reinke's crystals: are they related to cryptorchidism? *Int J Androl* **33** (2010) 91

D. Geist, S. Ii, K. Tsuchiya, G. Stefanov, H.P. Karnthaler, C. Rentenberger. Nanocrystallization of intermetallic Zr_3Al by Amorphization by Repeated Cold Rolling and subsequent heat treatment**.** *Proc. of the 60th annual meeting of the Austrian Physical society* (2010) 103

D. Geist, S. Ii, K. Tsuchiya, H.P. Karnthaler, G. Stefanov, C. Rentenberger. Creation of Nanocrystalline Zr_3Al through Amorphization by Repeated Rolling and Recrystallization. *Proc. of the 17th International Symposium on Metastable, Amorphous and Nanostructured Materials (ISMANAM)* (2010) 51

D. Geist, A. Thaller, C. Rentenberger, J. Bernardi, H.P. Karnthaler. SEM and TEM cross-section study of inhomogeneities in Zr3Al deformed by high pressure torsion. *Proc. of Microscopy Conference 2009 Graz* Vol. 3 (2009) 251

D. Geist, C. Rentenberger and H. P. Karnthaler. TEM of high pressure torsion processed intermetallic Zr_3Al. *Proc. of the 14th Europ. Micr. Congr.* Vol. 2 (2008) 647.

D. Geist, C. Rentenberger and H. P. Karnthaler. Severe plastic deformation of bulk intermetallic Zr_3Al studied by TEM. *Mater. Sci. For.* **584-586** (2008) 553.

D. Jezek, D. Geist, Lj. Banek, G. Juric Lekic, H.P. Karnthaler, T. Waitz, B. Foretic and K. Semanjski. Reinke's crystals in infertile patients. *Acta Clin. Croat.* **46**, 2 (2007) 220

D. Geist, C. Rentenberger, T. Waitz, H. P. Karnthaler. TEM Investigation of thin protein crystals. *Proc. 8th Multinat. Congr. on Microscopy, Prague* (2007) 465

BOLTZMANNGASSE 5 • 1090 WIEN • AUSTRIA
PHONE +43 1 4277 51311 • E-MAIL: david.geist@univie.ac.at